X-ray scattering studies of charge stripes in transition-metal oxides

Su, Yixi

X-ray Scattering Studies of Charge Stripes in Transition-metal Oxides

by

Yixi Su

A thesis submitted in fulfilment of the requirements for the degree of Doctor of Philosophy to The University of Durham 1999

Abstract

This thesis describes the development of single crystal x-ray scattering applied to the study of charge stripes in some exotic transition-metal oxides. Charge stripes in the cuprates and manganites are strongly associated with high T_C superconductivity and colossal magnetoresistance, and can be characterised by the satellite reflections located around related Bragg peaks below the charge ordering transition temperature (T_{CO}). The intensities of these extremely weak satellite reflections are between 10^{-4} and 10^{-6} less than those of Bragg reflections, thus very high brilliant rotating-anode x-ray and synchrotron radiation sources are required to study them. The structure factors and correlation lengths of the charge stripes can be directly obtained by measurements of the integrated intensities and peak widths of the charge ordering satellite reflections as a function of temperature.

The charge stripes in single crystals of $Bi_{0.24}Ca_{0.76}MnO_3$, $Nd_{0.5}Sr_{0.5}MnO_3$ and $La_{5/3}Sr_{1/3}NiO_4$ have been comprehensively characterised using both laboratory and synchrotron radiation x-ray scattering. The measurements on $Bi_{0.24}Ca_{0.76}MnO_3$ directly demonstrate a strong relationship between the charge stripe ordering and the first-order structural phase transition, which is common in many perovskite manganites. Direct evidence for the existence of perpendicular charge-ordered domains in manganites was obtained for the first time by x-ray scattering in $Nd_{0.5}Sr_{0.5}MnO_3$, and this result demonstrates that charge stripes have complex structures in the mesoscopic length scale. Scattering was also observed at the positions in reciprocal space associated with spin ordering into stripes. These showed evidence of different critical behaviour than the corresponding charge stripe satellites. The quasi two-dimensional feature of the charge stripes in $La_{5/3}Sr_{1/3}NiO_4$ was successfully demonstrated by the critical exponents of the charge stripe melting and by the measurements of their in-plane and out-of-plane correlation lengths. Experimental evidence for the existence of electronic liquid-crystal phases in $La_{5/3}Sr_{1/3}NiO_4$ was obtained, in agreement with recent theoretical predictions

Acknowledgements

Firstly, I must gratefully thank my supervisor Dr. P. D. Hatton for giving me the opportunity, the encouragement, and the space to carry out my study, his countless helps for me certainly are something to remember. I would also like to thank Prof. B. K. Tanner, my second supervisor who, through his tenure as head of department, has provided me with the excellent facilities and much needed financial aids from Physics Department.

I particularly would like to thank Dr. C.-H. Du for his constant help and permission to share some data appearing in Chapter 7. Many thanks would also go to other members in Durham X-ray Scattering and Magnetism group, Dr. W-J. Lin, Dr. I. Pape, Dr. T. P. A. Hase, Mr. B. Fulthorpe, Mr. J. Clarke for their help and friendship.

I would like to thank Prof. S-W. Cheong at Rutgers University and Bell Laboratories, for his constant suggestion and providing me with excellent single crystals. I am grateful to the organisers and fellow participants of the STRIPE 98 conference for giving me plenty of motivation and ideas to write up this thesis.

Many thanks should also go to other collaborators, Dr. S. P. Collins, Dr. C. C. Tang, Ms. B. M. Murphy (the SRS), Dr. S. Brown (the ESRF) for their great assistance during my synchrotron radiation experiments.

I would also like to thank many technical staffs in this department, John, Norman, Pauline and Mike for their help during my PhD studying.

Finally, I would like to thank my wife and parents for their emotionally support and encouragement all the time. This thesis is dedicated to them.

Declaration

I declare that the work contained in this thesis is my own and has not been submitted previously for any other degree. All the work presented herein was conducted by the author, unless explicitly stated otherwise. Some of the results of this thesis have appeared in:

1. Y. Su, C.-H., Du, P. D. Hatton, S. P. Collins and S-W. Cheong, *Charge ordering and related structural phase transition in single-crystal* $(Bi_{0.24}Ca_{0.76})MnO_3$, Phys. Rev. B, **59**, 1999 (in print)
2. Y. Su, C.-H. Du, B. K. Tanner, P. D. Hatton, S. P. Collins, S. Brown, D. F. Paul and S-W. Cheong, *X-ray scattering studies of charge stripes in manganites and nickelates*, Journal of Superconductivity, 1999 (in print)
3. C.-H., Du, Y. Su, P. D. Hatton, S. P. Collins, A. J. Chowdhury and S-W. Cheong, *X-ray scattering studies of charge ordering in bismuthates, manganites and nickelates*, J. of Phys. D., 1999 (in print)

Yixi Su, March 1999

Contents

Chapter 1

Introduction

Transition-metal oxides have long been the subject of study, because they exhibit a wide range of exotic and still imperfectly understood structural, electronic and magnetic behaviour, for example, high-T_C superconductivity observed in some copper oxides, and colossal magnetoresistance discovered in some manganese oxides. These properties cannot be explained within the context of the usual one-electron band theory that accounts well for the properties of most other solids, indicating the importance of strong electron-electron and electron-lattice correlations.

More recently, attention has become focused on *Charge Stripes* appearing in transition-metal oxides. In some materials, the electronic charge density organises itself into stripes. Stripe physics has been of intense interest to condensed matter physics, as an example of a non-trivial ordering phenomenon, and because of its possible connection to high-T_C superconductivity and colossal magnetoresistance.

Stripe physics also opens a window onto the fundamental issue of the interplay between *hybridisation* and *interaction*. Hybridisation, the overlap of electron wavefunctions centered on different sites, is a quantum-mechanical effect that allows electrons to hop from one atom to another, thus tending to spread the electronic density uniformly through the solid. In contrast, interactions of electrons with one another and with displacements of the atoms in the solid tend to promote non-uniform charge distributions. If the hybridisation is dominant, a conventional metal (such as copper) or insulator (such as diamond) results. But if the interactions are dominant, charge ordering may occur: in a charge-ordered state the electrons arrange themselves

in a pattern with periodicity differing from that of the underlying lattice. The precise pattern is determined by the nature of the interactions and by the residual effects of the hybridisation.

In many circumstances the charge ordering takes the form of stripes, as shown in Fig. 1.1, which seem to be the best compromise between the localising effect of interactions and the delocalising effect of hybridisation. Along the stripe, the charge density is constant except for the underlying lattice; perpendicular to the stripe, the charge density varies with a period different from that of the lattice, as shown in Fig. 1.1.

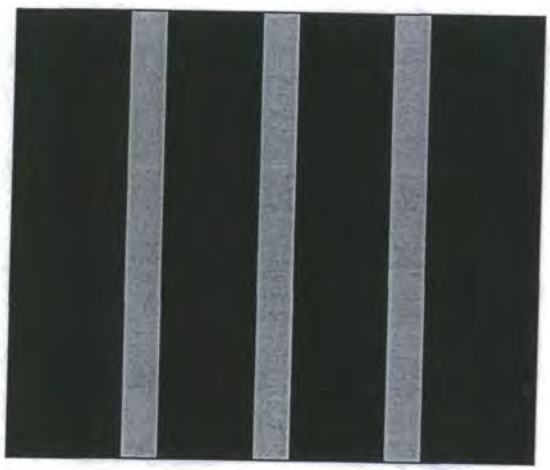

Fig. 1.1 A schematic view of charge stripes. The dark and grey ribbons represent the regions with different charge density distributions.

This thesis comprehensively describes the single-crystal x-ray scattering studies of charge stripes in some transition-metal oxides. An outline of this thesis is presented as follows.

In chapter 2, the structures of the charge stripes in various transition-metal oxides are reviewed. This introduction is based on some recent experimental reports on $La_{1.6-x}Nd_{0.4}Sr_xCuO_{4+\delta}$, $La_{2-x}Sr_xNiO_{4+\delta}$, and perovskite manganites $R_{1-x}A_xMnO_3$.

Chapter 3 gives a comprehensive introduction to the impact of charge stripes on the physics of strongly correlated transition-metal oxides. The possible role played by charge stripes in high-T_C superconductivity and colossal magnetoresistance is described. Various theories regarding stripe formation are also given.

Chapter 4 covers both theoretical and experimental aspects of x-ray scattering methods. Kinematical scattering theory is given in brief. The principles of x-ray sources, including both conventional and synchrotron radiation sources, and diffractometers are introduced. Synchrotron radiation experimental techniques are summarised.

In chapter 5, the charge stripes and related structural phase transitions in single-crystal $Bi_{0.24}Ca_{0.76}MnO_3$ were comprehensively demonstrated via x-ray scattering.

In chapter 6, the properties of the charge stripes in $Nd_{0.5}Sr_{0.5}MnO_3$ were extensively studied by x-ray scattering. The first evidence for the existence of the charge-ordered domains was obtained by high resolution measurements.

In chapter 7, the quasi 2-dimensional feature of the charge stripes in $La_{5/3}Sr_{1/3}NiO_4$ was directly demonstrated. The charge stripes were found to be disordered and quenched even at temperatures far below T_{CO}, which is interpreted as the evidence for the possible existence of the electronic liquid-crystal phases.

Chapter 2

Charge Stripes (I): Structure

2.1 Introduction

Charge stripes are just one manifestation of the charge ordering phenomenon, in which the charge density modulation can be stripe-like, and have been the subject of intensive investigation since the early 90's. Charge ordering is commonly observed in various mixed-valent transition-metal oxides[1], when charge carriers localize and form a long-range ordered pattern in the host lattice below a charge-ordering temperature, T_{CO}. The striped charge orderings observed in some cuprates, nickelates and manganites are particularly interesting because of their importance in understanding some intriguing phenomena, such as high-T_C superconductivity (HTSC)[2] and colossal magnetoresistance (CMR)[3].

To have a complete understanding of charge stripe physics, the first necessary step is to reveal and clarify the structure of charge stripes, their microscopic appearance and formation of the charge stripe modulation. Charge stripes have often been found to be accompanied by related spin and orbital ordering in strongly correlated electron systems. These cooperative orderings have been understood to be the result not only of the strong electron-electron interaction, but also of the strong electron-phonon coupling (electron-lattice coupling), therefore, the electronic morphology of stripes will vary over a number of different electron-lattice systems, e.g., the cuprates have a relatively weak electron-phonon interaction, the manganites display a relatively strong electron-phonon coupling, and the nickelates lie somewhere between the cuprates and manganites.

Scattering methods utilising electrons, neutrons and x-rays have so far been powerful techniques providing information on structures of charge stripes in various compounds. The charge stripes in manganites have been found to be correlated all in three-dimensions (3D), in the nickelates they appear almost two-dimensional (2D), however, in most cuprates, the charge stripes display fluctuating and dynamical features. The stripe physics has been just starting to emerge during my PhD studying, and structures of charge stripes and relevant properties are still largely unclear in many compounds, even the concept of the *stripe* itself has been in wide debate. Therefore, it is impossible to give a comprehensive review in this thesis, but a brief account based on some well-known observations and theories. This chapter is organized as follows, a simple historical account of charge stripe is given in Section 2.2, and a model for charge stripes in $La_{1.6-x}Nd_{0.4}Sr_xCuO_{4+\delta}$ and other cuprates is described in Section 2.3. Section 2.4 details the extension to $La_{2-x}Sr_xNiO_{4+\delta}$ compounds, and then, a detailed discussion on the striped charge and orbital ordering in perovskite manganites, such as $La_{1-x}Ca_xMnO_3$ is presented in Section 2.5.

2.2 Brief history: from phase separation to stripes

High-T_C superconductivity was discovered in 1986 by Müller and Bednorz[4] in $La_{2-x}Ba_xCuO_4$. Soon after, the phenomenon of macroscopic phase separation (PS) in $La_2CuO_{4+\delta}$ was discovered by Jorgensen[5] etc. in 1988, which revealed the coexistence of oxygen-poor (insulating $La_2CuO_{4.01}$) domains and oxygen-rich (superconducting $La_2CuO_{4.06}$) domains for $0.01<\delta<0.06$ and $T<T_{PS}$. This was the first realisation of macroscopic charge inhomogeneity[6] in superconducting cuprates.

In 1990, the discovery of a one-dimensional (1D) charge modulation in a superlattice of quantum stripes in the superconducting CuO_2 plane by Bianconi and others[7, 8],

revealed a mesocopic phase separation and a resulting inhomogeneous CuO_2 lattice. This result was a major surprise, for at that time the assumption of a homogeneous and rigid superconducting CuO_2 plane was a widely accepted paradigm and the coexistence of polaron ordering in 1D stripes and superconductivity was considered to be detrimental for the superconducting phase.

In 1993, Chen and Cheong at Bell Labs. discovered the striped charge ordering in the related nickelate[9], and Johnston[10] at Ames Lab. found evidence for 1D charge domain walls between antiferromagnetic domains in copper perovskites at very low doping levels. In 1995 Tranquada[11] at Brookhaven National Lab. discovered magnetic and charge modulations in the insulating cuprate perovskite $La_{1.6-x}Nd_{0.4}Sr_xCuO_{4+\delta}$ at the critical hole concentration of 1/8. He interpreted these results as due to formation of charge stripe order. Another type of striped charge and orbital ordering was reported in 1996 by Chen and Cheong[12, 13] in the 3D manganite perovskites that show colossal magnetoresistance. The stripes reported in these compounds can also be seen as phase separation on a microscopic scale. Since then, there has been now more considerable experimental evidence for the existence of striped charge ordering in various strongly correlated transition-metal oxides.

2.3 Charge stripes in $La_{1.6-x}Nd_{0.4}Sr_xCuO_{4+\delta}$ and related cuprates

2.3.1 Background

$La_{1.6-x}Nd_{0.4}Sr_xCuO_{4+\delta}$ (x = 0.12) has played a central role in stripe physics since Tranquada creatively interpreted observed magnetic and charge ordering as due to a stripe-ordered modulation[11, 14-18]. Actually, the stripe interpretation should be regarded as a natural development following some pioneering efforts, such as

theoretical studies of the phase separation and charge inhomogeneity in copper oxides. These showed that it is quite possible that the competition between the local tendency toward macroscopic phase separation[6] and the long-range Coulomb interaction among charge carriers leads to modulated domain structure at mesoscopic scales[2, 19]. Tranquada linked these studies and neutron scattering observations[20-24] of the similar magnetic and charge ordering in various hole-doped La_2NiO_4 compounds.

The charge stripe observed in $La_{1.6-x}Nd_{0.4}Sr_xCuO_{4+\delta}$ (x = 0.12) has also been suggested to have a strong influence on the supression[25] of superconductivity in $La_{2-x}Ba_xCuO_4$ when x = 1/8. Several studies[26, 27] on cuprate systems have established that the suppression of the superconductivity requires both a hole concentration of 1/8 per Cu and a distortion from the low-temperature-orthorhombic (LTO) to the low-temperature-tetragonal (LTT) structure. One system that is particularly convenient to investigate this phenomenon is $La_{1.6-x}Nd_{0.4}Sr_xCuO_{4+\delta}$ (x = 0.12), due to the coexistence of 1/8 hole concentration and the LTT phase.

The superconductors[28-30] derived from La_2CuO_4, with Ba and Sr substituting for La, were the first high-T_C oxides to be reported. In many ways, they serve as prototypes because their basic structures are relatively simple, with oxygen content which varies little over a wide range of Ba and Sr substitution. At higher temperature the compounds have the tetragonal K_2NiF_4-structure with *I4/mmm* space group (denoted HTT). However at lower temperatures, and for most superconducting compositions the stable phase is LTO with standard space group *Cmca*. A notable complication in $La_{2-x}Ba_xCuO_4$ and $La_{1.6-x}Nd_{0.4}Sr_xCuO_4$ is the presence of LTT phase at or below 100K, space group $P4_2/ncm$, which, near the Ba (or Sr) content $x \approx 1/8$ is associated with a severely depressed T_C. A schematic phase diagram of $La_{2-x}Sr_xCuO_4$ is shown as Fig. 2.1, for x = 0 (no Sr doping) this compound is an antiferromagnetic (AF) insulator. Hole doping, through substituting different amounts of Sr (or Ba or Ca) for La, leads to metallic behaviour and to superconductivity in the range $0.05 \leq x \leq 0.5$ below T_C.

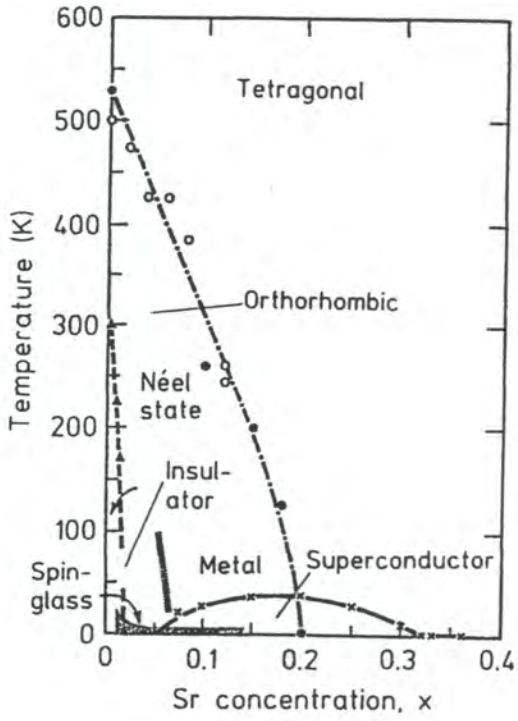

Fig. 2.1 Phase diagram of $La_{2-x}Sr_xCuO_4$[28-30]

The crystalline structure of $La_{1.6-x}Nd_{0.4}Sr_xCuO_{4+\delta}$, is same as that of the $La_{2-x}Sr_xCuO_{4+\delta}$ (La-214), as shown in Fig. 2.2, which usually is discussed in terms of the tetragonal *I*4/*mmm* space group. The *a*- and *b*- axes of the unit cell have been chosen to be along the Cu-O bond in the CuO_2 plane, while the *c*-axis is perpendicular to the CuO_2 layer, and the unit cell has the dimensions $a = b \approx a_p$, $c \approx 13.2$ Å, where a_p is the cell parameter of basic perovskite structure ABO_3.

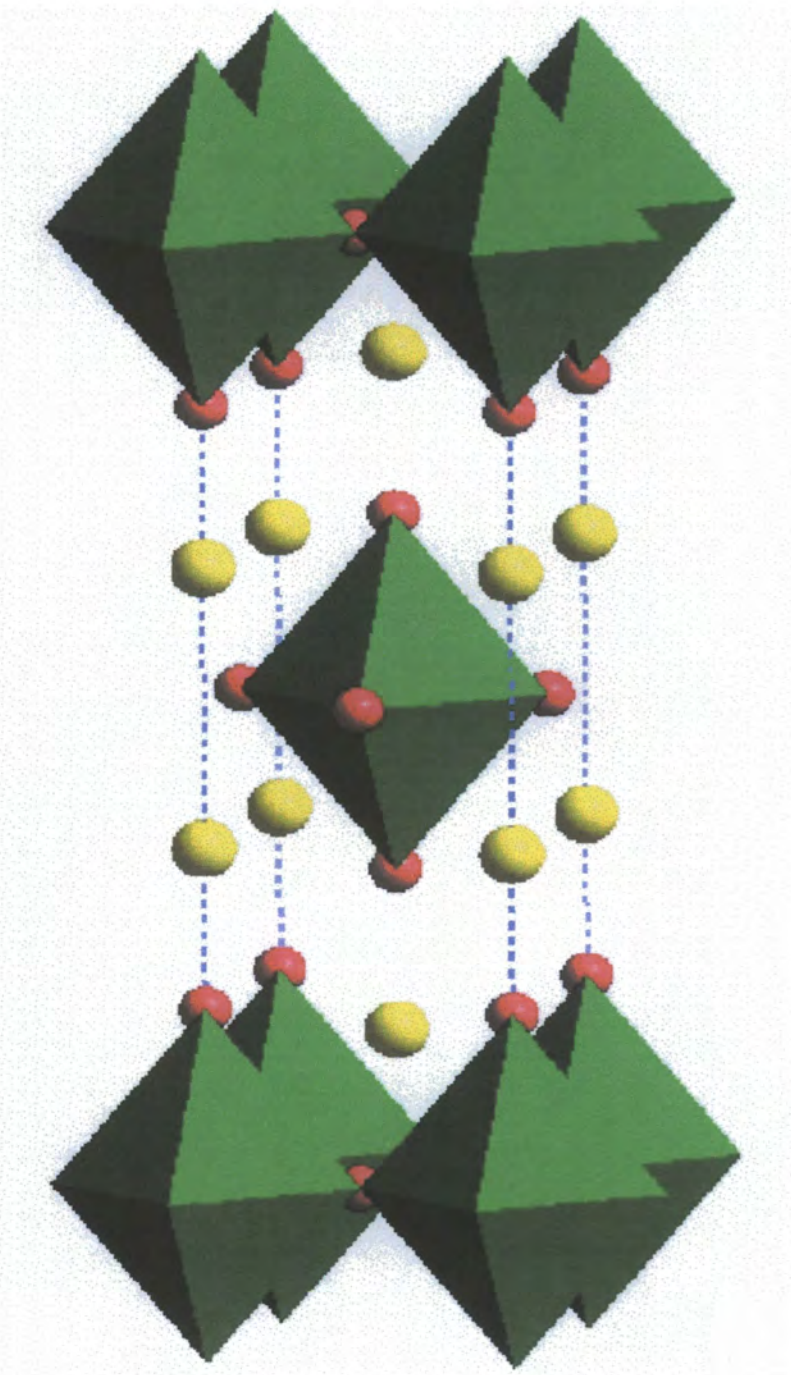

Fig. 2.2 The crystalline structure of $La_{2-x}Sr_xCuO_{4+\delta}$ compound

The compound $YBa_2Cu_3O_{7-\delta}$[28-30] sometimes referred to as the Y123 compound, has an orthorhombic or tetragonal structure. For $0 < \delta < 0.6$, Y123 is orthorhombic and superconducting at low temperature, and for $0.6 < \delta < 1$, it is tetragonal. The T_C also depends on the oxygen deficiency and the highest T_C of these compounds is about 90K when $0 < \delta < 0.2$. The difference between La-214 and Y123 is that $La_{2-x}Sr_xCuO_4$ contains one CuO_2 plane while Y123 contains two adjacent CuO_2 plane plus a Cu-O chain in a primitive unit cell. The dimensions of Y123 unit cell are very close to that of La-214, with $a \approx b \approx a_p$, $c \approx 11.7$ Å. The a- and c-axes are both parallel to the Cu-O bond, and the c-axis runs along Cu-O chains.

2.3.2 Experimental evidence and the stripe model

The first evidence for charge and spin stripes in perovskite copper oxides was obtained in $La_{1.6-x}Nd_{0.4}Sr_xCuO_{4+\delta}$ ($x = 0.12$) compounds using neutron diffraction by Tranquada[11, 14, 16]. The data showed that a significant elastic magnetic component developed in the LTT phase, and satellite peaks at second-harmonic positions were observed split about the nuclear Bragg peaks, e.g. (*200*), suggestive of charge ordering scattering. Scans of superlattice peaks in the (*hk0*) zone of reciprocal space are shown in Fig. 2.3,

The characteristic wavevector for the charge density modulation (charge ordering) was observed to be,

$$\boldsymbol{Q}_{CO} = (2\varepsilon, 0, l) \text{ and } (0, 2\varepsilon, l) \qquad (2.1)$$

For the spin ordering, the observed modulation wavevector was,

$$\boldsymbol{Q}_{SO} = (\pm\varepsilon, 0) \text{ and } (0, \pm\varepsilon) \qquad (2.2)$$

where, $\varepsilon = x$, and the components of $\boldsymbol{Q}$ are specified in units of $2\pi/a$. The locally antiferromagnetic Cu spins are characterized by a two-dimensional wavevector $\boldsymbol{Q}_{AF}$ = (1/2, 1/2). Therefore satellite peaks related to the charge ordering and spin ordering are expected at position $\boldsymbol{G} \pm \boldsymbol{Q}_{CO}$ and $\boldsymbol{G} \pm \boldsymbol{Q}_{AF} \pm \boldsymbol{Q}_{SO}$, respectively. The charge ordering was further confirmed by a high-energy x-ray scattering measurement on the same sample, because x-ray scattering is a far more sensitive detector of charge density distribution than neutron scattering, and is relatively insensitive to spin ordering.

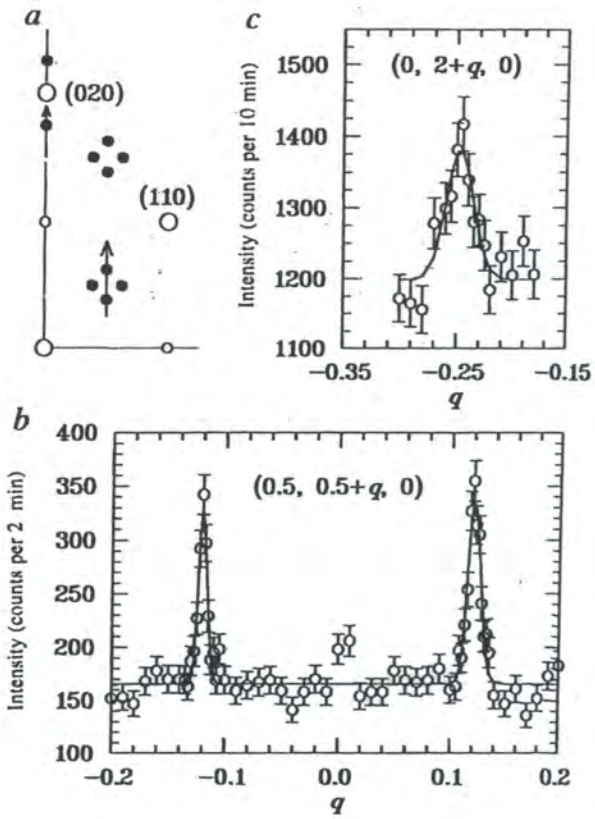

Fig. 2.3 Scans of superlattice peaks in (hk0) zone of reciprocal space of $La_{1.6-x}Nd_{0.4}Sr_xCuO_{4+\delta}$ (x = 0.12) (taken from Tranquada[11])

According to the above observations, one model[11, 14] of stripes was proposed in a tetragonal crystal of La_2CuO_4 doped with a ratio of one hole to every eight copper atoms, as shown in Fig. 2.4. The added charges (holes) line up in rows in the copper

oxide plane, the charge rows are also antiphase domain walls between antiferromagnetically ordered spins in the CuO_2 planes, with nearest neighbors having opposite spins. The period of the charge stripes is four lattice sites whereas that for the antiferromagnetic ordering is twice as much, because the phase changes by π across each charge stripe. The charge stripes run horizontally along the direction of the Cu-O bond.

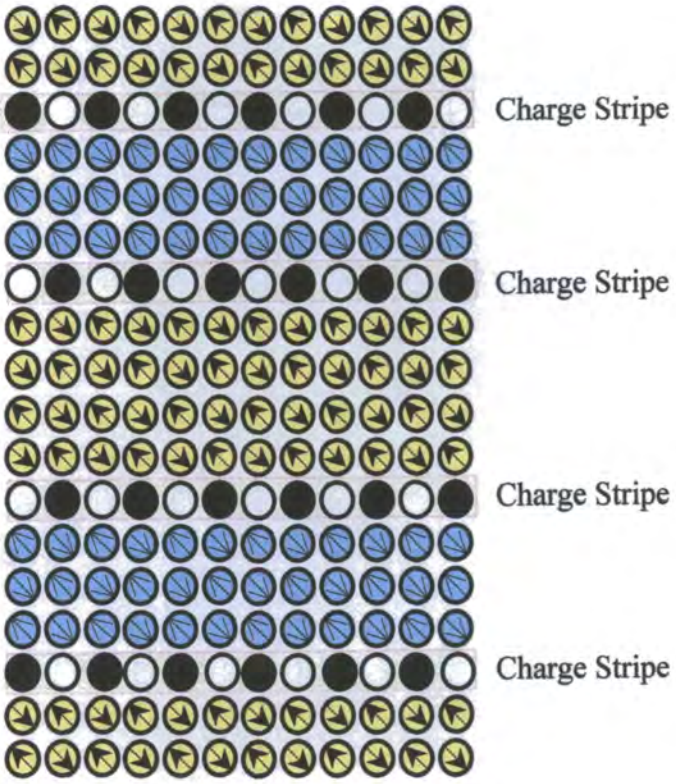

Fig. 2.4 The stripe model of $La_{1.6-x}Nd_{0.4}Sr_xCuO_{4+\delta}$ (x = 1/8). Only the Cu sites are represented. Arrows indicate the presence of magnetic moments, which are locally antiparallel. The regions with different filling colors (blue and yellow) are antiphase magnetic domains. Holes (black filled circles) are located at the antiphase domain boundaries, which are indicated by the rows of circles without arrows (taken from Tranquada[11, 14])

The temperature dependence of the intensity of the superlattice peak of the charge stripes and spin ordering, is shown in Fig. 2.5. The (1, 0, 0) peak is allowed in LTT but not LTO. The magnetic peaks decrease faster than the charge peaks, which implies that the formation of the stripes is charge-driven. However, both types of order disappear at or before the LTT-LTO structural transition at 70 K is reached. This indicates that the stripe ordering can only exist in LTT phase in $La_{1.6-x}Nd_{0.4}Sr_xCuO_{4+\delta}$ ($x = 0.12$).

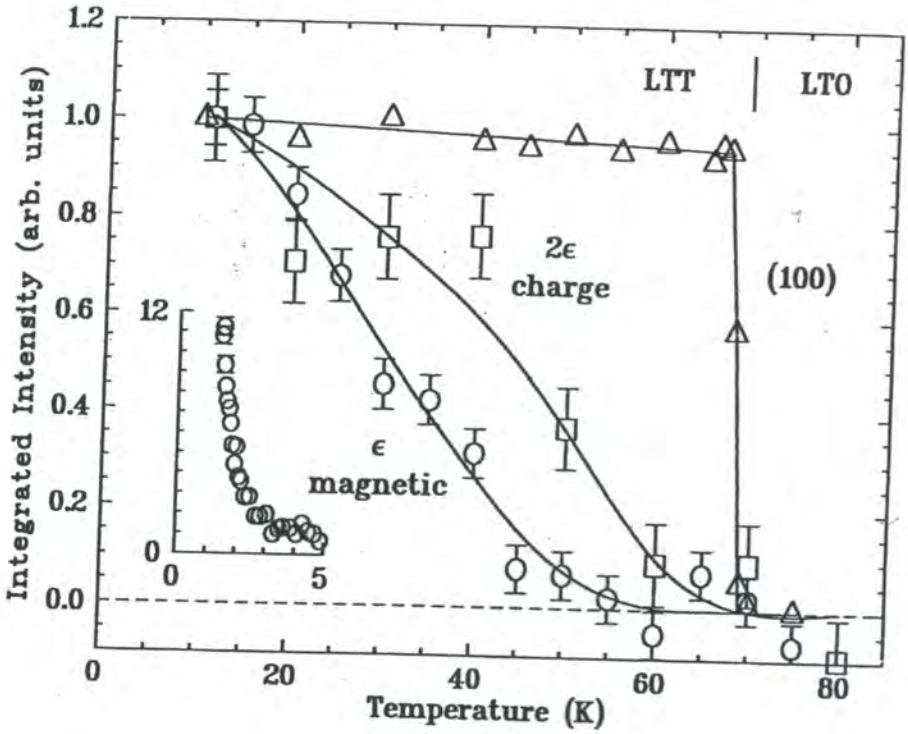

Fig. 2.5 Temperature dependence of charge and spin ordering in $La_{1.6-x}Nd_{0.4}Sr_xCuO_{4+\delta}$ ($x = 0.12$)(taken from Tranquada[11, 14])

In $x = 0.15$ and 0.20 $La_{1.6-x}Nd_{0.4}Sr_xCuO_{4+\delta}$ samples[16], the elastic magnetic ordering scattering has also been found to coexist with the superconductivity, however, the

charge ordering was too weak to make detailed measurements by neutron scattering. The nature of the static charge stripes in superconducting $La_{1.6-x}Nd_{0.4}Sr_xCuO_{4+\delta}$ will need further clarification. In particular, the glassy feature of the stripes, which recently was observed by measurements[31] of the correlation length of the spin stripes in $La_{1.6-x}Nd_{0.4}Sr_xCuO_{4+\delta}$, has been the subject of intense debate since the possible link between a *electronic liquid-crystal* phase[32] and the *charge stripe* was suggested.

2.4 Charge stripes in $La_{2-x}Sr_xNiO_{4+\delta}$

Charge stripes and spin orderings in hole-doped La_2NiO_4 systems have also attracted intense interest because of the similar structure to that of the cuprates. In fact, hole-doped La_2NiO_4 was the first type of transition-metal oxide observed to show a stripe-like charge and magnetic density modulation. The first evidence for unusual magnetic correlations was obtained in a inelastic neutron scattering[33] study on a single crystal of $La_{1.8}Sr_{0.2}NiO_{4+\delta}$, similar magnetic ordering was also observed in $La_2NiO_{4.125}$[34]. Indication of charge ordering in $La_{2-x}Sr_xNiO_{4+\delta}$ was first reported in electron diffraction and transport measurements[9, 35, 36] on ceramic samples. Following a number of experiments using neutron scattering[21-24, 37-41], carried out on compounds with various hole concentrations, the basic nature of the charge stripes and associated spin ordering has now been fairly well established, although many questions concerning this ordering remain to be answered.

Both La_2NiO_4 and La_2CuO_4 are 2-dimensional antiferromagnetic insulators containing layered MO_2 (M = copper and nickel) planes, which means the coupling of spins within each metal-oxygen plane is much stronger than that between spins in neighbouring planes. When holes are doped into the MO_2 planes, $La_{2-x}Sr_xCuO_4$ eventually shows metallic behaviour and the maximum T_C for superconductivity is reached for $x \approx 0.15$. $La_{2-x}Sr_xNiO_{4+\delta}$ shows very similar metallic behaviour when the

doping level of $x \approx 1$ is reached, but no superconductivity has been observed to date. At sufficiently high level of doping (≥ 0.15 holes/Ni), the added holes, which enter the NiO_2 planes, order into periodically spaced stripes. The Ni spins in the intervening regions order antiferromagnetically, with an antiphase relationship between neighboring domains. These coupled charge- and spin-density modulations align themselves diagonally with respect to the Ni-O bonds, as indicated by the positions of the charge-ordered and magnetic superlattice peaks observed by electron and neutron diffraction. If one makes use of a unit cell with axes rotated by 45° with respect to the Ni-O bonds, then in reciprocal space, the magnetic peaks are split about the antiferromagntic $\boldsymbol{Q}_{AF} = (1, 0, 0)$ along [100] direction by an amount ε, or have the wavevectors $(1 \pm \varepsilon, 0, 0)$ in reciprocal plane $(hk0)$, while the charge-ordered peaks are split about fundamental Bragg peaks by 2ε, or at $(h \pm 2\varepsilon, 0, 1)$.

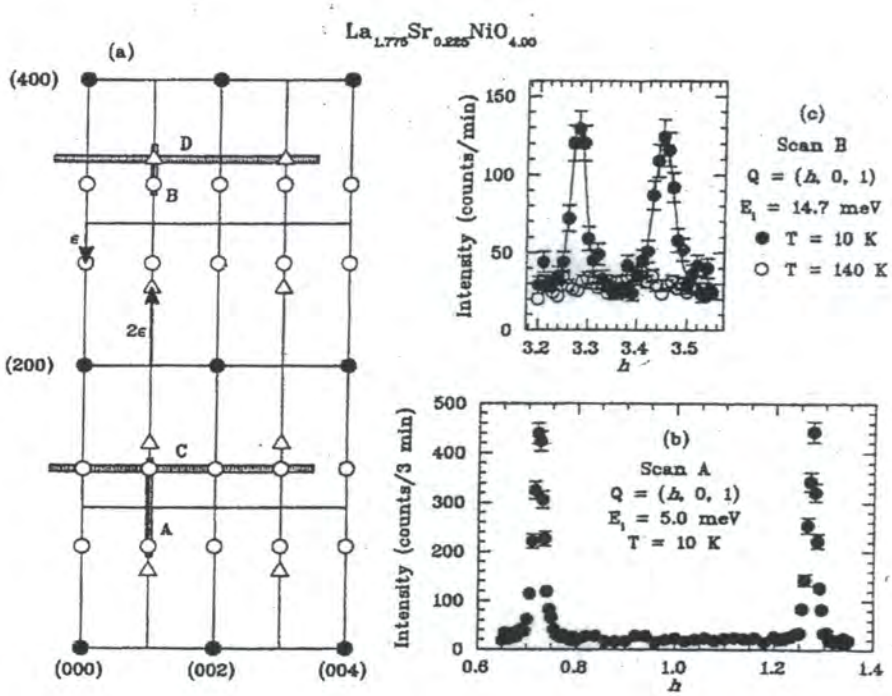

Fig. 2.6 Scans of superlattice peaks in $(h0l)$ zone of reciprocal space of $La_{2-x}Sr_xNiO_4$ ($x = 0.225$)(taken from Tranquada[38])

Fig. 2.6 shows scans through some superlattice peaks in the (*h0l*) zone in $La_{2-x}Sr_xNiO_4$ ($x = 0.225$)[38], with indexing based on space group *F*4/*mmm*, or notation $a = b \approx \sqrt{2}a_p \approx 5.4$Å, $c \approx 12.6$Å. The characteristic wavevector of the charge stripe and spin ordering in $La_{2-x}Sr_xNiO_{4+\delta}$ has been confirmed as,

$$\boldsymbol{Q}_{CO} = (2\varepsilon, 0, 1) \tag{2.3}$$

and

$$\boldsymbol{Q}_{SO} = (1 + \varepsilon, 0, 0) \tag{2.4}$$

The relationship between charge and spin wavevectors indicates that the period of the spin structure in direct space is twice that of the charge modulation. The stripe model[11, 18] in $La_{2-x}Sr_xNiO_{4+\delta}$ is shown in Fig. 2.7. The charge stripes, appearing diagonally with respect to the Ni-O bonds, are antiphase boundaries separating two neighboring AF spin regions. The charge (hole) concentration *along* the stripe is 1 hole/Ni, corresponding to that of ½ hole/Cu in the Nd-doped copper oxide. Another notable difference of the stripe model between the nickelate and the cuprate is the different *l*-dependence of the modulation wavevectors. The requirement that $l = 1$ in nickelate is related to the presence of two NiO_2 layers per unit cell, indicating that the displacement pattern in one layer is exactly opposite to that in the neighboring layers. This result is also consistent with a staggering of the hole stripes from one layer to the next, as one would expect because of Coulomb repulsion. Because the stripes are truly pinned by the LTT phase in the cuprate within a layer, they must rotate by 90° from one layer to the next, to follow the LTT distortion pattern. Thus, a weak interaction between neighbouring orthogonal stripe layers would be expected. As a result, the scattering from the stripes should be essentially two-dimensional in character, with the modulation wavevectors $\boldsymbol{Q}_{CO} = (2\varepsilon, 0, l)$ for the vertical stripe layers and $\boldsymbol{Q}_{CO} = (0, 2\varepsilon, l)$ for the horizontal stripe layers.

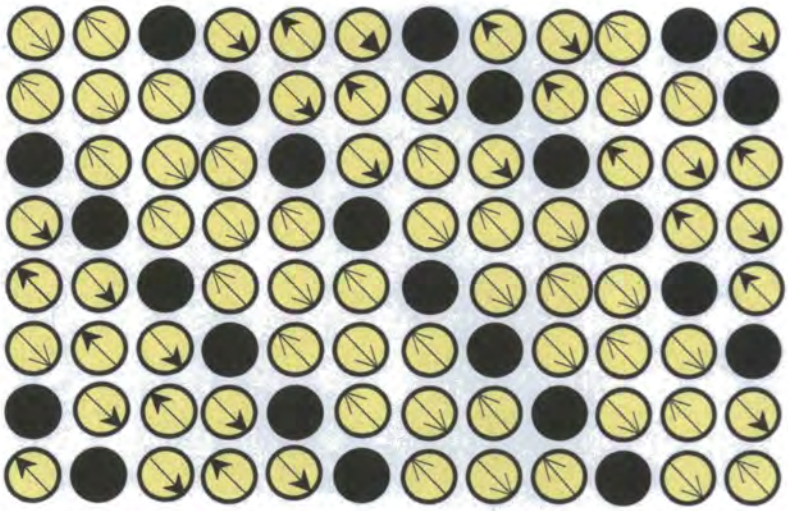

Fig. 2.7 The stripe model for $La_{2-x}Sr_xNiO_4$ (x = 1/4). Arrows indicate the presence of magnetic moments, which are locally antiparallel. holes (black filled circles) are ordered at the antiphase domain bounaries, which run diagonally in NiO_2 lattice square. (taken from Tranquada[11, 18])

2.5 Striped charge and orbital ordering and magnetic coupling in the perovskite manganites $R_{1-x}A_xMnO_3$

2.5.1 Introduction

Manganese oxide perovskites, with the general formula $R_{1-x}A_xMnO_3$, (with R a rare-earth ion such as La, Nd, Pr and A a divalent ion such as Ca, Sr, Ba or Pb), were first discovered in the 1950's[42], and, soon after, their properties were extensively studied[43-46]. The early studies on these compounds already established the extreme complexity of their structural, magnetic and transport phase diagrams as a function of the formal Mn^{4+} content x (hole doping), average A-site cation site $\langle r_A \rangle$ and

temperature. One of the most important findings was the discovery, for appropriate values of x ($0.2 \leq x \leq 0.4$) and $\langle r_A \rangle$, of a sharp metal-insulator (M-I) transition as a function of increasing temperature. The compounds displaying these effects are ferromagnetic (FM) metals at low temperatures, and paramagnetic (PM) insulators at high temperature. The temperature at which the M-I transition occurs, $T_{M\text{-}I}$, was found to coincide with the Curie temperature T_C, where ferromagnetism disappears. The double-exchange (DE) mechanism[46] was then proposed to explain this metallic FM ground state.

The more recent "renaissance" of the research on these manganite perovskites was prompted by a series of measurements, by von Helmholt[47] and by Jin *et al.*[48], showing, near T_C, extremely high values of the magnetoresistance, much larger than the so-called giant magnetoresistance (GMR) for magnetic metallic multi-layers. This phenomenon was then widely termed colossal magnetoresistance (CMR). In addition to the technological potential on information storage, manganite perovskites have proved to be extremely interesting for basic condensed-matter physics. One of the reasons is that the interaction between charge carriers and lattice distortions is unusually strong[49-52], due to the marked differences in the size and coordination of the different manganese oxidation states involved. This strong "electron-phonon" interaction, which can be tuned by varying the electronic doping, electronic bandwidth and disorder, gives rise to a complicated phenomenology, in which crystallographic structure, magnetic structure and transport properties appear to be intimately related. The striped charge ordering and the related orbital and spin ordering represent one of the most intriguing manifestations of these effects in these compounds. Below a certain temperature T_{CO}, electronic carriers become localized onto specific sites, which display long-range order throughout the lattice structure (*charge ordering*). Moreover, the filled Mn^{+3}-e_g orbitals and the associated lattice distortions (elongated Mn-O bonds) also develop long-range order (*orbital ordering*). Finally, the magnetic exchange interaction between neighboring Mn ions, mediated by oxygen ions, become strongly anisotropic at the local level, since Mn-O-Mn

superexchange interactions are ferromagnetic through a filled and empty e_g orbital, but antiferromagnetic through two empty e_g orbitals. This gives rise to complex *magnetic ordering* in the structure. The interaction among charge, orbital and magnetic degree of freedom has been the central issue on the current studies of manganites[53-55].

2.5.2 Lattice structure, electronic states and electron-lattice coupling

The basic structural unit for $R_{1-x}A_xMnO_3$ is the perovskite structure ABO_3 ($Pm3m$), as shown in Fig. 2.8.

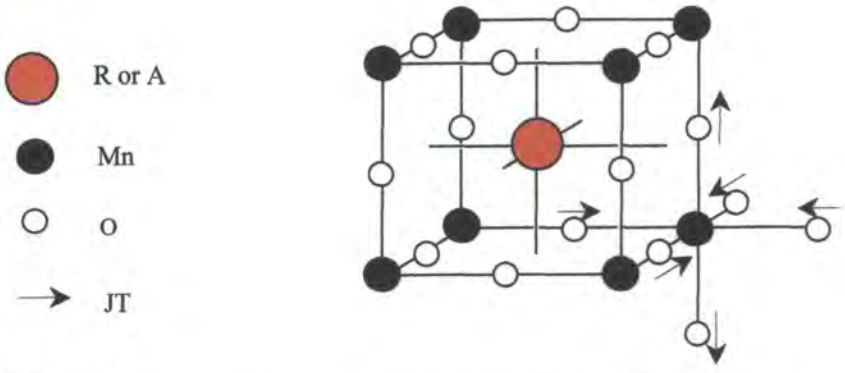

Fig. 2.8 Manganese perovskite and Jahn-Teller (JT) distortions

The $3d$ orbital energy splitting induced by the lattice distortions in perovskite manganites can strongly affect the characteristics of the charge carriers[1, 3, 50, 53, 56]. In the ideal perovskite structure, each Mn is in a locally cubic environment (octahedral site symmetry O_h) and the crystal field splits the five d orbitals into triply degenerate t_{2g} and doubly degenerate e_g states, as shown in Fig. 2.9.(a). The t_{2g} levels seem to lie substantially (~2-4 eV) below the e_g levels. In some layered systems, the site symmetry of the manganese ion becomes tetragonal (D_{4h}) due to the lattice distortion with the elongation of the out-of-plane Mn-O bonding length and the shortening of the in-plane Mn-O ones. Then the e_g orbital energy splits so that the $3d_{x^2-y^2}$ in-plane

orbital energy is separated from the $3d_{3z^2-r^2}$ out-of-plane one. An orthorhombic distortion causes a similar energy splits of the e_g orbital, as shown in Fig. 2.9.(a).

The on-site Coulomb repulsion is apparently strong enough that (i) no $3d$ orbital may be occupied by more than one electron and (ii) all electron spins on a given Mn are ferromagnetically aligned by a large Hund's rule coupling. The resulting physical picture is thus that 3 of the (4-x) d electron fill up the t_{2g} levels, forming an electronically inert core spin S_C of magnitude 3/2, while the remaining (1-x) electron goes into a linear combination of e_g orbitals and may move through the crystal[50]. The electronic states in the manganites, $Mn^{3+}(3d^4: t_{2g}^3 e_g^1)$ and $Mn^{4+}(3d^3: t_{2g}^3)$, are shown in Fig. 2.9 (b).

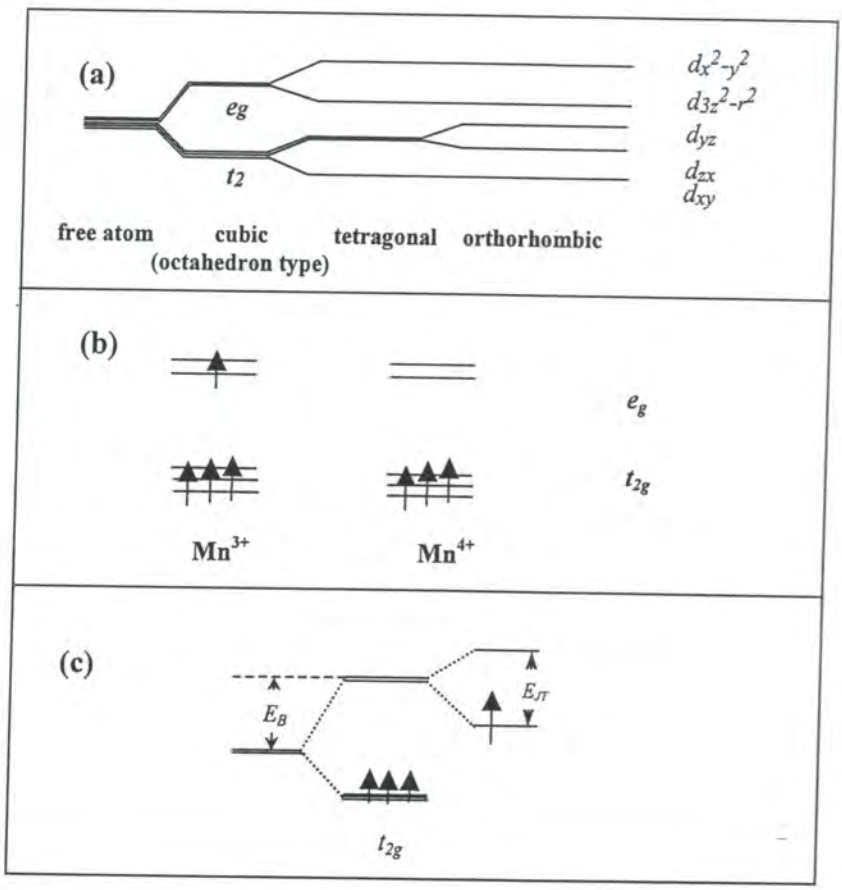

Fig. 2.9 Electronic states of Mn ions in the perovskite manganites[1, 50, 53]

When the double occupancy of the e_g orbitals is prohibited, there appears an additional internal degree of freedom for the e_g electrons to occupy either the $d_{x^2-y^2}$ or the $d_{3z^2-r^2}$ orbital, due to the degeneracy of the e_g orbitals. Therefore, the e_g electrons have two internal degrees of freedom, that is, spin and orbital[53, 56]. It has been pointed out that the spin and orbital couple with each other in manganites to produce a variety of ordering states, that is, *orbital ordering*.

The degeneracy in the e_g orbitals may bring about a Jahn-Teller lattice distortion[50]. There are three important electron-phonon coupling modes: a "breathing" distortion of O_6 octahedral around a given Mn which couples to change in the e_g charge density, and two linearly independent even-parity uniaxial volume-preserving distortions (JT modes) which couple to preferential occupancy of one e_g orbital over the other. One such distortion, indicated by arrows in Fig. 2.8, involves a stretching of the Mn-O bonds along z and compression in the x-y planes. A schematic energy level of the Mn ion is shown in Fig. 2.9 (c), the central portion of which is for the undistorted lattice. The right-hand portion of the Figure shows that if the e_g level is singly occupied, a Jahn-Teller (JT) distortion of the surrounding O_6 octahedra may occur, which would split the e_g doublet by an energy E_{JT}. Hence, the doped hole can only go into the out-of-plane $3d_{3z^2-r^2}$ orbital, which is energetically lowered by the JT distortion. The left-hand portion of the figure shows that if the e_g level is unoccupied, a "breathing model" may occur which lowers the energy of the unoccupied e_g doublet by an amount E_B relative to its energy in the ideal structure.

2.5.3 The charge, orbital and spin degree of freedom and related ordering phenomena

The charge, orbital and spin degree of freedom are three very important internal parameters which provide a rich variety of magnetic, transport and structural properties of the perovskite manganites $R_{1-x}A_xMnO_3$[57]. The undoped $R_{1-x}A_xMnO_3$ (x = 0) is an AF insulator, with a layered spin structure, the so-called A-type AF[43], as shown in Fig. 2.10 (a), in which the exchange coupling in the a-b plane (Mn-O plane)

is ferromagnetic, but along the *c*-axis, the neighbouring layers are AF coupled. In this case, the orbital and spin degrees of freedom, which are strongly associated with each other and also correlated with Jahn-Teller (JT) distortions, largely dictate the ground state of this system. Which e_g orbitals, (x^2-y^2)- or $(3z^2-r^2)$-type, are occupied by $3d$ electrons provides an important clue to understanding the exchange coupling between spins. The model of a $(3x^2-r^2/3y^2-r^2)$-type orbital ordering in the *a-b* plane accompanied by JT distortions, as shown in Fig. 2.10 (a), was proposed[44, 58, 59] to explain the observed A-type magnetic correlations. This kind of orbital ordering type in $LaMnO_3$ was recently confirmed by a resonant x-ray scattering study[60].

In the low doping range, i.e. the region of $0.1 < x \leq 0.5$, a FM metallic ground state appears for most $R_{1-x}A_xMnO_3$ compounds, and in the region of $0.5 \leq x < 1$, various types of AF ordering appear. Because the holes are doped into Mn^{3+} sites, some of the e_g orbitals are not occupied. The charge degree of freedom then regains importance. The charge-ordered phases were observed to be accompanied by AF ordering. The charge ordering (CO) state tends to be stable at $x = 0.5$, where the e_g orbitals are half occupied. The least distorted $La_{0.5}Sr_{0.5}MnO_3$ is a FM metal below Curie temperature (T_C) and a PM metal above T_C without charge ordering[61]. Strongly distorted $Pr_{0.5}Ca_{0.5}MnO_3$ ($T_{CO} \sim 230K$)[62, 63] and $Nd_{0.5}Ca_{0.5}MnO_3$ ($T_{CO} \sim 220K$)[64] become CO insulators below charge-ordering temperature (T_{CO}) and do not show ferromagnetism. $La_{0.5}Ca_{0.5}MnO_3$ ($T_{CO} \sim 160K$)[12, 55, 65] and $Nd_{0.5}Sr_{0.5}MnO_3$ ($T_{CO} \sim 150K$)[66], which are located between the two extremes, undergo a FM metal to an AF charge-ordered insulators. Most of the CO states in these compounds were suggested to have a CE-type AF ordering[43, 62]. This model was originally proposed by Goodenough[44, 59] to interpret the large AF superstructure found for the $La_{0.5}Ca_{0.5}MnO_3$ as evidence of charge ordering and a possible orbital ordering pattern. In this model, as shown in Fig. 2.10 (b), Mn^{3+} and Mn^{4+} are arranged in a checkerboard pattern in the *a-b* plane and the Mn^{3+} sites have JT distortions.

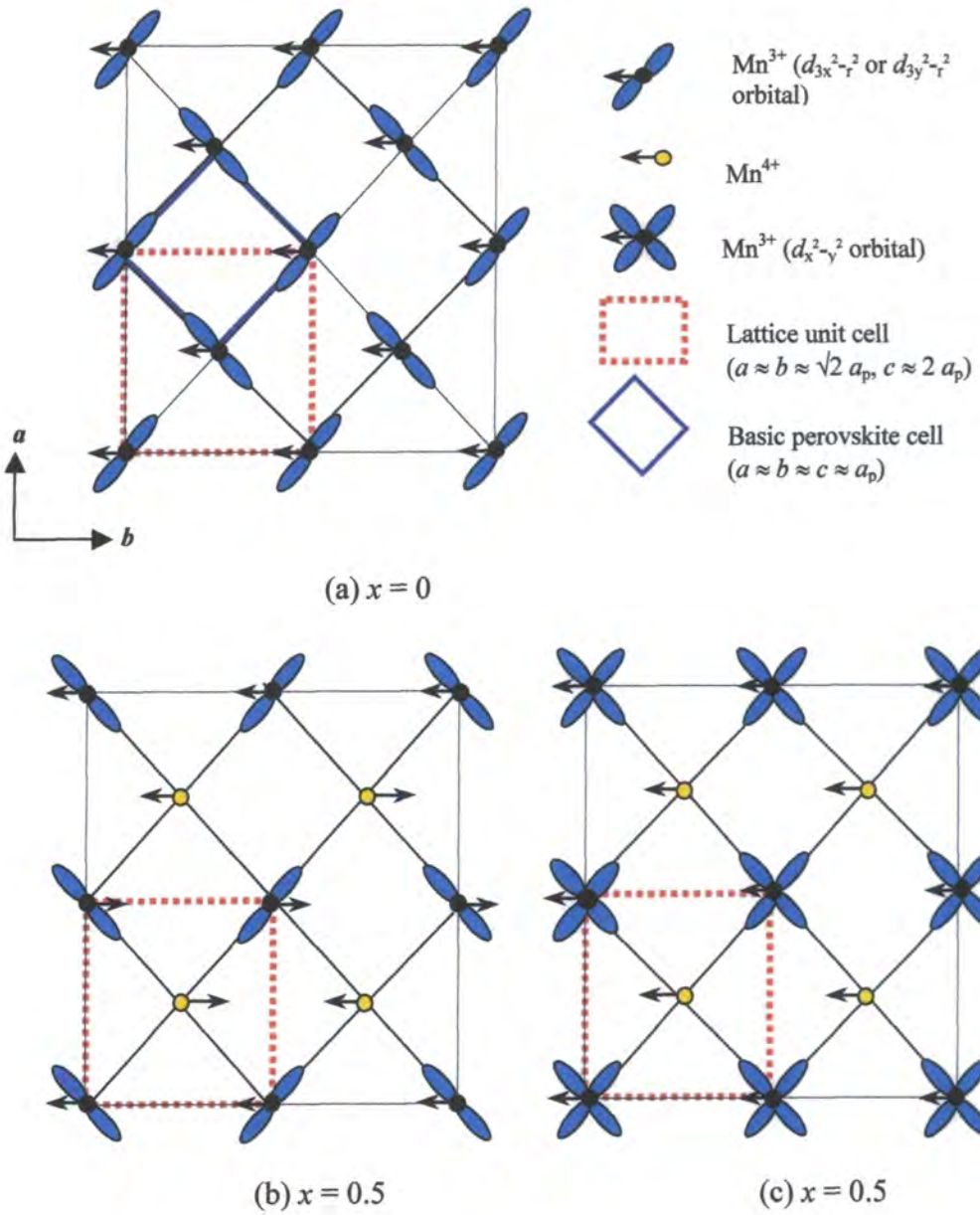

(a) $x = 0$

(b) $x = 0.5$

(c) $x = 0.5$

Fig. 2.10 Examples of CE-type and A-type charge, orbital and spin ordering in $R_{1-x}A_xMnO_3$

Since the exchange coupling between Mn^{3+} and Mn^{4+} depends on which type of e_g orbital is occupied at the Mn^{3+} site, the orbital degree of freedom at Mn^{3+} site appears important as well. The $(3x^2\text{-}r^2/3y^2\text{-}r^2)$-type orbital ordering, as shown in Fig. 2.10 (b), is quite possible. However, this type of orbital ordering has not been observed directly until now. Along the *c*-axis, the same in-plane arrangement of Mn^{3+} and Mn^{4+} is stacked and the neighboring planes are AF coupled, as shown schematically in Fig. 2.11.On the other hand, not all half-doped CO AF insulators are CE-types, a neutron diffraction study[67] on $Pr_{0.5}Sr_{0.5}MnO_3$ ($T_N \sim 130K$[68]) showed that A-type AF ordering sets in below T_N, as shown in Fig. 2.10 (c), where the in-plane exchange coupling was FM. The $(x^2\text{-}y^2)$-type orbital ordering shown in Fig. 2.10 (c), which couples with the in-plane breathing-type lattice distortion, is expected to be favoured in the A-type AF CO state.

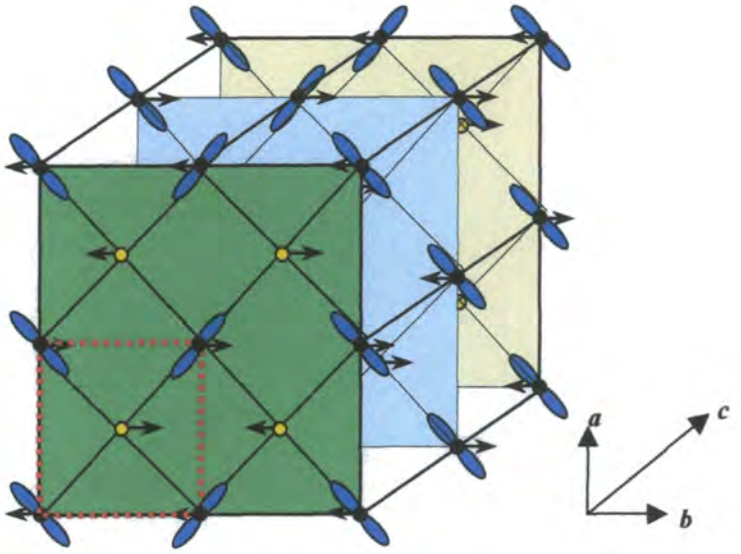

Fig. 2.11 The schematic 3D view of a CE-type ordering

2.5.4 The phase diagram of $La_{1-x}Ca_xMnO_3$

The compound $La_{1-x}Ca_xMnO_3$ is the prototype of the mixed-valent manganites. The richness of the chemical phase diagram was noted even as early as the 1950's when Wollan and Koehler[43] demonstrated that a wide variety of magnetic structure existed in $La_{1-x}Ca_xMnO_3$ as a function of the stoichiometry, x. The details of the phase diagram of the manganite compounds, however, have only recently been explored in detail, and only $La_{1-x}Ca_xMnO_3$ has been examined through the full range of doping[3, 69-72]. In Fig. 2.12, this phase diagram[72] is displayed as a function of Ca concentration and temperature. At high temperature, the spins are not ordered, the material is paramagnetic and the conductivity is high. The FM conducting ground state which results in CMR exists only for $0.2 < x < 0.5$. For $x > 0.5$, the ground state is AF and is charge ordered. The concentration regime near $x = 0.5$ boundary is of particular interest since this is the regime where the FM conducting ground state becomes unstable with respect to a charge-ordered AF state. The competition between different ground states leads to a strongly first-order transition between FM and AF behaviour, which is also characterised by a commensurate to incommensurate charge ordering[12, 55, 71, 73].

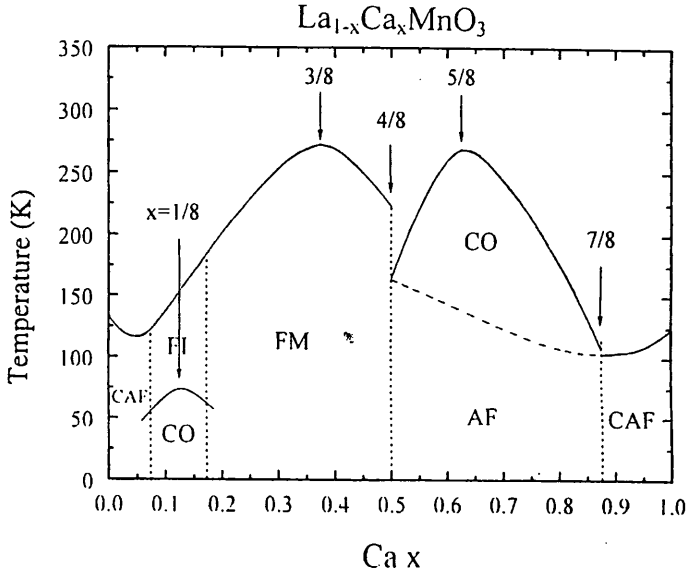

Fig. 2.12 The phase diagram of $La_{1-x}Ca_xMnO_3$ (taken from Cheong[72])

2.5.5 Direct observation: TEM studies of stripe formation in charge-ordered $La_{1/3}Ca_{2/3}MnO_3$

The first direct space image of charge stripes was obtained by a high resolution TEM study on $La_{1/3}Ca_{2/3}MnO_3$, as shown in Fig. 2.13 (c)[13]. The ordering of the rows of Mn^{4+} and Mn^{3+} ions gives rise to a vertical striped pattern with a bright-dark contrast. The periodicity along the transverse direction of the stripes is ~ 16.5 Å. Further evidence from electron diffraction is shown in Fig. 2.13 (a) and (b), which represents an [001] zone-axis electron diffraction obtained from a selected area at a temperature of 95K. The sharp but weak spots that can be indexed with fractional indices are superlattice spots due to charge stripes. The modulation wavevector of the charge ordering as measured from the nearest fundamental Bragg reflection can be written as,

$$\boldsymbol{Q}_{CO} = (\delta, 0, 0) \text{ or } (0, \delta, 0) \tag{2.5}$$

in reciprocal lattice units with $\delta = 1/3$. It should be noted that δ tends to vary slightly (10%) from area to area within the sample and may not always adopt the commensurate value of 1/3. It was also determined that the two perpendicular modulation wavevectors actually originate from different domains of the samples[13, 72].

The modulation wavevector, δ, of the charge ordering depends upon the doped charge carrier concentration. For a hole concentration of x, the ratio of Mn^{4+} to Mn^{3+} ions is $x / (1-x)$[13, 72]. From a number of measurements on various charge-ordered $La_{1-x}Ca_xMnO_3$ compounds, δ was found to equal to $1 - x$ for $x \geq 0.5$,

$$\delta \approx 1 - x \; (x \geq 0.5) \tag{2.6}$$

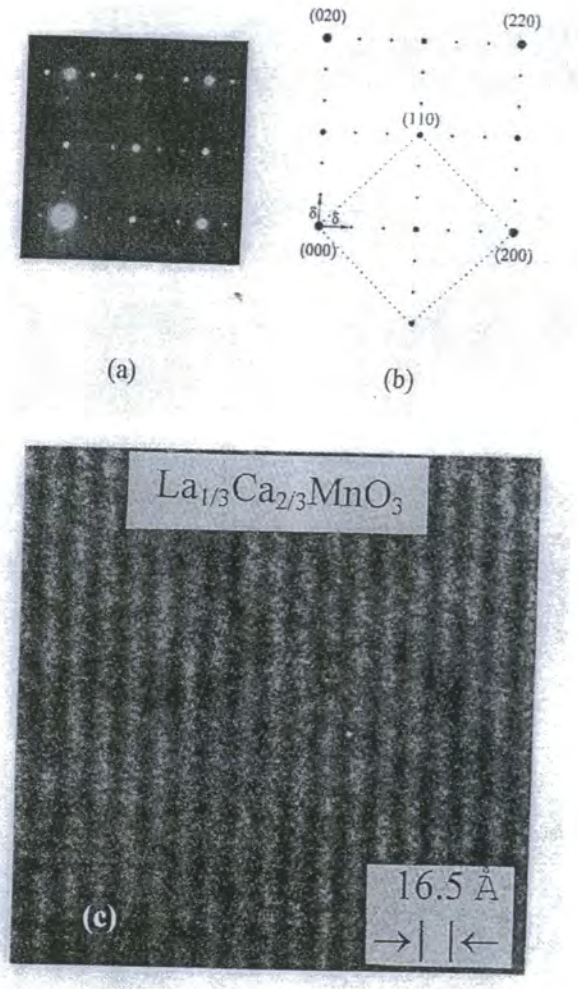

Fig. 2.13 The electron diffraction and TEM image of charge stripes in $La_{1-x}Ca_xMnO_3$ (taken from Chen & Cheong[13, 72])

As mentioned before, there exists a sharp phase boundary between the FM metallic and the CO AF ground states at $x = 0.5$. The strongly-first-order feature of a transition from FM to AF was identified by transport measurements[69, 70]. The intriguing features of the charge stripe was further revealed by TEM experiments[12, 72]. First, the

charge ordering undergoes an incommensurate to commensurate transition between 240 and 130K. Second, the incommensurate charge stripe coexists with ferromagnetism in a narrow temperature range. The charge ordering phenomenon is mutually exclusive with ferromagnetism in the double exchange mechanism, which requires a charge carrier hopping from a Mn^{3+} ion across an intervening O^{2-} ion to an adjacent Mn^{4+}. More recently, such kinds of competition and coexistence between FM metallic and charge-ordered AF phases have been further confirmed, and suggested to result from a mesoscopic-scale electronic phase separation[74-77].

2.5.6 Paired stripes in $La_{1-x}Ca_xMnO_3$

Very recent experiments[74, 78] have revealed that $La_{1-x}Ca_xMnO_3$ has a more complex charge stripe structure than previously believed. Using a very high resolution (less than 3Å) TEM, it was found that the two stripes form a stable *pair* in direct space, and that these paired stripes repeat periodically, as shown in Fig. 2.14, for $La_{1/3}Ca_{2/3}MnO_3$. The micrograph shown in the upper panel of Fig. 2.14 exhibits a regular array of paired, dark-blue fringes, separated by orange stripes. A schematic model is shown in the lower panel of Fig. 2.14. The doublet fringes were suggested as being produced by the $(3x^2\text{-}r^2/3y^2\text{-}r^2)$-type orbital ordering of adjacent Mn^{3+} ions (shown in blue) that were oriented perpendicular to one another. The sharing of electrons between the anisotropic orbitals of Mn^{3+} and its six oxygen neighbors causes a distortion of lattice due to the JT effect, the resulting strain produced the high-contrast blue regions in the image. The regions around the isotropic Mn^{4+} ions (shown in orange) are much less distorted and exhibit less contrast. The paired $Mn^{3+}O_6$ stripes stick together even when the hole doping level changes. Increasing the relative number of Mn^{4+} ions simply increases the separation between $Mn^{3+}O_6$ stripes. These paired JT stripes therefore were suggested to be the fundamental building blocks of the charge-ordered state in perovskite manganites, and may thus be expected to have profound implications for the magnetic and transport properties of these materials. The discovery of paired stripes also highlights the importance of the

orbital ordering. Recently, it was argued that a *Wigner Crystal* model, rather than *Stripe* model would give a more suitable description for the comprehensive observations on $La_{1/3}Ca_{2/3}MnO_3$ by powder neutron and x-ray scattering[79].

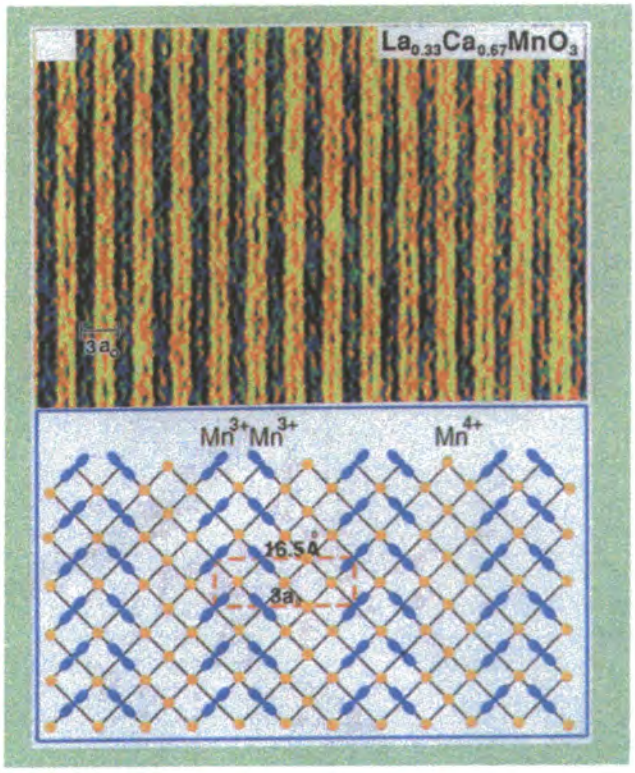

Fig. 2.14 A TEM image and schematic model for the paired stripes in $La_{1-x}Ca_xMnO_3$ ($x = 2/3$) (taken from Mori, Chen & Cheong[78, 80])

2.6 References

1 M. Imada, A. Fujimori, and Y. Tokura, Reviews of Modern Physics **70**, 1039 (1998).

2 V. J. Emery and S. A. Kivelson, Physica C **263**, 44 (1996).

3 A. P. Ramirez, Journal of Physics-Condensed Matter **9**, 8171 (1997).

4 J. G. Bednorz and K. A. Muller, Zeitschrift Fur Physik B-Condensed Matter **64**, 189 (1986).

5 J. D. Jorgensen, B. Dabrowski, S. Y. Pei, *et al.*, Physical Review B-Condensed Matter **38**, 11337 (1988).

6 E. Dagotto, Reviews of Modern Physics **66**, 763 (1994).

7 A. Bianconi, S. Dellalonga, C. Li, *et al.*, Physical Review B-Condensed Matter **44**, 10126 (1991).

8 A. Bianconi, C. X. Li, F. Campanella, *et al.*, Physical Review B-Condensed Matter **44**, 4560 (1991).

9 C. H. Chen, S. W. Cheong, and A. S. Cooper, Physical Review Letters **71**, 2461 (1993).

10 J. H. Cho, F. C. Chou, and D. C. Johnston, Physical Review Letters **70**, 222 (1993).

11 J. M. Tranquada, B. J. Sternlieb, J. D. Axe, *et al.*, Nature **375**, 561 (1995).

12 C. H. Chen and S. W. Cheong, Physical Review Letters **76**, 4042 (1996).

13 C. H. Chen, S. W. Cheong, and H. Y. Hwang, Journal of Applied Physics **81**, 4326 (1997).

14 J. M. Tranquada, J. D. Axe, N. Ichikawa, *et al.*, Physical Review B-Condensed Matter **54**, 7489 (1996).

15 J. M. Tranquada, Journal of Superconductivity **9**, 397 (1996).

16 J. M. Tranquada, J. D. Axe, N. Ichikawa, *et al.*, Physical Review Letters **78**, 338 (1997).

17 J. M. Tranquada, Physica C **282**, 166 (1997).

18 J. M. Tranquada, Journal of Physics and Chemistry of Solids **59**, 2150 (1998).

19 V. J. Emery and S. A. Kivelson, Physica C **209**, 597 (1993).

20 J. M. Tranquada, D. J. Buttrey, and D. E. Rice, Physical Review Letters **70**, 445 (1993).

21 J. M. Tranquada, D. J. Buttrey, V. Sachan, *et al.*, Physical Review Letters **73**, 1003 (1994).

22 J. M. Tranquada, D. J. Buttrey, J. E. Lorenzo, *et al.*, Physica B **213**, 69 (1995).

23 V. Sachan, D. J. Buttrey, J. M. Tranquada, *et al.*, Physical Review B-Condensed Matter **51**, 12742 (1995).

24 J. M. Tranquada, J. E. Lorenzo, D. J. Buttrey, *et al.*, Physical Review B-Condensed Matter **52**, 3581 (1995).

25 A. R. Moodenbaugh, Y. W. Xu, M. Suenaga, *et al.*, Physical Review B-Condensed Matter **38**, 4596 (1988).

26 J. D. Axe, A. H. Moudden, D. Hohlwein, *et al.*, Physical Review Letters **62**, 2751 (1989).

27 M. K. Crawford, R. L. Harlow, E. M. McCarron, *et al.*, Physical Review B-Condensed Matter **44**, 7749 (1991).

28 G. Burns and A. M. Glazer, *Space Group for Solid State Scientists* (Academic Press, Boston, 1990).

29 N. M. Plakida, *High-temperature Superconductivity : experiment and theory* (Springer, Berlin, New York, 1995).

30 G. Burns, *High-temperature Superconductivity : an introduction* (Academic Press, Boston, 1992).

31 J. M. Tranquada, N. Ichikawa, and S. Uchida, cond-mat/9810212 (1998).

32 S. A. Kivelson, E. Fradkin, and V. J. Emery, Nature **393**, 550 (1998).

33 S. M. Hayden, G. H. Lander, J. Zarestky, *et al.*, Physical Review Letters **68**, 1061 (1992).

34 K. Yamada and *et al.*, Physica C **221**, 355 (1994).

35 S. W. Cheong, C. H. Chen, H. Y. Hwang, *et al.*, Physica B **199**, 659 (1994).

36 S. W. Cheong, H. Y. Hwang, C. H. Chen, *et al.*, Physical Review B-Condensed Matter **49**, 7088 (1994).

37 J. E. Lorenzo, J. M. Tranquada, D. J. Buttrey, *et al.*, Physical Review B-Condensed Matter **51**, 3176 (1995).

38 J. M. Tranquada, D. J. Buttrey, and V. Sachan, Physical Review B-Condensed Matter **54**, 12318 (1996).

39 J. M. Tranquada, P. Wochner, A. R. Moodenbaugh, *et al.*, Physical Review B-Condensed Matter **55**, R6113 (1997).

40 P. Wochner, J. M. Tranquada, D. J. Buttrey, *et al.*, Physica B **241**, 877 (1997).

41 P. Wochner, J. M. Tranquada, D. J. Buttrey, *et al.*, Physical Review B-Condensed Matter **57**, 1066 (1998).

42 G. H. Jonker and J. H. Van Santen, Physica **16**, 337 (1950).

43 E. O. Wollan and W. C. Koehler, Physical Review **100**, 545 (1955).

44 J. B. Goodenough, Physical Review **100**, 564 (1955).

45 G. H. Jonker, Physica **22**, 707 (1956).

46 C. Zener, Physical Review **82**, 403 (1951).

47 R. von Helmolt, J. Wecker, B. Holzapfel, *et al.*, Physical Review Letters **71**, 2331 (1993).

48 S. Jin, T. H. Tiefel, M. McCormack, *et al.*, Science **264**, 413 (1994).

49 A. J. Millis, Journal of Applied Physics **81**, 5502 (1997).

50 A. J. Millis, Nature **392**, 147 (1998).

51 A. J. Millis, Philosophical Transactions of the Royal Society of London Series a- Mathematical Physical and Engineering Sciences **356**, 1473 (1998).

52 H. Roder, J. Zang, and A. R. Bishop, Physical Review Letters **76**, 1356 (1996).

53 J. Inoue, Philosophical Transactions of the Royal Society of London Series a-Mathematical Physical and Engineering Sciences **356**, 1481 (1998).

54 D. I. Khomskii and G. A. Sawatzky, Solid State Communications **102**, 87 (1997).

55 P. G. Radaelli, D. E. Cox, M. Marezio, *et al.*, Physical Review B-Condensed Matter **55**, 3015 (1997).

56 J. Inoue, Journal of Physics D-Applied Physics **31**, 643 (1998).

57 A. Fujimori and T. Mizokawa, in *Colossal Magnetoresistance, Charge Ordering and Related Properties of Manganese Oxides*, edited by C. N. R. Rao and B. Raveau (World Scientific, Singapore, 1998), p. 279.

58 J. Kanamori, J. Phys. Chem. Solids **10**, 87 (1959).

59 J. B. Goodenough, A. Wold, R. J. Arnott, *et al.*, Physical Review **124**, 373 (1961).

60 Y. Murakami, J. P. Hill, D. Gibbs, *et al.*, Physical Review Letters **81**, 582 (1998).

61 A. Urushibara, Y. Moritomo, T. Arima, *et al.*, Physical Review B-Condensed Matter **51**, 14103 (1995).

62 Z. Jirak, S. Krupicka, and Z. Simsa, Journal of Magnetism and Magnetic materials **53**, 153 (1985).

63 Y. Tomioka, A. Asamitsu, H. Kuwahara, *et al.*, Physical Review B-Condensed Matter **53**, R1689 (1996).

64 T. Vogt, A. K. Cheetham, R. Mathendiram, *et al.*, Physical Review B **54**, 15303 (1996).

65 P. G. Radaelli, D. E. Cox, M. Marezio, *et al.*, Physical Review Letters **75**, 4488 (1995).

66 H. Kuwahara, Y. Tomioka, A. Asamitsu, *et al.*, Science **270**, 961 (1995).

67 H. Kawano, R. Kajimoto, H. Yoshizawa, *et al.*, Physical Review Letters **78**, 4253 (1997).

68 Y. Tomioka, A. Asamitsu, Y. Moritomo, *et al.*, Physical Review Letters **74**, 5108 (1995).

69 P. Schiffer, A. P. Ramirez, W. Bao, *et al.*, Physical Review Letters **75**, 3336 (1995).

70 A. P. Ramirez, P. Schiffer, S. W. Cheong, *et al.*, Physical Review Letters **76**, 3188 (1996).

71 A. P. Ramirez, S. W. Cheong, and P. Schiffer, Journal of Applied Physics **81**, 5337 (1997).

72 S.-W. Cheong and C. H. Chen, in *Colossal Magnetoresistance, Charge Ordering and Related Properties of Manganese Oxides*, edited by C. N. R. Rao and B. Raveau (World Scientific, Singapore, 1998), p. 241.

73 P. G. Radaelli, G. Iannone, D. E. Cox, *et al.*, Physica B **241**, 295 (1997).

74 S. Mori, C. H. Chen, and S. W. Cheong, Physical Review Letters **81**, 3972 (1998).

75 P. Calvani, G. DeMarzi, P. Dore, *et al.*, Physical Review Letters **81**, 4504 (1998).

76 G. Allodi, R. DeRenzi, G. Guidi, *et al.*, Physical Review B-Condensed Matter **56**, 6036 (1997).

77 G. Allodi, R. DeRenzi, F. Licci, *et al.*, Physical Review Letters **81**, 4736 (1998).

78 S. Mori, C. H. Chen, and S. W. Cheong, Nature **392**, 473 (1998).

79 P. G. Radaelli, D. E. Cox, L. Capogna, *et al.*, cond-mat/9812366 (1998).

80 A. J. Millis, Nature **392**, 438 (1998).

Chapter 3

Charge Stripes (II): Impact on the physics of transition-metal oxides

3.1 Introduction

Since the discovery of charge stripes and related orbital and spin ordering in various transition-metal oxides[1-4], a number of intriguing phenomena related to stripes have been experimentally observed and/or theoretically predicted. Stripe physics is developing into an important area of condensed matter physics.

In this chapter, the current impact of striped charge ordering on strongly correlated electron physics is reviewed. The organisation is as follows, in Section 3.2, incommensurate spin fluctuations, or dynamic stripes in copper oxides, which have been extensively studied before the discovery of the static stripe, are briefly reviewed. Static charge and spin stripes were suggested as the pinning of incommensurate spin fluctuations. The relationship between stripes and high-T_C superconductivity is discussed in this section. In section 3.3, the physics of colossal magnetoresistance (CMR) in a number of manganites, and related metal-insulator transitions (MIT) are represented. Roles played by striped charge, orbital and spin orderings in CMR manganites, are also revealed. Section 3.4 provides a theoretical consideration on charge stripes and related aspects. Main mean-field theories of stripes are summarised, in particular, a number of mechanisms for producing stripe phases, such as *frustrated phase separation* and *a Fermi-surface instability* are briefly described. Two models for explaining CMR, *double exchange (DE)* and *ferromagnetic Kondo*

model (FK), strongly associated with stripe physics, are also given in this section. Furthermore, two of the most interesting theoretical predictions, *electronic liquid-crystal phases* and *phase separation*, and their comparison to experiments, are mentioned as well.

3.2. Stripes *vs.* Superconductivity

3.2.1 Introduction

The discovery of charge stripes by Tranquada[2] has shown that the suppression of superconductivity in $La_{1.6-x}Nd_{0.4}Sr_xCuO_{4+\delta}$ ($x = 0.12$) is associated with the formation of charge-striped antiphase domain walls between antiferromagnetically ordered spins in the CuO_2 planes. The concept of a striped phase, not only provides an explanation for the unique behaviour of the La_2CuO_4 family of compounds near to 1/8 doping, but also strongly supports the idea, that the low energy incommensurate (IC) spin fluctuation observed in cuprate superconductors is probably the dynamic analogue of charge stripes[2, 5-7]. Connections between static stripes and dynamical spin fluctuations have been revealed from a number of experimental evidence, e.g., magnetic fluctuations in superconducting $La_2Sr_{2-x}CuO_4$ are characterized by a doping-dependent incommensurate wavevector[8], and, for a given Sr concentration, the wavevector found in samples with and without Nd are essentially identical[9]. More recently, it has been reported that spin fluctuations in underdoped $YBa_2Cu_3O_{6+x}$ ($x = 0.6$)[10, 11] have an incommensurate component, and that the spatial orientation of the modulation wavevector is identical with that in $La_{2-x}Sr_2CuO_4$. It is becoming increasingly apparent that low energy IC spin fluctuations are universal to the high T_C superconductors[9, 12].

Much recent interest on the stripe model in cuprates has focused on the observation of static IC magnetic ordering which coexists with superconductivity in certain La_2CuO_4-based systems. Following the observation of elastic IC magnetic ordering in $La_{1.6-x}Nd_{0.4}Sr_xCuO_{4+\delta}$ (x = 0.12, 0.15 and 0.20)[2, 5, 6, 9, 12] compounds, it has also been directly confirmed by elastic neutron scattering that similar static IC magnetic ordering exists at doping level near x = 1/8 even in the absence of Nd^{3+}-doping, e.g., $La_{2-x}Sr_xCuO_4$ (x = 0;10, 0.12 and 0.13)[13, 14] and excess-oxygen-doped La_2CuO_{4+y}[12]. However, there are still no reports for the observation of associated charge ordering peaks in these systems, which will be essential to finally clarify the stripe model proposed for cuprates.

3.2.2 Incommensurate (IC) spin fluctuations in high T_C superconductors

The most celebrated common feature of copper oxide magnetism is that the undoped parent compounds are insulating antiferromagnets, characterised by a simple $\boldsymbol{Q}_{AF}$ = (1/2, 1/2), or a doubling of the crystallographic unit cell along the [110] direction in the *I*4/*mmm* tetragonal notation. Neutron scattering, which measures the Fourier transform of spin-spin correlation function, imaged the doubling that manifests itself in diffraction peaks at the wavevector (½, ½) in the reciprocal space. It is also well known that chemical doping leads to a suppression of the long-range AF ordering followed by a metal-insulator transition and superconductivity, as shown in the phase diagram in Fig. 2.1, and that the elastic neutron diffraction peaks at (½, ½), due to AF magnetic ordering, disappear. However strong inelastic scattering derived from spin fluctuations persist in both AF and superconducting compositions. The difference is that, in the small doping range, e.g., $0 \leq x \leq 0.05$ for $La_{2-x}Sr_xCuO_4$, or the AF regime, dynamic spin fluctuations are commensurate with a modulation wavevector (½, ½), while spin fluctuations instead become incommensurate centered at (½, ½) in the higher doping level, superconducting regime, as shown in schematically Fig. 3.1,

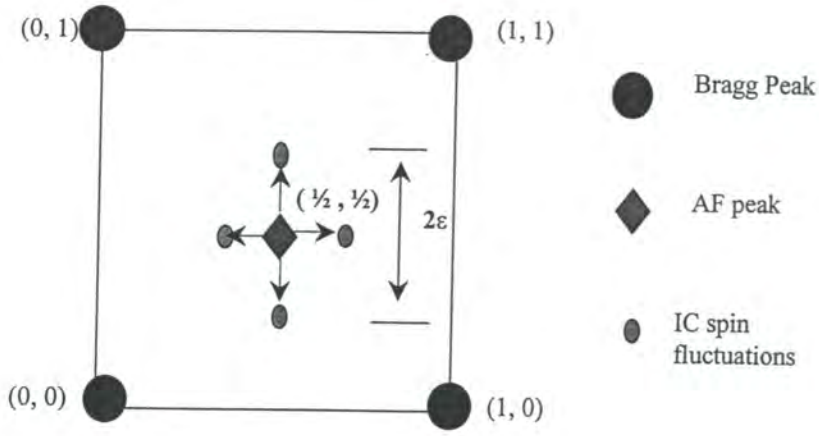

Fig. 3.1 a schematic configuration of the AF peak and IC spin fluctuations in reciprocal space

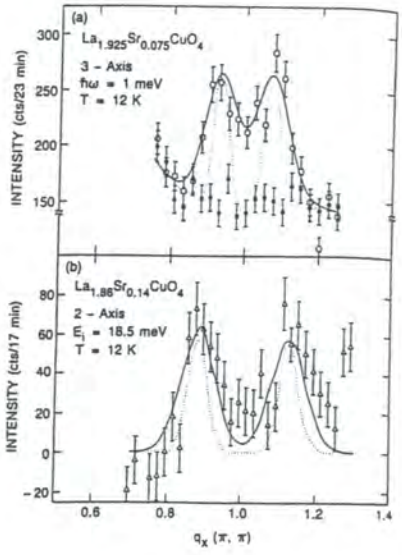

Fig. 3.2 Low energy IC magnetic response in metallic $La_{2-x}Sr_xCuO_4$ for two compositions (x = 0.075 and x = 0.14). The data are scans in momentum transfer through two of the four peaks that appear at (π, π) ± (π, 0) and (π, π) ± (0, π). The upper panel is for an energy transfer of 1meV, the lower is energy integrated using an incident neutron energy of 18.55meV. (taken from Cheong[8])

Evidence for incommensurate magnetic fluctuations in $La_{2-x}Sr_xCuO_4$ compounds was first provided by the inelastic neutron scattering study of Cheong[8], as shown in Fig. 3.2.

The AF position can be described as (½, ½) in reciprocal space, when scans were performed along q_x and q_z, the two pairs of split peaks centered at (½, ½) were detected, which can be described as followed,

$$\boldsymbol{Q}_{IC} = (\tfrac{1}{2} \pm \delta, \tfrac{1}{2}) \text{ and } (\tfrac{1}{2}, \tfrac{1}{2} \pm \delta) \qquad (3.1)$$

The incommensurability δ has been found to have a strong hole-doping dependence[15], as shown in Fig. 3.3, which indicates that $\delta \approx x$ for $0.05 \leq x \leq 1/8$, and $\delta \approx 1/8$ for $x \geq 1/8$.

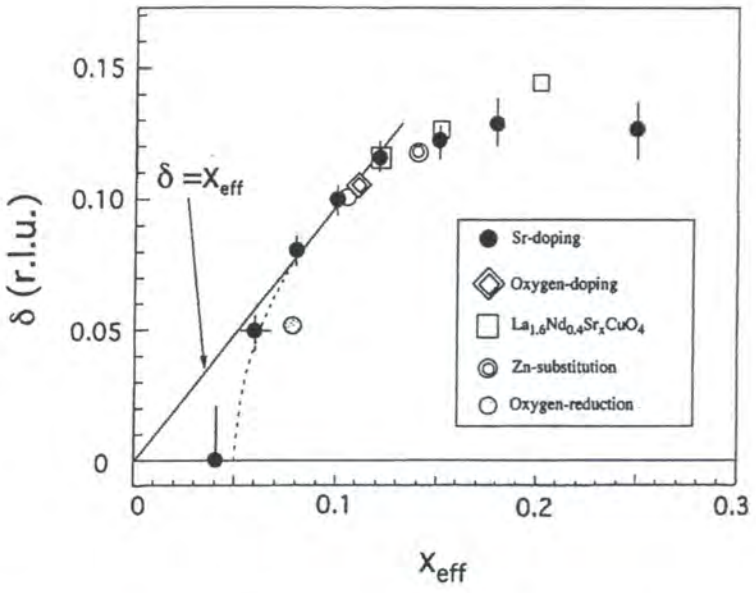

Fig, 3.3 Incommensurability δ, of spin fluctuations in $La_{2-x}Sr_xCuO_4$ and related systems plotted as a function of the effective doping level. (taken from Yamada[15])

Very recently, a two-dimensional inelastic neutron scattering study of $YBa_2Cu_3O_{6.6}$ was reported, which revealed that low-frequency spin fluctuations are virtually identical to those of similarly doped $La_{2-x}Sr_xCuO_4$[10]. Thus, the high-temperature ($T_C \leq 92$ K) superconductivity of Y123 may be related to spatially coherent low-frequency spin excitations that were previously thought to be unique to the lower-T_C (≤ 40 K) single-layer $La_{2-x}Sr_xCuO_4$ family. Fig. 3.4 shows the reciprocal space diagram and neutron-scattering results, which clearly indicates the existence of low-energy incommensurate spin fluctuations with the wavevectors ($\frac{1}{2} \pm \delta, \frac{1}{2}$) and ($\frac{1}{2}, \frac{1}{2} \pm \delta$).

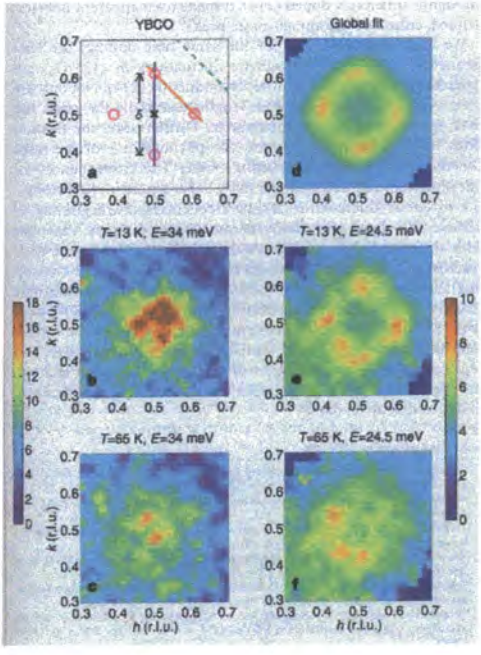

Fig. 3.4 Images of the magnetic scattering from $YBa_2Cu_3O_{6.6}$ above and below T_C at 34 and 24.5 meV in the two dimensional reciprocal space of the CuO_2 planes. At the lower energy (e) and (f), an IC response, described by the model shown in (d), appears at the positions noted in the schematic map, (a). (taken from Mook[10])

Summarising considerable experimental evidence, it has been proposed that IC spin fluctuations are actually universal features in copper oxides[9, 12]. In addition, IC spin fluctuations have also been suggested as spatial and temporal fluctuating stripes.

3.2.3 The "1/8 effect" – pinning of dynamic stripes in superconductors

The explanation for the "1/8 effect" by Tranquada built a link between charge stripes observed in $La_{1.6-x}Nd_{0.4}Sr_xCuO_4$ ($x = 0.12$) and IC spin fluctuations in some high-T_C copper superconductors. It was suggested that certain pinning effects, such as lattice distortions etc., could pin dynamic spin fluctuations into the static stripe formation in CuO_2 planes[2, 5, 7].

With increasing x, the long-range AF order in both $La_{2-x}Sr_xCuO_4$ and $La_{2-x}Ba_xCuO_4$ is destroyed; both of them move through a spin-glass-like disordered phase (SG) and eventually become superconducting at dopant concentrations of 0.07 and 0.05, respectively (see the phase diagram in Fig. 2.1). However, at $x \approx 0.115$ in $La_{2-x}Sr_xCuO_4$ and $x \approx 0.125$ in $La_{2-x}Ba_xCuO_4$, superconductivity is suppressed and magnetic order reemerges – this phenomenon is known as the "1/8 effect"[16, 17].

Successive transitions in $La_{1.875}Ba_{0.125}CuO_4$ from a high-temperature tetragonal (HTT) to a low-temperature orthorhombic (LTO), to a low-temperature tetragonal (LTT) structural phase[17], involve successive distortions or rotations of the CuO_6 octahedral. $La_{1.6-x}Nd_{0.4}Sr_xCuO_{4+\delta}$ has a very similar transition from LTO to LTT[18]. Thus, a stripe mechanism has been proposed to explain the "1/8 effect" as the pinning of the dynamic magnetic correlation. Dynamic spin fluctuations, which were observed as the inelastic magnetic peaks, are stabilised by some "pinning" mechanism because inelastic and elastic reflections are observed at the same position. The distortions associated with the LTO→ LTT transitions in $La_{1.6-x}Nd_{0.4}Sr_xCuO_{4+\delta}$ and $La_{1.875}Ba_{0.125}CuO_4$ have been proposed as a pinning mechanism by Tranquada. The formation of charge stripes, or charge and magnetic ordering detected by neutron

scattering, is driven by the LTO→ LTT transition, as shown by the temperature dependence measurement in Fig. 2.5, in which the charge and spin stripes only appear once the LTO-LTT transition was completed. The pinning of dynamic magnetic correlation, seen in superconducting samples of $La_{2-x}Sr_xCuO_4$, or static charge and spin stripes has a dramatic effect on the suppression of superconductivity. Noting that $La_{1.6-x}Nd_{0.4}Sr_xCuO_{4+\delta}$ samples with the largest magnetic ordering parameter also have the lowest T_C, Tranquada *et al.* indicated that static stripe ordering and superconductivity compete with each other[6].

3.2.4 Challenges: static charge and spin ordering in high T_C superconductors

Recent experiments have been able to provide the evidence for elastic spin ordering in La_2CuO_4-based compounds, which was previously reported only in $La_{1.6-x}Nd_{0.4}Sr_xCuO_{4+\delta}$ (x = 0.12, 0.15 and 0.20) compounds. As discussed above, it was speculated that the LTT phase is essential for static magnetic ordering in superconductors. Experiments on $La_{2-x}Sr_xCuO_4$, however, show that the existence of the LTT structural phase is not a necessary condition for the appearance of static magnetic ordering. Based on NMR studies of $La_{2-x}Sr_xCuO_4$ (x = 0.115) and $La_{2-x}Ba_xCuO_4$ (x = 0.125), Goto *et al.* conclude that magnetic ordering exists even in the absence of the LTT structure[19]. More direct evidence has come from recent neutron scattering experiments on $La_{2-x}Sr_xCuO_4$ single crystals with x = 0.10, 0.12 and 0.13, all of which have the LTO structure[13, 14]. Experimental reports on La_2CuO_{4+y} provide some interesting features[12]. For incommensurabilities very near 1/8, the elastic magnetic peak intensity appears at the same temperature as the superconductivity within the errors, suggesting that the two phenomena are strongly correlated. A plausible explanation of the elastic magnetic ordering observed in $La_{2-x}Sr_xCuO_4$ and La_2CuO_{4+y} is a stripe model similar to that proposed to describe $La_{1.6-x}Nd_{0.4}Sr_xCuO_{4+\delta}$. However, new elastic magnetic peaks at positions $(1/2 \pm \varepsilon/2, 1/2 \pm \varepsilon/2)$ in $La_{2-x}Sr_xCuO_4$ (x = 0.05), which are rotated by 45° with respect to those

previously reported, were observed recently, this result gives rise to more challenges for the theories of high-T_C superconductivity[20].

The model of stripes proposed by Tranquada involves two sets of assumptions, one is the modulation of spin correlation, which can be characterized with the wavevector $(1/2 \pm \varepsilon, ½)$ and $(1/2, ½ \pm \varepsilon)$ in reciprocal space, the other is the charge ordering modulation with wavevector $(\pm 2\varepsilon, 0)$ and/or $(0, \pm 2\varepsilon)$. In particular, the charge ordering peak is conclusive evidence of the stripe model. The charge ordering peak has only been successfully measured in the compounds of $La_{1.6-x}Nd_{0.4}Sr_xCuO_{4+\delta}$ (x = 0.12 and 0.15) by neutron scattering, further confirmed by x-ray diffraction[21]. Therefore, the direct detection of the charge ordering by various scattering experiments on La_2CuO_4-based compounds, in which the static magnetic ordering has been observed, would be essential to clarify the stripe model, thus remains as a challenge for the future of stripe physics.

3.3 Stripes *vs.* CMR

3.3.1 Introduction

Studies of CMR in $R_{1-x}A_xMnO_3$ have brought novel features related to the striped charge ordering in these oxides[22-25]. The striped charge ordering in the manganites, which was usually accompanied with orbital and spin ordering, is interesting because the double-exchange (DE) gives rise to a metallic state along with ferromagnetism (FM) while the charge-ordered state is associated with insulating and antiferromagnetic (AFM) behaviour. The competition between FM with metallic behaviour and the striped charge/orbital ordering with insulating behaviour lead to some most intriguing properties in manganites. In particular, charge stripes in some manganites can be melted into a metallic FM state by the application of a magnetic

field. This kind of field-induced metal-insulator transition (MIT) has been regarded as one of the major origins of CMR phenomena[25-28]. The direct relationship between the stripe order and CMR has attracted intensive interest since then.

3.3.2 Phenomenology of the CMR

Magnetoresistance (MR) is the relative change in the electrical resistance or resistivity of a material produced on the application of a magnetic field. It is generally defined by,

$$MR = \Delta R / R(0) = [R(H) - R(0)] / R(0) \qquad (3.2)$$

Where $R(H)$ and $R(0)$ are the resistance or resistivity at a given temperature in the presence and absence of a magnetic field, H, respectively. MR can be negative or positive. Most metals show a small MR (only a few percent). In non-magnetic pure metals and alloys MR is generally positive and the MR shows a quadratic dependence on H. MR can be negative in magnetic materials because of the suppression of spin disorder by the magnetic field. Large magnetoresistance, referred to as giant magnetoresistance (GMR), was first observed on the application of magnetic fields to metallic superlattices, such as Fe/Cr[29] and Cu/Co[30, 31]. At room temperature, resistance changes $\Delta R/R(0)$ was typically observed to be as high as 40% in Cu/Co multilayers[30, 31]. GMR is a result of the reduction of the extra resistance due to the spin-dependent scattering at the interface between ferromagnetic and nonmagnetic regions. The MR observed in $R_{1-x}A_xMnO_3$ manganites with perovskite structure can be very large, close to 100% in some compounds, which has been called CMR, as distinct from GMR in layered or granular metallic materials. In fact the resistance ratio (RR),

$$RR = R(0) / R(H) \qquad (3.3)$$

is more realistic since it shows clearly how many orders of magnitude of the resistance can be decreased by applying a magnetic field. The first series of investigation made in 94-95 on thin films and sintered ceramics of CMR manganites, showed that extremely high *RR*, up to 10^{11}, can be reached. A typical CMR behaviour is shown in Fig. 3.5, which represents the magnetization, resistivity and magnetoresistance of $La_{1-x}Ca_xMnO_3$ ($x = 0.25$) as a function of temperature at various magnetic fields[32]. As sample is cooled through the FM transition, the resistivity, ρ, peaks sharply and drops rapidly—changing from hopping to metallic conduction. In a magnetic field, the FM transition is broadened and shifted to higher temperature. The shifting of the peaks in ρ results in a large MR near T_C, and indeed the MR, also plotted in bottom panel of Fig. 3.5, is sharply peaked near the transition. The behaviour near T_C can be understood at least qualitatively in terms of the DE model, and quantitative comparisons can be made when the model is extended to include strong electron-lattice interaction related to the Jahn-Teller (JT) distortions.

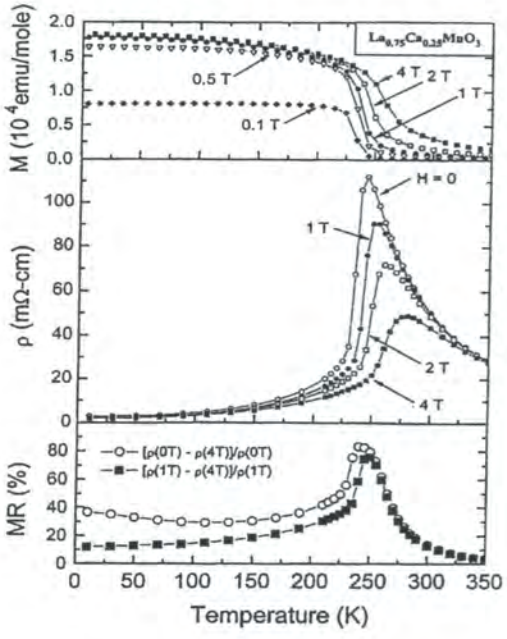

Fig. 3.5 The Magnetization, resistivity, and magnetoresistance of $La_{1-x}Ca_xMnO_3$ ($x = 0.25$) as a function of temperature at various fields. (taken from Schiffer *et al.*[32])

Although it is phenomenally the same from the viewpoint of magnetoresistance properties for all perovskites manganites, there are two distinguishing CMR behaviours depending on the ground states of the manganites. As discussed in Chapter 2, in the low doping range $0.1 < x < 0.5$, a FM metallic state (FMM) appears for most $R_{1-x}A_xMnO_3$, and in the region of $0.5 \leq x < 1$, an AF insulating (AFI), charge-ordered state could appear in some compounds[24]. Thus the behaviour of the type I manganites can be described by a PM insulating state (PMI) to FMM transition with decreasing temperature, and the type II manganites exhibits a similar PMI to FMM transition, at T_C, with decreasing temperature, but differing from type I, by the existence of a FMM to AFI transition at T_N when the temperature is further decreased. Both types of manganites exhibit negative CMR properties when submitted to a magnetic field. $La_{1-x}Ca_xMnO_3$ ($x = 0.25$), as shown in Fig. 3.5, is a example of the type I. $Nd_{1-x}Sr_xMnO_3$ ($x = 0.5$)[33] is a type II manganite with a striped charge/orbital ordering below T_{CO}, whose temperature dependence of magnetisation (top panel), lattice parameters (middle panel) and resistivity (bottom panel) in a single crystal sample is shown in Fig. 3.6. Upon the charge ordering transition, resistivity shows a jump by several orders of magnitude, simultaneously the FM magnetization disappears due to the AF spin ordering and the lattice parameters in the orthorhombic structure (*Pbnm*) show an abrupt change characteristic of the first-order phase transition. The CMR in $Nd_{1-x}Sr_xMnO_3$ ($x = 0.5$) is highly related to a field-induced collapse of the charge ordering in AF ground state. Therefore, the CMR behaviour of the type II manganites is nothing but an insulator-metal transition (MIT) driven by an external magnetic field.

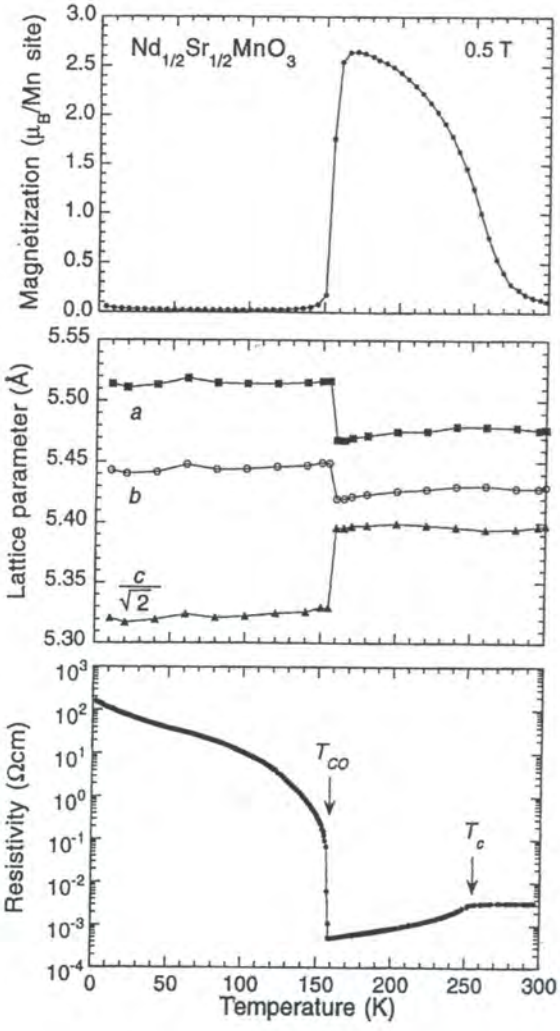

Fig. 3.6 Temperature dependence of the magnetization (top) (measured at a magnetic field of 0.5 T), lattice parameters (middle), and resistivity (bottom) in a crystal of $Nd_{1-x}Sr_xMnO_3$ ($x = 0.5$). (taken from Kuwahara *et al.*[33])

3.3.3 The field-induced metal-insulator transition in stripe-ordered manganites

Metal-insulator transitions (MIT) are accompanied by huge resistivity changes, even over tens of orders of magnitude, and are widely observed in condensed matter systems[27]. The MIT in CMR manganites has been a central issue since the realization, that the CMR could occur with a field-induced transition. A clear case where the field-induced MIT is observed is in the collapse of the charge-ordered state under an external magnetic field. Thus it is quite clear that the CMR of the type II manganites is directly related to the charge stripe.

For those perovskite manganites compounds, there exist two crucial microscopic control parameters, which can largely modify the electron correlation strength and resultant properties of transport, magnetism and lattice structure. One is a carrier density (hole-doping level) x or band filling $(1 - x)$ of the conduction band. The other control parameter is an effective one-electron bandwidth (W), or equivalently e_g electron transfer interaction (t). The magnitude of W is changed by varying the averaged ionic radius of the A site, or equivalently the tolerance factor (f), defined as followed[28, 34-36],

$$f = (\langle r_A \rangle + \langle r_O \rangle) / [\sqrt{2}(r_{Mn} + r_O)] \qquad (3.4)$$

here, $\langle r_A \rangle$ is the averaged ionic radius of the A site, r_{Mn} and r_O are the ionic radii for the respective elements Mn and O. In general, the smaller the averaged ionic radius of A site or f is, the smaller W is. Another way to control W is by application of external pressure (P): the W-value can be more finely increased with P through the contraction of Mn-O bond length or a straightening a Mn-O bond angle[37-41].

The electronic phase diagrams[27] of some representative perovskites of general formula $R_{1-x}A_xMnO_3$ is shown in Fig. 3.7, these include (a) $La_{1-x}Sr_xMnO_3$, (b) $Nd_{1-x}Sr_xMnO_3$, (c) $La_{1-x}Ca_xMnO_3$, (d) $Pr_{1-x}Ca_xMnO_3$. As the tolerance factor, f, or

equivalently the averaged ionic radius of perovskite A site decreases from (La, Sr) to (Pr, Ca) through (Nd, Sr) and (La, Ca), orthorhombic distortion increases, resulting in the decrease of W. With reduced W, or equivalently e_g electron transfer interaction (t), other electronic instabilities, such as JT-type electron-lattice coupling, charge/orbital ordering, and AF superexchange interactions, may become important and compete with FM double-exchange interaction. Therefore, as shown in Fig. 3.7, when W is decreased (f is decreased), the FM state becomes to be apparently absent, as observed for $Pr_{1-x}Ca_xMnO_3$. Around a middle-W region, i.e., $Nd_{1-x}Sr_xMnO_3$ and $La_{1-x}Ca_xMnO_3$ compounds, the subtle balance or competition between the FM double-exchange and the AF charge-ordering interaction complicate the phase diagram, possibly leading to CMR of the type II. $La_{1-x}Sr_xMnO_3$ is the most canonical double-exchange system with maximal W, thus dominated by the FM in the phase diagram, leading to a type I of CMR.

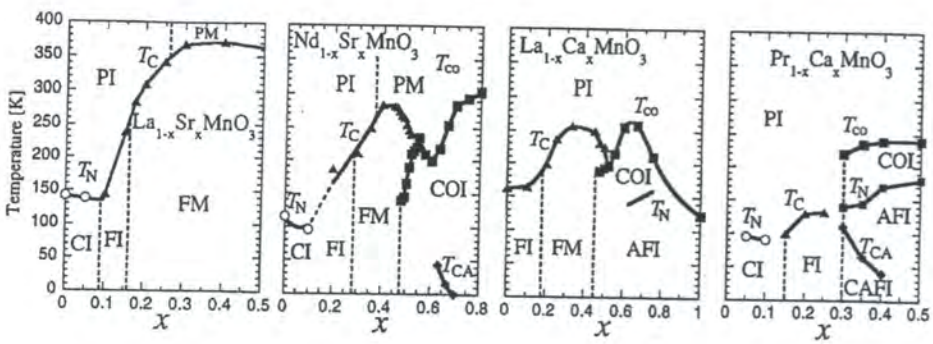

Fig. 3.7 Electronic phase diagrams in the plane of the doping concentration x and temperature for representative distorted perovskites of $R_{1-x}A_xMnO_3$: (a) $La_{1-x}Sr_xMnO_3$; (b) $Nd_{1-x}Sr_xMnO_3$; (c) $La_{1-x}Ca_xMnO_3$; and (d) $Pr_{1-x}Ca_xMnO_3$. States denoted by abbreviations: PI, paramagnetic insulating; PM, paramagnetic metallic; CI, spin-canted insulating; COI, charge-ordered insulating; AFI, antiferromagnetic insulating (in the COI); CAFI, canted antiferromagnetic insulating (in the COI). (taken from Imada, Fujimori & Tokura[27])

The MIT relevant to the charge/orbital ordering phenomena under various values of W and x, has been extensively investigated. A typical example of the charge/orbital ordering transition in $Nd_{1-x}Sr_xMnO_3$ (x = 0.5)[42] is shown in Fig. 3.6. According to a neutron scattering study[43], the FMM to AFI transition can be assigned to the phase transition to the striped charge/orbital state, in which the nominally Mn^{3+} and Mn^{4+} species show a CE-type ordering, as shown in Fig. 2.11. The ($3x^2 - r^2$ / $3y^2 - r^2$) type orbital ordering show superlattice along b-axis on the (001) plane (*Pbnm* notation). Reflecting such an orbital ordering, the spin ordering shows a complicated superstructure with 4 × 4 ×2 unit cell in the pseudo-cubic perovskite setting ($a = b = c = a_p$), and the stripes of the homovalent Mn ions are along the c-axis. The same CE-type charge/orbital ordering was also reported for $La_{1-x}Ca_xMnO_3$ (x = 0.5)[4, 32, 44-46] and $Pr_{1-x}Ca_xMnO_3$ (x = 0.5)[47-49]. Fig. 3.8 displays the temperature dependence of resistivity under various magnetic fields for $Nd_{1-x}Sr_xMnO_3$ (x = 0.5). The resistivity near T_C (= 255K) is much reduced by applying an external field, since the field forcibly aligns the t_{2g} local spins and hence the DE carriers gain a mobility due to a reduced spin scattering. This is the conventional MR effect which is generally seen around T_C in the manganites showing the FM ground state. In addition to such a canonical MR, a more remarkable field effect, i.e., six orders of magnitude change in resistivity, is seen in the charge-ordered state. The critical temperature of the CO transition, that accompanies the thermal hysteresis characteristic of the first-order phase transition, is decreased by increasing a magnetic field. The charge-ordered AFI state is totally extinguished over the whole temperature range by applying a field larger than 7T. Such a magnetic-field-induced destruction of the charge-ordered state can be viewed as one of major origins of the CMR effect.

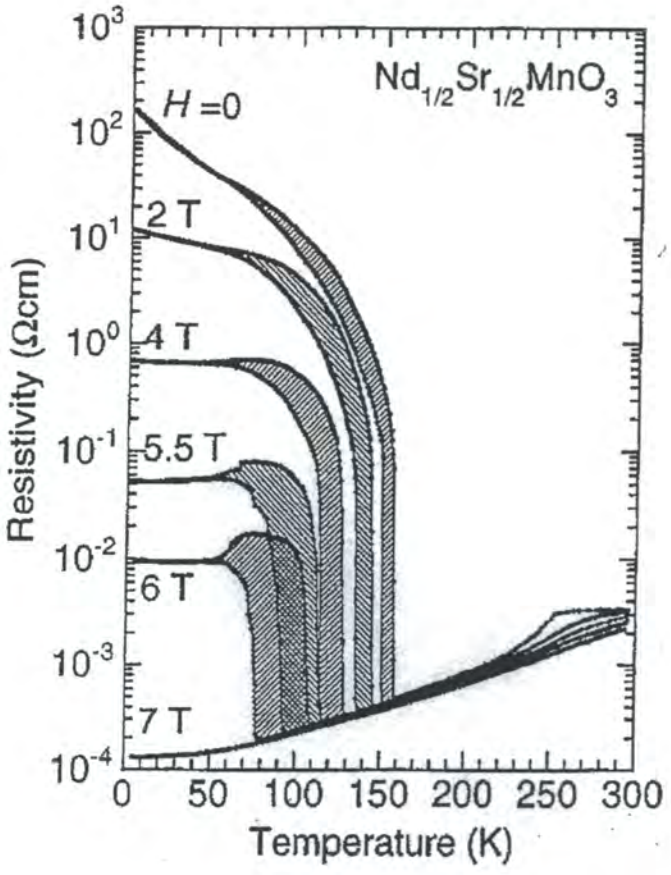

Fig. 3.8 Temperature dependence of resistivity for $Nd_{1/2}Sr_{1/2}MnO_3$ crystal under several magnetic fields. (taken from Tokura *et al*[42])

The charge-ordered insulating state appears to be extended over a wider doping region (x) when W is further narrowed, as can be seen for $0.3 \leq x \leq 0.7$ in the case of $Pr_{1-x}Ca_xMnO_3$, in contrast to the case of $Nd_{1-x}Sr_xMnO_3$ with a larger W-value where the CO state emerges only in the limited region in the vicinity of $x = 0.5$. For $Pr_{1-x}Ca_xMnO_3$ ($x = 0.5$), a larger external magnetic field is needed to destroy the CO insulating state than in Nd-Sr compound. It was recently realized that the irradiation with x-rays[50], a nanosecond laser pulse[51], and an electric field[52] can also cause the

transient or permanent melting of the charge-ordered state as well as MIT in this compound. These observations may open a new field for externally induced metal-insulator transitions.

3.4 Theories regarding stripe formation

3.4.1 Introduction

Even before the discovery of the experimental evidence of stripe phases, a number of theories predicated the possible existence of striped charge domain walls in an antiferromagnetic background, such as a CuO_2 plane in hole-doped superconducting copper oxides. These domain walls were originally proposed to explain the IC spin fluctuations observed in $La_{2-x}Sr_xCuO_4$ compounds.

Charge stripes exhibit quite different behaviours, which are strongly associated with the different microscopic parameters in cuprates, nickelates and manganites as discussed in the previous sections, so it is extremely hard to develop an universal theory for stripe physics. However, all of the parent compounds which show striped charge ordering when charge carriers are introduced chemically, are antiferromagnetic Mott insulators, whose insulating behaviour is due to strong electron correlations. Therefore, most mechanisms for explaining the origin of the stripe phase and related properties have been based on the theories of doped Mott insulators.

3.4.2 Mean-field theories of the Hubbard model

The charged domain wall in doped high-T_C oxides was first predicated theoretically using the Hartree-Fock (HF) approximation of mean-field theory applied to a

Hubbard model[53], and such kind of stripe instability was also confirmed by a number of subsequent investigations.

Most theories of strongly correlated electron system begin with the Hubbard Model because of its simplicity[54]. This is a model in which band electrons interact via a two-body repulsive Coulomb interaction. No phonons are present and in general no explicitly attractive interactions are included. This simple model is believed to contain the basic physics of a CuO_2 plane in high-T_C oxides. The second quantized Hamiltonian of a single-band two-dimensional Hubbard model[54, 55] on a square lattice, with hopping restricted to nearest neighbors (indicated by the bracket $<i, j>$) is shown as follows,

$$H = -t \sum_{<ij>,\sigma} (c^{\dagger}_{i,\sigma} c_{j,\sigma} + H.c.) + U \sum_{i} n_{i,\uparrow} n_{i,\downarrow} \tag{3.5}$$

Where $c^{\dagger}_{i,\sigma}$ and $c_{i,\sigma}$ creates and destroys an electron with spin σ at site i, respectively, and $n_{i,\sigma} = c^{\dagger}_{i,\sigma} c_{i,\sigma}$. U is the on-site Hubbard repulsion and t the transfer parameter. The Coulomb interaction is assumed to be screened, thus only the on-site term U is kept. The t and U are two important internal parameters deciding the electronic states of the Hubbard model.

For small values of the Hubbard on-site repulsion U (generally smaller than $3t \sim 4t$), these calculations resulted in a striped phase oriented along either the (10) or (01) direction, whereas for higher values of U the orientation is along the diagonals as observed experimentally in the nickelates[55]. In particular, a multiband Hubbard model HF calculation[56] gave a correct and even quantitatively description of the ground state of doped nickelates, where the stripes were first observed.

However, all stripe calculations performed so far within the HF approximation of the Hubbard model predict one hole per site along the striped domain wall (filled stripe).

This is the case in the nickelates, but quite contrasts the observation of half-filled stripes (one hole per two sites) in Nd-doped copper oxides. Despite a recent calculation[55] of Hubbard model in the presence of long-range Coulomb interactions predicting the existence of a half-filled stripe, the hole concentration along stripe is a yet unresolved problem of mean-field theory.

3.4.3 Two mechanisms: Coulomb-frustrated phase separation and a Fermi-surface instability

Two mechanisms for producing a stripe phase have been suggested by theories of doped Mott-Hubbard insulators: a Fermi-surface instability[53, 57-60] and frustrated phase separation[61, 62]. The Fermi-surface instability relies on Fermi-surface nesting which leads to a reduced density of states, or a gap, at the Fermi energy. In this mechanism, the spins form antiphase domains that are stabilized by holes bound to the domain walls. In this scenario, spin and charge order together, or charge stripe order following after spin order, which is contrary to the experimental observation of a charge-driven stripe in $La_{1.6-x}Nd_{0.4}Sr_xCuO_{4+\delta}$ ($x = 0.12$).

In the frustrated phase separation mechanism, a competition in doped Mott-insulators between the tendency of macroscopic phase separation and the long-range part of the Coulomb interaction leads to charge-ordered phases, and especially to stripe formation. A classical Ising pseudo-spin model[62] was given to study the competition between short-range FM coupling and long-range AFM Coulomb interaction, which is a coarse-grained representation of frustrated phase separation in high-T_C copper oxides, as shown in Eq. (3.6),

$$H = K\sum_j S_j^2 - L\sum_{<ij>} S_i S_j + \frac{Q}{2}\sum_{i\neq j}\frac{\mathbf{S}_i\mathbf{S}_j}{r_{ij}} \qquad (3.6)$$

Where L, $Q > 0$, represents the strength of the FM and AF interactions, respectively, and $S_j = \pm 1,0$ specifies the charge at site j of a two-dimensional square lattice. $S_j = +1$ and $S_j = -1$ correspond to hole-rich and hole-poor phases, whereas $S_j = 0$ indicates that the local density is equal to the average value. The quadrupolar field K controls the concentration of sites at which $S_j^2 = 1$. The solution of this simple model confirms that the local charge inhomogeneity and the stripe phase are expected consequences of frustrated phase separations.

In order to minimize their kinetic energy, the holes attempt to separate into hole-rich regions and hole-poor regions with significant local AF correlations. However, phase separation is frustrated by the long-range Coulomb interaction between holes. The hole forms an array of metallic stripes, whose period is determined by the energetics of phase separation and is unrelated to any nesting wavevector of the Fermi surface. The charge ordering, in turn, drives the antiphase ordering of the spin stripe domains. The experiments on $La_{1.6-x}Nd_{0.4}Sr_xCuO_{4+\delta}$ ($x = 0.12$)[2] were proposed to favour this point of view. One interpretation[63] of the ARPES experiments on $Bi_2Sr_2CaCu_2O_{8+\delta}$ gave further support to this mechanism: a Fermi-surface nesting would lead to a diminished density of states at the Fermi surface, whereas an increased density of states corresponding to the flat bands was seen in the experiments.

3.4.4 Density matrix renormalization group (DRMG) studies of the *t-J* model

More recently, the stripe phase in 2D doped antiferromagnets was also revealed by numerical density matrix renormalization group (DRMG) calculations[64-66] for a *t-J* model with a hole doping $x = 1/8$, the energetics of the domain walls in a 2D *t-J* model with various hole concentration x was also studied. The *t-J* Hamiltonian in the subspace of no doubly occupied sites is given by,

$$H = -t\sum_{<ij>s}(c_{is}^{\dagger}c_{jk} + H.c.) + J\sum_{<ij>}(\boldsymbol{S}_i \cdot \boldsymbol{S}_j - \frac{n_i n_j}{4}) \qquad (3.7)$$

Here <*ij*> are near-neighbor sites, *s* is a spin index, $\boldsymbol{S}_i$ is electron spin, and $c_{is}^{\dagger}$ and c_{jk} are creation operators. The near-neighbour hopping interaction is t and the near-neighbour exchange interaction is J.

For a 16 × 8 cluster of a *t-J* system (J/t = 0.35), at x = 1/8, the domain walls with a filling of ½ hole per domain wall unit cell (half-filled domain walls), separating π-phase-shifted AF regions, were spaced four lattice spacings apart, which was in agreement with neutron scattering results for $La_{1.6-x}Nd_{0.4}Sr_xCuO_{4+\delta}$ (x = 0.12). Based on further DRMG calculations, it was found that the ground state always has striped domain walls for doping $0 < x \leq 0.3$. For $x \leq 1/8$, the system has (1,0) domain walls (horizontal or vertical type) with the hole concentration of ½ hole per domain wall unit along the stripe, and the inverse domain spacing $d^{-1} = 2x$ was also found. This scenario is quite consistent with experiments. For $x \geq 0.17$, the domain walls was a filled stripe and having $d^{-1} = x$. However, more experimental tests of these calculations are needed.

3.4.5 Topological doping of correlated insulator and electronic liquid-crystal phases

The topological doping of correlated insulators[67] was argued to involve fundamental physics of transition-metal oxides. A materials which is an insulator entirely because of interaction effects is called a correlated insulator, e.g., trans-polyacetylene[68] and high-T_C copper oxides. Whereas doping of a normal band insulator results in a shift of the chemical potential into the conduction or valence band, doping of a correlated insulator produces fundamental changes in the electronic density of states (DOE) itself. The doping of a correlated insulator generally produces a density of topological defects in the insulating order. The charge stripe and relevant IC spin fluctuation observed recently was proposed to be a consequence of the topological doping of correlated insulators. The topological doping results in a state which is

inhomogeneous on intermediate scales of length and time with added charges localized in topological defects.

The topological doping also could lead to some new phases of matter, such as electronic liquid-crystal phase (ELC) of a doped Mott insulator predicated by a recent theory[69, 70]. A strong similarity between ELC phases and stripe phases was revealed. Such new phases of matter were indicated to be strongly associated with some unusual properties, such as high T_C superconductivity and 2D anisotropic metallic non-Fermi liquids. A schematic phase diagram of ELC phases is shown in Fig. 3.9. The quantum parameter depends in a complicated way on material parameters, as well as doped hole concentration. The schematic view of the local stripe order in the various phases is also indicated in Fig. 3.9. Heavy lines represent liquid-like stripes, along which the electrons can flow, whereas the filled circles represent pinned, density-wave order along stripes. The stripes are shown executing more or less harmonic oscillations in the smectic phase. Two dislocations, which play an essential role in the smectic-to-nematic phase transition, are shown in the view of the nematic phase.

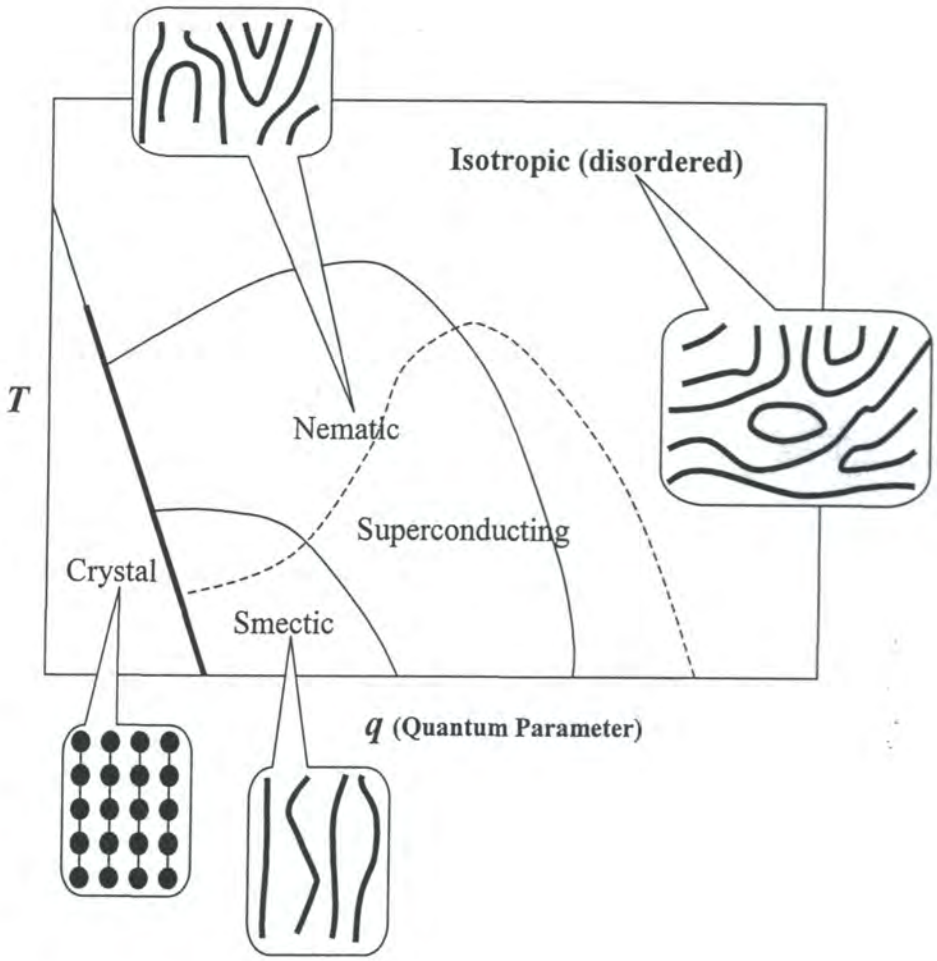

Fig. 3.9 Schematic phase diagram of the electronic liquid crystal phases of a doped Mott insulator, as discussed in the text. The quantum parameter, q, depends in a complicated way on the material parameters, as well as the doped hole concentration. (taken from Kivelson *et al.*[69])

3.4.6 Theories of the perovskite manganites

The double exchange (DE) and ferromagnetic Kondo lattice model (FKL) are the two main theories for describing the behaviour of the perovskite manganites[71]. It has been

known since 1950's that some hole-doped $LaMnO_3$ compounds become FM metals, and exhibit remarkable magnetoresistive properties. In 1951, Zener[72] proposed a theoretical explanation for this intriguing phenomenon via the DE mechanism. He assumed that the only way to transport transfer between Mn^{4+} and Mn^{3+} was via the simultaneous hopping of an e_g electron from Mn^{3+} to the connecting O^{2-} and from the O^{2-} to the Mn^{4+} e_g band; hence the term double exchange. Ferromagnetism is then induced via this hopping by the very large Hund's rule coupling between the Mn e_g and t_{2g} electrons. An explicit formulation of this mechanism was first presented by Anderson and Hasegawa[73], and treated in a mean-field type description by De Gennes[74]. In those studies, an effective one-band Hamiltonian[71] was proposed which in the limit of infinite Hund's rule coupling is represented by Equation 3.8,

$$H_{DE} = \sum_{ij} \frac{t_{ij}}{\sqrt{2}} \sqrt{1 + \frac{\boldsymbol{S}_i \boldsymbol{S}_j}{\boldsymbol{S}^2}} (c_i^{\dagger} c_j + H.c.) \tag{3.8}$$

Equation 3.8 describes the hopping of spinless fermions with a hopping amplitude dependent on the relative orientation of the total *d*-electron spin on neighbouring sites *i* and *j*. However, the DE model is unable to completely describe the entire phase diagram observed experimentally.

Kubo and Ohata derived a mean-field theory for perovskite manganites using the so-called ferromagnetic Kondo lattice (FKL) model[75, 76], in which the spin degrees of freedom are explicitly taken into account, as shown in Equation 3.9[71],

$$H_{FKL} = -t \sum_{i,j,\sigma} (c_{i\sigma}^{\dagger} c_{jk} + H.c.) + J_H \sum_{i,\sigma,\sigma'} (\boldsymbol{S}_i \cdot \sigma_{\sigma\sigma'}) c_{i\sigma}^{\dagger} c_{j,\sigma'} \tag{3.9}$$

Where spin –1/2 e_g electron $c_{i,\sigma}^{+}$ are hopping in a cubic lattice coupled to a local S = 3/2 spin, describing the three localized t_{2g} electrons. The FKL calculations showed that a FM to PM phase transition occurred at T_C, accompanied by a change in the

temperature dependence of the resistivity, and a diverging negative magnetoresistance at this transition. Using a modern version of mean field theory, the $d = \infty$ mean field theory[77] developed for the treatment of correlated electrons in the high-T_C superconductors, N. Furukawa reproduced the earlier results of the FKL model. In particular, a more recent computational analysis[78] of the FKL model has revealed a rich phase diagram in manganites, and also predicated the existence of the phase separation (PS).

The interest in these models was renewed recently in connection with the active study of the manganites with CMR. The most controversial point is whether the ingredients previously employed in the DE and FKL models are sufficient to adequately describe the physics of manganites. One school of thought, represented most notably by N. Furukawa, maintains that the FKL model is adequate, provided that proper electron-electron correlations are taken into account[77]. Many researchers, however, disagree with this statement, and believe that some important elements are missing in the DE and FKL models, such as a strong electron-phonon coupling, or JT distortion, double degenerate e_g orbitals and the tendency to phase separation (PS) etc. For example, the DE model was re-examined considering the realistic situation with double degenerate e_g orbitals by a theory from Brink and Khomskii[79]. It was found that the orbital degeneracy leads in general to the formation of anisotropic magnetic structures and that, in particular, depending on the doping concentration, the layered magnetic structures of the *A*-type and the chainlike structures of the *C*-type are stabilized. The phase diagram observed was consistent with the experimentally observed magnetic structures of some overdoped manganites, such as $Nd_{1-x}Sr_xMnO_3$ ($x > 0.5$).

3.4.7 The electron-lattice coupling and polarons in manganites

The strong interaction between charge, orbital, spin and lattice degree of freedom has been found to be important for both structural, magnetic and transport properties of perovskite manganites, and leads to some exotic behaviours, such as charge stripes,

lattice effect, and microscopic and mesoscopic phase separation. In 1996, A. J. Millis proposed that electron-lattice coupling may provide the missing ingredient for the DE model. In a dynamic mean field theory[80, 81], Millis *et al.* treated the DE coupling dynamically by using a "frozen-phonon approach" for the lattice. According to this model, in the PM phase above T_C charge carriers would be trapped by slowly fluctuating lattice distortions, known as *small polarons*. In the FM phase, these polarons would disappear, leaving the electrons free to move within the lattice. The most probable mechanism leading to the formation of polarons in manganites is the well-known JT effect[82, 83].

The existence of polarons in manganites has been subsequently confirmed through a number of experimental techniques. The most direct evidence for polaronic behaviour comes from the study of charge-ordered states[84], like $La_{1-x}Ca_xMnO_3$, since charge ordering can be thought of as resulting from a long-range-ordered polarons condensation. Polarons in the PM phases, which are assumed to play an important role in the charge transport, are much more elusive, because they possess neither the long-range ordering nor the static character of charge ordering. Nevertheless, the existence of small polarons above T_C also has been established by a variety of measurements[85-89]. In addition, the discovery of a strong oxygen isotope effect further points to the importance of dynamic lattice fluctuations[90-93].

3.4.8 Phase separation (PS) and stripes in manganites

Recent computational studies of FKL models for manganites have revealed a surprisingly complicated phase diagram, not anticipated in early calculations in this context in the 1950's and 60's. In particular, it was reported that transitions between the AF insulating state of the hole-undoped limit and the FM metallic state at a finite hole-density can occur through a mixed-phase process, or phase separation (PS). The calculations for both an one-orbital FKL model[78], and a two-orbital FKL model[94] including JT phonons gave quite similar PS scenario, though the two-orbital JT

model is a more realistic approach for manganites system, because of the importance of the double degenerate e_g orbitals and strong JT couplings. The Hamiltonian of a two-orbital JT model with JT phonons is given in Equation 3.10[94],

$$H_{total} = H_{FKL} + H_{JT} + H_{AF} \tag{3.10}$$

Where H_{FKL} is the standard FKL Hamiltonian. H_{JT} and H_{AF} is Hamiltonians of the contribution from JT phonons and AF exchange interactions. The orbital degree of freedom was suggested to be responsible for PS. When the long-range Coulomb interactions are included, a microscopiclly charge inhomogeneous state, such as charge stripes, should be stabilised. These phase separation tendencies also present at low electronic densities, influencing the properties of the FM region by increasing charge fluctuations. There has been considerable experimental evidence for the existence of PS in manganites[95, 96].

PS in manganites has clear similarities with previously discussed frustrated phase separation occurring in cuprates and nickelates. The tendency towards PS decreases across the transition-metal-row, from a strong tendency in Mn, through Ni, to a weak tendency in Cu. Depending on the competition between PS tendency and long-range Coulomb interactions, the electronic phase separation could appear with quite different length scales, from macroscopic electronic PS observed in superconducting $La_2CuO_{4+\delta}$[97] and some manganites, to mesoscopic electronic PS observed as charge stripes in a number of transition-metal oxides, and to microscopic electronic PS, such as orbital ordering in various manganites.

3.5 References

1 C. H. Chen, S. W. Cheong, and A. S. Cooper, Physical Review Letters **71**, 2461 (1993).

2 J. M. Tranquada, B. J. Sternlieb, J. D. Axe, *et al.*, Nature **375**, 561 (1995).

3 C. H. Chen, S. W. Cheong, and H. Y. Hwang, Journal of Applied Physics **81**, 4326 (1997).

4 C. H. Chen and S. W. Cheong, Physical Review Letters **76**, 4042 (1996).

5 J. M. Tranquada, J. D. Axe, N. Ichikawa, *et al.*, Physical Review B-Condensed Matter **54**, 7489 (1996).

6 J. M. Tranquada, J. D. Axe, N. Ichikawa, *et al.*, Physical Review Letters **78**, 338 (1997).

7 J. M. Tranquada, N. Ichikawa, and S. Uchida, cond-mat/9810212 (1998).

8 S. W. Cheong, G. Aeppli, T. E. Mason, *et al.*, Physical Review Letters **67**, 1791 (1991).

9 T. E. Mason, cond-mat/9812287 (1998).

10 H. A. Mook, P. C. Dai, S. M. Hayden, *et al.*, Nature **395**, 580 (1998).

11 P. C. Dai, H. A. Mook, and F. Dogan, Physical Review Letters **80**, 1738 (1998).

12 Y. S. Lee, R. J. Birgeneau, M. A. Kastner, *et al.*, cond-mat/9902157 (1999).

13 T. Suzuki, T. Goto, K. Chiba, *et al.*, Physical Review B-Condensed Matter **57**, R3229 (1998).

14 H. Kimura, K. Hirota, H. Mastsushita, *et al.*, Physical Review B (in press) **59** (1999).

15 K. Yamada, C. H. Lee, K. Kurahashi, *et al.*, Physical Review B-Condensed Matter **57**, 6165 (1998).

16 A. R. Moodenbaugh, Y. W. Xu, M. Suenaga, *et al.*, Physical Review B-Condensed Matter **38**, 4596 (1988).

17 J. D. Axe, A. H. Moudden, D. Hohlwein, *et al.*, Physical Review Letters **62**, 2751 (1989).

18 M. K. Crawford, R. L. Harlow, E. M. McCarron, *et al.*, Physical Review B-Condensed Matter **44**, 7749 (1991).

19 T. Goto, S. Kazama, K. Miyagawa, *et al.*, J. Phys. Soc. Jpn. **63**, 3494 (1994).

20 S. Wakimoto, R. J. Birgeneau, Y. Endoh, *et al.*, cond-mat/9902201 (1999).

21 M. VonZimmermann, A. Vigliante, T. Niemoller, *et al.*, Europhysics Letters **41**, 629 (1998).

22 C. N. R. Rao and A. K. Cheetham, Advanced Materials **9**, 1009 (1997).

23 C. N. R. Rao and A. K. Cheetham, Science **276**, 911 (1997).

24 A. P. Ramirez, Journal of Physics-Condensed Matter **9**, 8171 (1997).

25 Y. Tokura, Current Opinion in Solid State & Materials Science **3**, 175 (1998).

26 Y. Tokura, Physica B **237**, 1 (1997).

27 M. Imada, A. Fujimori, and Y. Tokura, Reviews of Modern Physics **70**, 1039 (1998).

28 H. Kuwahara and Y. Tokura, in *Colossal Magnetoresistance, Charge Ordering and Related Properties of Manganese Oxides*, edited by C. N. R. Rao and B. Raveau (World Scientific, Singapore, 1998), p. 217.

29 M. N. Baibich, J. M. Broto, A. Fert, *et al.*, Physical Review Letters **61**, 2472 (1988).

30 S. S. P. Parkin, Z. G. Li, and D. J. Smith, Applied Physics Letters **58**, 2710 (1991).

31 P. M. Levy, Science **156**, 972 (1992).

32 P. Schiffer, A. P. Ramirez, W. Bao, *et al.*, Physical Review Letters **75**, 3336 (1995).

33 H. Kuwahara, Y. Tomioka, A. Asamitsu, *et al.*, Science **270**, 961 (1995).

34 H. Y. Hwang, S. W. Cheong, P. G. Radaelli, *et al.*, Physical Review Letters **75**, 914 (1995).

35 Y. Tomioka, H. Kuwahara, A. Asamitsu, *et al.*, Applied Physics Letters **70**, 3609 (1997).

36 Y. Tomioka, A. Asamitsu, H. Kuwahara, *et al.*, Journal of the Physical Society of Japan **66**, 302 (1997).

37 H. Y. Hwang, T. T. M. Palstra, S. W. Cheong, *et al.*, Physical Review B-Condensed Matter **52**, 15046 (1995).

38 Y. Moritomo, H. Kuwahara, and Y. Tokura, Journal of the Physical Society of Japan **66**, 556 (1997).

39 Y. Moritomo, H. Kuwahara, Y. Tomioka, *et al.*, Physical Review B-Condensed Matter **55**, 7549 (1997).

40 Y. Moritomo, H. Kuwahara, and Y. Tokura, Physica B **237**, 26 (1997).

41 Y. Moritomo, A. Asamitsu, and Y. Tokura, Physical Review B-Condensed Matter **56**, 12190 (1997).

42 Y. Tokura, H. Kuwahara, Y. Moritomo, *et al.*, Physical Review Letters **76**, 3184 (1996).

43 H. Kawano, R. Kajimoto, H. Yoshizawa, *et al.*, Physical Review Letters **78**, 4253 (1997).

44 A. P. Ramirez, P. Schiffer, S. W. Cheong, *et al.*, Physical Review Letters **76**, 3188 (1996).

45 P. G. Radaelli, D. E. Cox, M. Marezio, *et al.*, Physical Review B-Condensed Matter **55**, 3015 (1997).

46 E. O. Wollan and W. C. Koehler, Physical Review **100**, 545 (1955).

47 Y. Tomioka, A. Asamitsu, H. Kuwahara, *et al.*, Physical Review B-Condensed Matter **53**, R1689 (1996).

48 Z. Jirak, S. Krupicka, and V. Nekvasil, Journal of Magnetism and Magnetic Materials **15-18**, 519 (1980).

49 Z. Jirak, S. Krupicka, and Z. Simsa, Journal of Magnetism and Magnetic materials **53**, 153 (1985).

50 V. Kiryukhin, D. Casa, J. P. Hill, *et al.*, Nature **386**, 813 (1997).

51 K. Miyano, T. Tanaka, Y. Tomioka, *et al.*, Physical Review Letters **78**, 4257 (1997).

52 A. Asamitsu, Y. Tomioka, H. Kuwahara, *et al.*, Nature **388**, 50 (1997).

53 J. Zaanen and O. Gunnarsson, Physical Review B-Condensed Matter **40**, 7391 (1989).

54 E. Fradkin, *Field Theories of Condensed Matter Systems* (Addison-Wesley Publishing Company, 1991).

55 G. Seibold, C. Castellani, D. C., *et al.*, Physical Review B **58**, 13506 (1998).

56 J. Zaanen and P. B. Littlewood, Physical Review B-Condensed Matter **50**, 7222 (1994).

57 D. Poilblanc and T. M. Rice, Physical Review B **39**, 9749 (1989).

58 H. Schulz, Physical Review Letters **64** (1990).

59 J. A. Verges, Physical Review B **43**, 6099 (1991).

60 M. Inui and P. Littlewood, Physical Review B **44**, 4415 (1991).

61 V. J. Emery and S. A. Kivelson, Physica C **209**, 597 (1993).

62 U. Low, V. J. Emery, K. Fabricius, *et al.*, Physical Review Letters **72**, 1918 (1994).

63 M. I. Salkola, V. J. Emery, and S. A. Kivelson, Physical Review Letters **77**, 155 (1996).

64 S. R. White and D. J. Scalapino, Physical Review Letters **80**, 1272 (1998).

65 S. R. White and D. J. Scalapino, Physical Review Letters **81**, 3227 (1998).

66 S. R. White and D. J. Scalapino, cond-mat/9812187 v2 (1998).

67 S. A. Kivelson and V. J. Emery, Synthetic Metals **80**, 151 (1996).

68 A. J. Heeger, S. Kivelson, J. R. Schrieffer, *et al.*, Review of Modern Physics **60**, 781 (1988).

69 S. A. Kivelson, E. Fradkin, and V. J. Emery, Nature **393**, 550 (1998).

70 S. A. Kivelson and V. J. Emery, cond-mat/9809082 (1998).

71 A. R. Bishop and H. Roder, Current Opinion in Solid State & Materials Science **2**, 244 (1997).

72 C. Zener, Physical Review **82**, 403 (1951).

73 P. W. Anderson and H. Hasegawa, Physical Review **100**, 675 (1955).

74 P.-G. De Gennes, Physical Review **118**, 141 (1960).

75 K. Kubo and N. Ohata, J. Phys. Soc. Jpn. **33**, 21 (1972).

76 K. Kubo and N. Ohata, J. Phys. Soc. Jpn. **33**, 929 (1972).

77 N. Furukawa, J. Phys Soc. Jpn. **64**, 2734 (1995).

78 S. Yunoki, J. Hu, A. L. Malvezzi, *et al.*, Physical Review Letters **80**, 845 (1998).

79 J. van den Brink and D. Khomskii, Physical Review Letters **82**, 1016 (1999).

80 A. J. Millis, B. I. Shraiman, and R. Mueller, Physical Review Letters **77**, 175 (1996).

81 A. J. Millis, Physical Review B-Condensed Matter **53**, 8434 (1996).

82 A. J. Millis, R. Mueller, and B. I. Shraiman, Physical Review B-Condensed Matter **54**, 5405 (1996).

83 A. J. Millis, R. Mueller, and B. I. Shraiman, Physical Review B-Condensed Matter **54**, 5389 (1996).

84 J. Q. Li, M. Uehara, C. Tsuruta, *et al.*, Physical Review Letters **82**, 2386 (1999).

85 S. J. L. Billinge, R. G. DiFrancesco, G. H. Kwei, *et al.*, Physical Review Letters **77**, 715 (1996).

86 S. Yoon, H. L. Liu, G. Schollerer, *et al.*, Physical Review B-Condensed Matter **58**, 2795 (1998).

87 T. T. M. Palstra, A. P. Ramirez, S. W. Cheong, *et al.*, Physical Review B-Condensed Matter **56**, 5104 (1997).

88 P. Calvani, P. Dore, S. Lupi, *et al.*, Journal of Superconductivity **10**, 293 (1997).

89 A. Lanzara, N. L. Saini, M. Brunelli, *et al.*, Physical Review Letters **81**, 878 (1998).

90 G. M. Zhao, K. Conder, H. Keller, *et al.*, Nature **381**, 676 (1996).

91 B. GarciaLanda, M. R. Ibarra, J. M. DeTeresa, *et al.*, Solid State Communications **105**, 567 (1998).

92 G. M. Zhao, K. Ghosh, and R. L. Greene, Journal of Physics-Condensed Matter **10**, L737 (1998).

93 G. M. Zhao, K. Ghosh, H. Keller, *et al.*, Physical Review B-Condensed Matter **59**, 81 (1999).

94 S. Yunoki, A. Moreo, and E. Dagotto, Physical Review Letters **81**, 5612 (1998).

95 E. Dagotto, S. Yunoki, and A. Moreo, cond-mat/9809380 (1998).

96 A. Moreo, S. Yunoki, and E. Dagotto, cond-mat/9901057 (1999).

97 J. D. Jorgensen, B. Dabrowski, S. Y. Pei, *et al.*, Physical Review B-Condensed Matter **38**, 11337 (1988).

Chapter 4

Experimental methods of x-ray scattering

4.1 Introduction

X-ray scattering is a powerful method to explore the microstructure of materials. However, most measurements for studies of charge stripes have been undertaken by neutron and electron diffraction. Since neutrons scatter from the small nuclear displacements induced by the modulated charge density, charge stripe peaks observed via neutron scattering are extremely weak. Electron diffraction is, of course, especially sensitive to the charge modulation, but it is only useful for surfaces or very thin films which may differ from their bulk counterparts, furthermore, the multiple scattering involved in electron diffraction makes it very difficult to quantitatively analyze structure. X-ray scattering seems to be a logical choice to study charge stripes in various transition-metal oxides.

In this chapter, the experimental methods of x-ray scattering are reviewed briefly. In section 4.2, the basics of the kinematical x-ray scattering theory is described. Some aspects related to experimental measurements are discussed in section 4.3, in which synchrotron radiation (SR) and related experimental techniques are also introduced.

4.2 Elements of x-ray scattering

4.2.1 Diffraction direction: Bragg's law and the Ewald reflecting sphere

The simplest way to describe x-ray diffraction is Bragg's law[1], as follows,

$$2d_{hkl}\sin\theta = n\lambda \tag{4.1}$$

where λ is x-ray wavelength, n is an integer, and the incident (θ_I) and diffracted angles (θ_f) are defined in Fig. 4.1 (a), with $\theta_i = \theta_f = \theta$. The d_{hkl} is the interplanar spacing of reflecting planes with the Miller indices h, k and l.

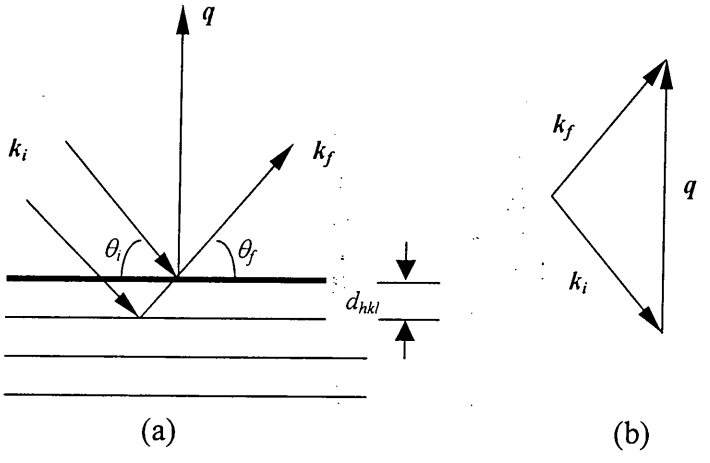

Fig. 4.1 The Bragg diffraction and the momentum transfer (q)

A very important concept, the momentum transfer (q), is defined as shown in Fig. 4.1 (b). $\boldsymbol{q}$ is the vector difference between the ingoing wavevector $\boldsymbol{k}_i$ and the outging wavevector $\boldsymbol{k}_f$. Since $|\boldsymbol{k}_i| = |\boldsymbol{k}_f| = |\boldsymbol{k}| = 2\pi/\lambda$ for elastic scattering, we can immediately derive the momentum transfer (q) with,

$$|\boldsymbol{q}| = |\boldsymbol{k}_f - \boldsymbol{k}_i| = 2|\boldsymbol{k}|\sin\theta = (4\pi/\lambda)\sin\theta = (2\pi n)/d_{hkl} \tag{4.2}$$

The momentum transfer is the fundamental experimental variable. It relates both to the experimental scattering angle, 2θ, through Equation 4.2, and to the theoretical scattering amplitude that will be discussed below.

Bragg's law and momentum transfer ($\boldsymbol{q}$) can also be graphically represented in reciprocal space. Fig. 4.2 shows the Ewald reflecting sphere construction for a set of planes at the correct Bragg angle. $\boldsymbol{k}_f$ is the wavevector of an incident x-ray which points to the origin of reciprocal space, O. A sphere of radius $|\ \boldsymbol{k}_i\ |\ (2\pi/\lambda)$ with a crystal at the center, A, can be drawn. The reciprocal lattice point *hkl* intersects the sphere at the exit point, B, of the diffracted beam. The vector **OB** is identical to momentum transfer ($\boldsymbol{q}$), or reciprocal lattice vector $\boldsymbol{d}^*_{hkl}$ of the reflecting planes. Thus, Bragg's law is equivalent to the statement that the reciprocal lattice point for the reflecting planes (*hkl*) should intersect the Ewald sphere. Conversely, if the reciprocal lattice point does not intersect the Ewald sphere then Bragg's law is not satisfied and no diffracted beams will occur.

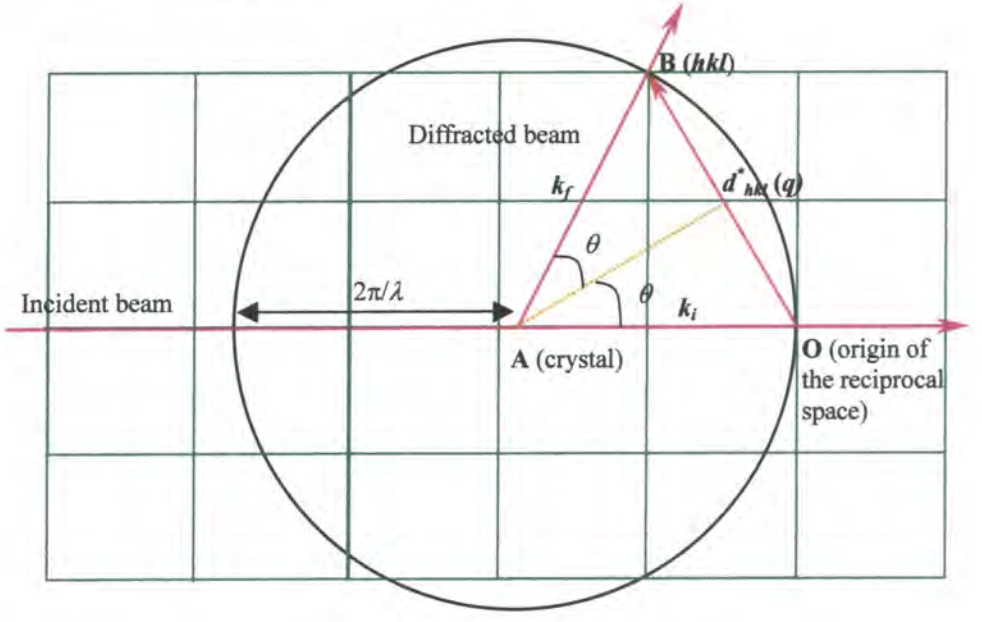

Fig. 4.2 The Ewald reflecting sphere construction of x-ray scattering in reciprocal space.

4.2.2 Diffraction intensity: kinematical theory of x-ray scattering

X-ray scattering by small, imperfect crystals has been comprehensively solved by kinematical theory[2-4]. In kinematical theory, the central assumption is that of single scattering, which means that every x-ray photon only interacts with the sample crystal once. The coherent scattering from different scattering gives rise to interference causing the observed diffraction. There also exists the dynamical theory for x-ray scattering[5], which gives the best description for highly perfect crystals. However, all crystals studied in this thesis are far from perfect, so only kinematical theory of x-ray scattering is introduced in the following part.

Consider a plane x-ray wave with wavevector $\boldsymbol{k}_i$ incident upon an atom located at $\boldsymbol{r}$, then the electric field amplitude of the scattered x-ray wave at a distance R from atom is,

$$E_1(\boldsymbol{q}, \boldsymbol{r}) = A_0 f(q)\, e^{i\boldsymbol{q}\cdot\boldsymbol{r}} \tag{4.3}$$

Where A_0 is the constant factor, $A_0 = E_0(e^2/mc^2)(1/R)$, $\boldsymbol{q}$ is the momentum transfer, and $f(q)$ is the atomic form factor, defined as the Fourier transform of the electron density of a single atom,

$$f(q) = \int_{atom} \rho(r) e^{i\boldsymbol{q}\cdot\boldsymbol{r}}\, dr \tag{4.4}$$

By neglecting the constant factors, the *scattering amplitude*, $A_1(\boldsymbol{q})$, can be defined as

$$A_1(\boldsymbol{q}) = f(q)\, e^{i\boldsymbol{q}\cdot\boldsymbol{r}} \tag{4.5}$$

X-rays scattered from different atoms within a crystal interfere with each other and thus diffraction occurs. For a crystal, which has a periodic structure, the first step in

calculating the diffraction pattern is to consider the diffraction from a single unit cell, the building block of the crystal structure. Under the single scattering assumption, the scattering amplitude of a crystal can be obtained by summing up the scattering amplitudes of all the atoms embedded in it, as shown below,

$$A_2 = \sum f(q) e^{iq \cdot r} = \sum_n \sum_j f_j(q) e^{iq \cdot (R_n + r_j)} = \sum_n F(q) e^{iq \cdot R_n} \qquad (4.6)$$

where $f_j(q)$ is the atomic form factor of the j-th atom in a unit cell. $\boldsymbol{R}_n$ is the position vector of the unit cell containing the atom and $\boldsymbol{r}_j$ is the position vector of the atom from the origin of the unit cell. The scattering amplitude of a unit cell, $F(\boldsymbol{q})$, is known as the *structure factor* and is defined as,

$$F(q) = \sum_j f_j(q) e^{iq \cdot r_j} \qquad (4.7)$$

Thus, the scattering amplitude of the crystal can be,

$$A_2 = F(q) \sum_n e^{iq \cdot R_n} \qquad (4.8)$$

Finally, consider the case of a crystal with the shape of a parallelepiped with edges N_1a_1, N_2a_2, N_3a_3 where a_1, a_2, a_3 are the lattice parameters. From Equation 4.6, the scattering amplitude of this crystal can be written as,

$$A_3 = \sum_n F(q) e^{iq \cdot R_n} = F(q) \sum_{n_1=0}^{N_1-1} \sum_{n_2=0}^{N_2-1} \sum_{n_3=0}^{N_3-1} e^{iq \cdot (n_1 a_1 + n_2 a_2 + n_3 a_3)} \qquad (4.9)$$

A function $S_N(x)$ can be defined as,

$$S_N(x) = \sum_{n=0}^{N-1} e^{ixn} = \frac{1 - e^{ixN}}{1 - e^{ix}} \tag{4.10}$$

This complex quantity represents a simplified version of the scattering amplitude for a one-dimensional crystal containing N atoms. The quantity of interest to experimenters is the square modulus of $S_N(x)$, representing the scattered intensity,

$$\left|S_N(x)\right|^2 = \frac{\sin^2(Nx/2)}{\sin^2(x/2)} \tag{4.11}$$

This is called the "N-slits interference function" because of its use in optics. Equation 4.9 then becomes,

$$A_3 = F(q)S_{N_1}(q \cdot a_1)S_{N_2}(q \cdot a_2)S_{N_3}(q \cdot a_3) \tag{4.12}$$

When N approaches infinity, the scattering amplitude is negligible everywhere except when $\boldsymbol{q} \cdot \boldsymbol{a}$ is equal to zero or 2π times any integer,

$$\boldsymbol{q} \cdot \boldsymbol{a}_1 = 2\pi h,\ \boldsymbol{q} \cdot \boldsymbol{a}_2 = 2\pi k \text{ and } \boldsymbol{q} \cdot \boldsymbol{a}_3 = 2\pi l \tag{4.13}$$

Here, h, k, l are called the *Miller indices*. Equation 4.13 is known as the *Laue conditions*, which is equivalent to the Bragg's law.

Now we can understand the diffraction pattern of a 3D crystal: the diffracted intensity is zero except at discrete points that lie on a lattice in the space of the momentum transfer vector, $\boldsymbol{q}$. The diffraction intensity at hkl points can be given as,

$$I_{hkl} = A_0^2 \left|F(q)\right|^2 \left|S_{N_1}(q \cdot a_1)\right|^2 \left|S_{N_2}(q \cdot a_2)\right|^2 \left|S_{N_3}(q \cdot a_3)\right|^2 \tag{4.14}$$

However, other non-structural factors, such as the temperature factor, Lorentz factor, absorption factor and polarization factor, need to be considered in order to calibrate intensities during measurements.

4.3 Experimental aspects of single crystal x-ray scattering

4.3.1 X-ray sources

Conventional x-ray generators produce x-rays through the interaction between electrons and anode materials. There are two types of generators widely employed by this method: a sealed x-ray tube and a rotating anode x-ray source[6]. Because x-rays are generated directly from electron transition, their energy is only related to the energy gap of the transition. Therefore, a conventional x-ray source only generates the discrete lines of the characteristic spectrum of the anode superimposed on the white radiation continuum. Another major disadvantage of conventional x-ray sources is the low efficiency. This disadvantage is caused in two ways. Firstly, much of the electron energy is converted to heat in the anode, instead of x-rays. Secondly, a conventional generator emits radiation isotropically with a large solid angle and, therefore, only a small fraction of the x-rays produced can be used.

Synchrotron radiation (SR) is an alternative source for x-ray scattering, which can produce much more intense and highly collimated x-ray photons[6-8]. SR originally was the "waste" radiation emitted by particle accelerators during experiments in high energy physics. All charged particles emit radiation when they are accelerated, such as the electrons and positrons in circular particle accelerators and storage rings. In the 1970's, scientists began to employ this radiation by add-on facilities at some accelerators. The capabilities of these "parasitic" facilities were limited, because their design and scheduled operation was compromised as their primary use was for high-energy physics research. They are called first generation SR sources. It was not until

the 1980's that specialized and dedicated SR sources, or second generation ones, were proposed and built throughout the world. The Synchrotron Radiation Source (SRS), at Daresbury Laboratory, Warrington (UK) and the National Synchrotron Light Source (NSLS), at Brookhaven National Laboratory (USA) are two typical second generation sources. In the third generation of high-energy synchrotron source, of which the European Synchrotron Radiation Facility (ESRF, 6 GeV) in Grenoble, France, the Advanced Photon Source (APS, 7 GeV) at Argonne National Laboratory, USA and the SPRing-8 (8 GeV) in Himeji, Japan are examples, the beam characteristics are significantly improved by the widespread use of insertion devices, such as *wigglers* and *undulators*. The insertion devices produce spatially alternating magnetic field which causes an undulation of the electron trajectory, and results in a shift in wavelength, and a large increase in usable intensity. There is a continuing improvement of SR sources, e.g., developments for the free-electron-laser (FEL) x-ray sources are already under way in some countries. Fig. 4.3 shows the improvement in the brilliance of the SR sources as a function of time.

The *brilliance* is an important characteristic parameter for a SR source, which is defined as the number of photons emitted per second, per unit source size, per unit space angle and for a bandwidth of 1/1000 of the photon energy, or brilliance = photons/s/mm^2/mrad^2/0.1%BW. In Fig. 4.3, It can be noticed that third generation synchrotron sources (~1995) are now emitting synchrotron x-ray beams that are a trillion (10^{12}) times more brilliant than those produced by x-ray tubes. The *emittance* is another important parameter, which describes the divergence of the synchrotron beam.

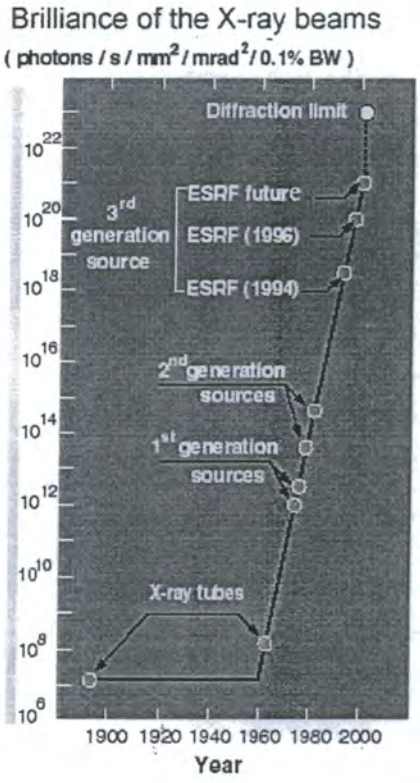

Fig. 4.3 Improvement in the brilliance of the SR sources (taken from *http://www.esrf.fr*)

Most SR sources consist of three parts: a linear accelerator (LINAC), a booster and a storage ring, as shown in Fig. 4.4. Electrons are generated and accelerated in the LINAC then passed to the booster where their energy is raised again. Finally, the electrons with a speed close to the velocity of light are injected into the storage ring. The storage ring is mainly a circular tube under ultra high vacuum. The bending magnets are used to provide a central force to bend the trajectory of electrons and make the trajectory a stable polygonal orbital in the storage ring. When electrons are deflected, x-ray will be emitted tangentially.

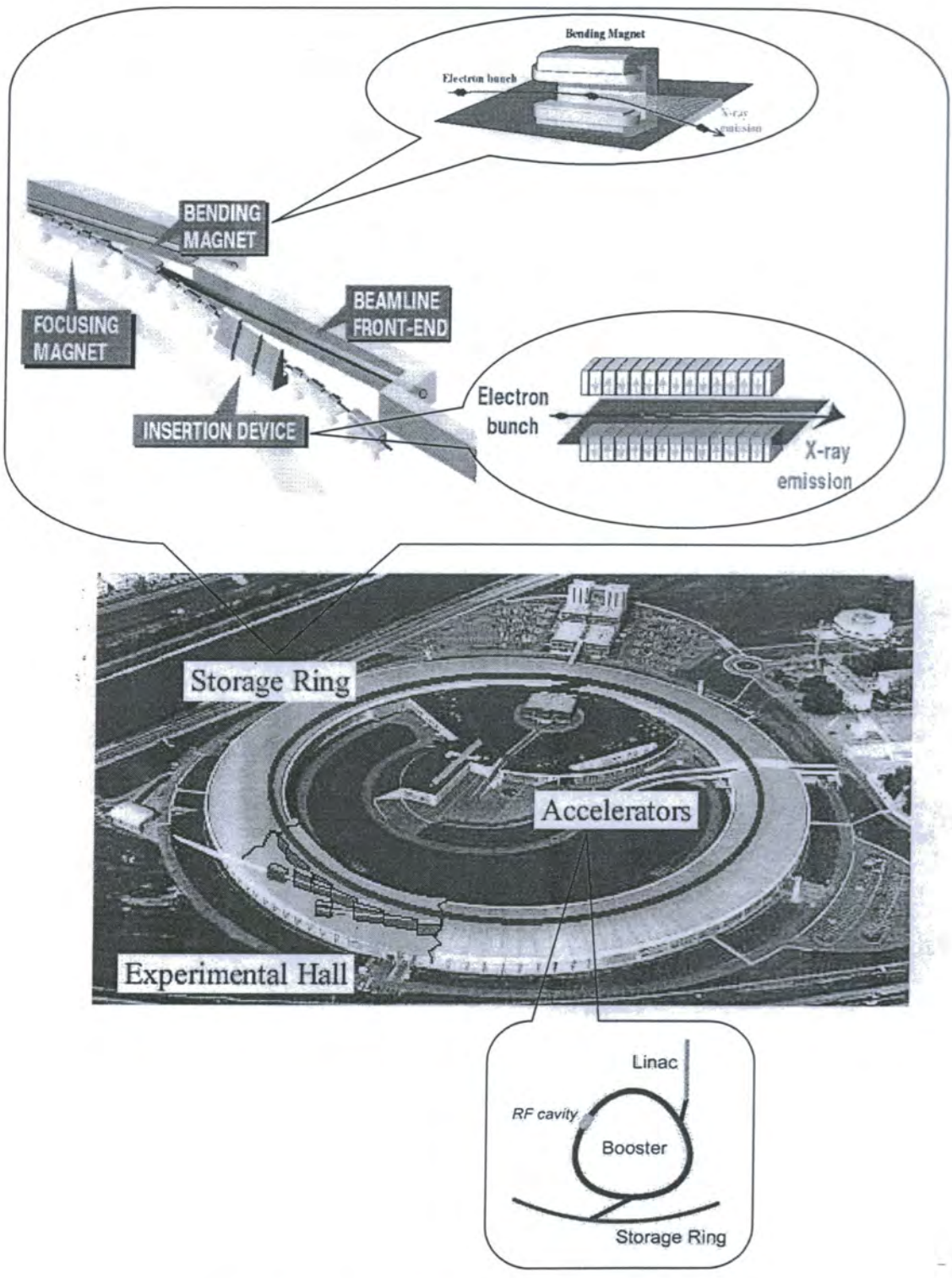

Fig.4.4 The layout of a typical synchrotron radiation facility.

Comparing to conventional sources, the advantages of synchrotron radiation can be summarised as,

- *High brilliance* (intense x-ray beam particularly for small samples)
- *Low divergence* (intrinsically collimated)
- *Tunable* (wide continuous spectrum)
- *Polarisation* (polarised)
- *Time structure* (pulsed)

These properties make synchrotron radiation extremely useful for studying the structural and electronic properties of condensed matter[9, 10]. Some recent applications are discussed as follows,

- *Weak reflections*: the extremely high brilliance of SR sources make it possible to study some very weak scattering, such as from Charge Density Wave (CDW) systems, Incommensurate (IC) modulated structures, Charge ordering (CO), and surface and interface reconstruction. Using SR sources, we have successfully demonstrated the novel features of two typical CDW materials, $B_{1-x}K_xBO_3$[11, 12] and 2*H*-$NbSe_2$[13].
- *Resonant scattering*: the tunable and polarised SR x-ray has been essential to decide the structures of the spin and orbital ordering[14-16] in some materials, in particular, it has been only possible technique to directly detect the formation of the orbital ordering in some transition-metal oxides.
- *Spectroscopy*: EXAFS and photon-emission spectroscopy can be very useful for detecting the local and electronic structures of materials.
- *Crystallography*: traditional single crystal diffraction can be done very fast, on very small samples, and on structures with very large unit cells, due to the very high brilliance.

- *Time-resolved structural studies*
- *Very high resolution measurements*
- *Extreme sample environments*: these include UHV growth, high pressure, variable magnetic fields etc.
- *High energy x-ray scattering*: it is particular useful for detecting very weak scattering by increasing the penetration depth of x-rays.

4.3.2 Diffractometers

Two-circle and four-circle diffractometers are the most common facilities for x-ray scattering[17, 18]. Fig. 4.5 shows the major elements of both diffractometers.

In Fig. 4.5 (a), the x-rays are incident on sample crystal which may be set at any angle to the incident beam, ω, by rotating about an axis through O, the centre of the diffractometer. The detector can also be rotated about O, and is set to any desired angle, 2θ, measuring the intensity of the x-rays scattered by the crystal. A standard four-circle diffractometer is shown in Fig. 4.5 (b). Two extra circles, χ and ϕ, are employed to change the orientation of the crystal. Different from the two-circle diffractometers, in which the diffraction vectors accessible are only those ones on the scattering plane defined by the incident and scattering wavevectors, the two extra circles in a four circle diffractometers can allow the user to select any lattice plane desired. There are diffractometers equipped with even more rotation adjustments for special purposes, e.g., in surface diffraction experiments, since the incident glancing angle and the scattering take-off angle must be fixed, a five or six circle diffractometer is necessary to achieve all the diffraction vectors under the extra geometrical limitations.

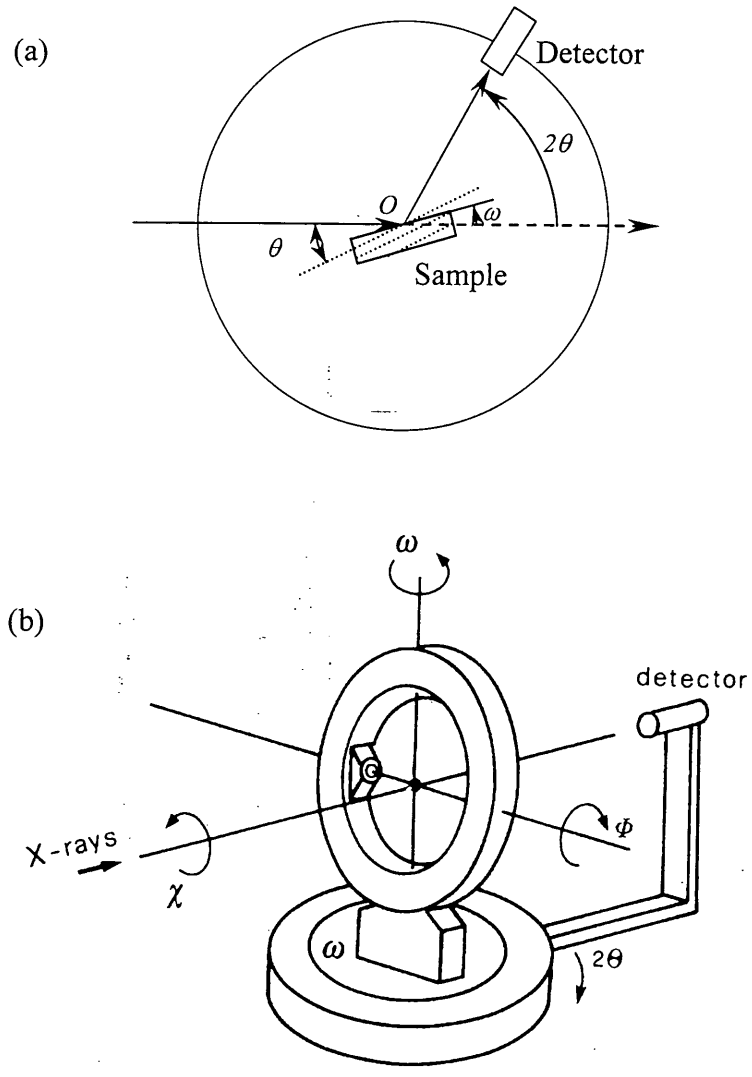

Fig. A schematic view of (a) a two-circle diffractometer, and (b) a four-circle diffractometer.

The Ewald reflecting sphere construction can be used to determine the diffraction condition. Fig 4.6 shows the Ewald reflecting sphere construction in a cubic reciprocal space in the case of a two circle diffractometer. $\boldsymbol{k}_i$ and $\boldsymbol{k}_f$ are wavevectors of incident and diffracted x-rays, $\boldsymbol{q}$ is the momentum transfer, ω and 2θ are incident and scattering angles. S is the Ewald reflecting sphere, according to Bragg's law, the diffraction will occur only when the diffracted reciprocal lattice point intersects S. The scattering angle, 2θ, is directly related to the magnitude of $\boldsymbol{q}$ and the glancing incident angle ω is related to the direction of $\boldsymbol{q}$. Because 2θ can not exceed 180°, it is obvious that the magnitude of $\boldsymbol{q}$ can not exceed a certain size. Consequently, it is impossible to have a $\boldsymbol{q}$ vector terminated outside the limit circle L, which is a circle centered at the origin of reciprocal space with radius $4\pi/\lambda$. Furthermore, for a large crystal with a flat surface, since the incident and diffracted waves are above the crystal, both 2θ and ω should always be positive. Under these limitations, there are two forbidden regions in reciprocal space within which $\boldsymbol{q}$ can never end inside, as shown as F in Fig. 4.6. So, only those lattice points within the limit circle but outside the forbidden regions are accessible by the diffractometer[18, 19].

In real measurements, the reciprocal space and multi-circle diffractometer are related by a $\boldsymbol{UB}$ matrix which must be calculated first. The $\boldsymbol{UB}$ matrix is the product of the $\boldsymbol{U}$ matrix (orientation matrix) and the $\boldsymbol{B}$ matrix (materials matrix). The $\boldsymbol{U}$ matrix can be calculated first by setting the lattice parameters for the sample crystal. To calculate the $\boldsymbol{U}$ matrix, the orientations of 2 Bragg reflections must be found. Once the $\boldsymbol{UB}$ matrix is defined, we can measure reflections in reciprocal space via moving individual circles of diffractometer in direct space.

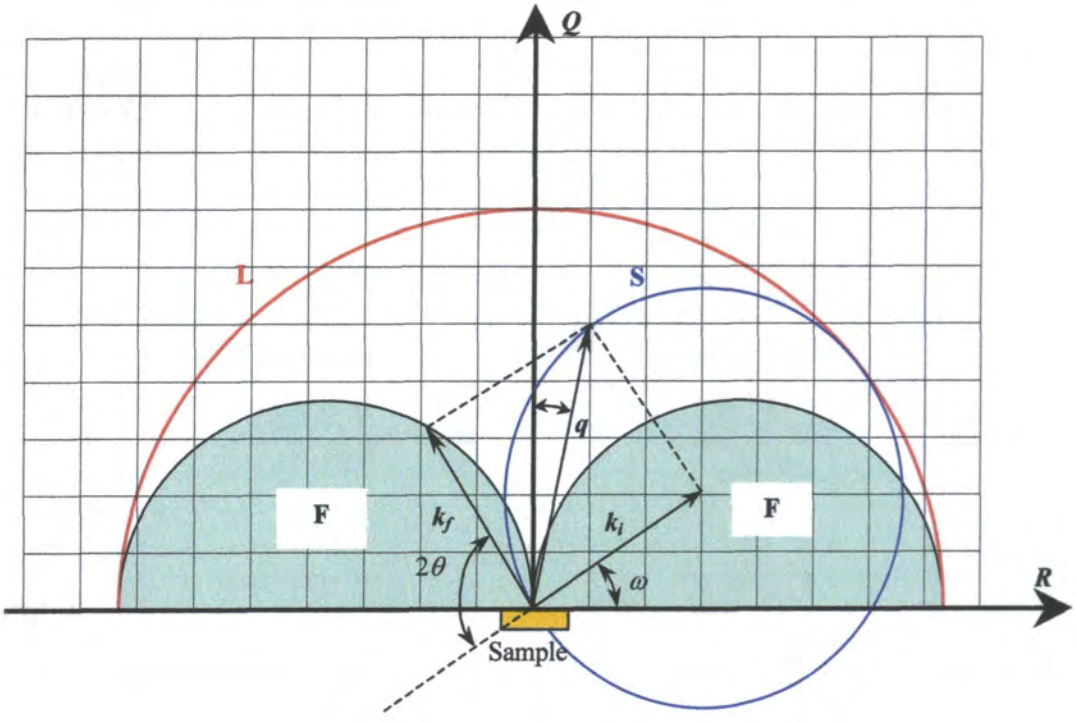

Fig. 4.6 The Ewald reflecting sphere construction and diffraction conditions

4.3.3 Double- and triple-axis scattering geometries and the resolution function

Both double-axis and triple-axis geometries have been widely used in various diffractometers for x-ray scattering. The double-axis diffractometer uses silts to limit the diffracted beam divergence before the diffracted beam reaches the detector, however, in a triple-axis diffractometer, the diffracted x-rays are first Bragg reflected off a crystal analyser and then monitored by the detectors. The silt selects the beam passing through it, regardless of the direction of the beam. On the other hand, the direction of the beam is selected by the crystal analyser, regardless of its position. So, it can be indicated that the slit is a position-sensitive optical element while the crystal analyser is a direction-sensitive element. Therefore, a triple-axis diffractometer is sensitive to the direction and the energy of the scattered x-ray beam and it probes directly wavevector space (reciprocal space). The double-axis diffractometer, however, is not only sensitive to the direction of the scattering beams but is also sensitive to their position. The resolution of a double-axis diffractometer depends on both reciprocal space and direct space effects. Thus it can be concluded that a triple-axis diffractometer often has a better resolution than a double-axis one. However, increasing the resolution also implies a commensurate reduction of signal intensity. For imperfect samples, high-resolution instruments are likely to reduce the signal of weak features thus making them almost impossible to detect. In this thesis, most of our measurements for charge stripes are undertaken in double-axis geometry, due to the nature of very weak scattering. Triple-axis geometry can also been employed if high-resolution measurements are needed.

Since it is very important to reach a proper balance between the resolution and the signal intensity as discussed above, understanding resolution degrading caused by the individual optical elements in the diffractometers becomes quite necessary. The resolution function of a triple-axis diffractometer has been well established by considering the intrinsic imperfection of individual optical elements[18, 19]. In a triple-axis diffractometer, the incident x-ray wavelength (λ), the monochromator crystal

(M), the sample crystal (S) and the analyser crystal (A) are not always perfect, therefore, they can individually cause streaks in wavevector space. After convoluting together these degrading effects, all the streaks will be centered at every Bragg reflection, the resolution function can be obtained as shown in Fig. 4.7 (a)[18, 19]. $\Delta\theta_m$ is the angular spread due to the monochromator crystal, $\Delta\theta_s$ is the angular spread due to the mosaic width of the sample crystal, $\Delta\theta_a$ is the angular spread due to the analyser crystal, and $\Delta\lambda$ is the wavelength spread of the incident beam. $\boldsymbol{Q}$ and $\boldsymbol{R}$ are longitudinal and transverse directions, respectively.

Fig. 4.7 (b) shows a experimental demonstration of the resolution function, in which the four streaks due to different imperfection effects are shown a 2-dimentional reciprocal space map of the Si (4, 0, 0) Bragg peak. The measurement was undertaken on BPEX, which is a two-circle triple-axis diffractometer using Ge crystals as both monochromator and analyser, in the University of Durham.

However in practice, it is usually better to measure the instrumental resolution function by using an appropriate Bragg reflection rather than calculate it explicitly. This has the advantage that the measured instrumental resolution function includes the effect of the mosaic spread of the specimen and also eliminates uncertainties in the collimator resolution and monochromator mosaic spreads. The instrumental resolution function is then assumed to be the same for small changes in wavevector. Experimental results are then analysed by assuming a parameterised functional form, such as Gaussian and Lorentz functions, convoluting it with the measured instrumental resolution function, and then adjusting the parameters to give a good fit to the experimental data.

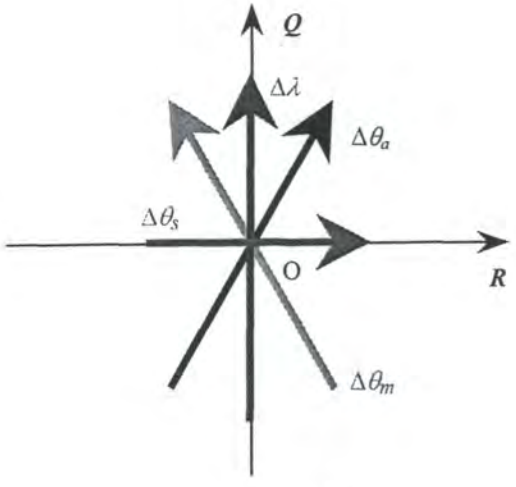

(a)

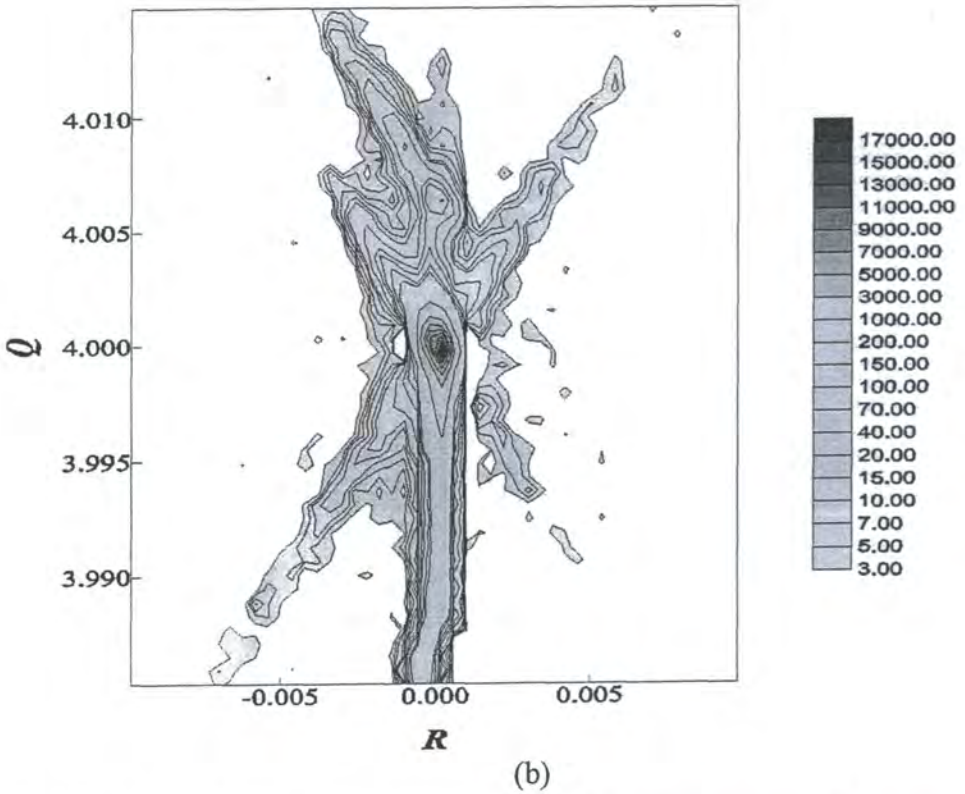

(b)

Fig. 4.7 (a) The resolution function of a triple-axis diffractometer; (b) A measurement of the resolution function of the BPEX diffractometer, the Si(4, 0, 0) Bragg reflection was measured.

4.4 References

1 C. C. Hammond, *The Basics of Crystallography and Diffraction* (Oxford University Press, Oxford, 1997).

2 B. D. Cullity, *Elements of X-ray Diffraction* (Addison-Wesley, Reading, Mass., 1978).

3 A. Gunier, *X-ray Diffraction in Crystals, Imperfect crystals, and Amorphous bodies* (Dover, New York, 1963).

4 B. E. Warren, *X-ray Diffraction* (Dover, New York, 1990).

5 W. Z. Zachariasen, *Theory of X-ray Diffraction in Crystals* (Dover, New York, 1967).

6 C. Giacovazzo, *Fundamentals of Crystallogrphy* (Oxford University Press, Oxford, 1992).

7 G. Margaritondo, *Introduction to Synchrotron Radiation* (OUP, New York, 1988).

8 P. Coppens, *Synchrotron Radiation Crystallography* (Academic Press, London, 1992).

9 J. Als-Nielsen and G. Materlik, Physics Today , 34 (1995).

10 J. Baruchel, *Neutron and Synchrotron Radiation for Condensed Matter Studies* (Springer, Berlin, New York, 1994).

11 C.-H. Du, Y. Su, P. D. Hatton, *et al.*, SRS Annual Report (1998).

12 C.-H. Du, Y. Su, P. D. Hatton, *et al.*, to be published (1999).

13 C.-H. Du, W. J. Lin, Y. Su, *et al.*, to be published (1999).

14 J. P. Hill, G. Helgesen, and D. Gibbs, Physical Review B-Condensed Matter **51**, 10336 (1995).

15 Y. Murakami, J. P. Hill, D. Gibbs, *et al.*, Physical Review Letters **81**, 582 (1998).

16 B. J. Sternlieb, J. P. Hill, U. C. Wildgruber, *et al.*, Physical Review Letters **76**, 2169 (1996).

17 D. K. Bowen and B. K. Tanner, *High Resolution X-ray Diffractometry and Topography* (Taylor & Francis, Bristol, PA, 1998).

18 W. J. Lin, PhD Thesis (University of Edinburgh, 1998).

19 T. W. Ryan, PhD Thesis (University of Edinburgh, 1986).

Chapter 5

Charge stripes and related structural phase transition in single crystal $Bi_{0.24}Ca_{0.76}MnO_3$

A single crystal of $(Bi_{0.24}Ca_{0.76})MnO_3$ has been extensively studied using both laboratory and synchrotron radiation x-ray scattering. Using x-ray techniques we can directly observe the formation of charge stripes associated with the low temperature structural phase transition. Weak satellite peaks with a modulation wavevector $\boldsymbol{q} \approx (0.24, 0.24\ 0)$ were observed below the transition temperature. These are associated with the charge ordering of Mn^{3+} and Mn^{4+} ions into charge (and spin) stripes within the perovskite structure. Measurements of the temperature dependence of the intensity and width of the charge ordering satellites over the temperature range 10 - 240K were also completed. These demonstrate the first order nature of the structural phase transition which accompanies the formation of charge and spin ordering. Measurements of the width of the charge order satellites demonstrate that the correlation length of the charge order is long-range at all temperatures, and in all directions, below the structural phase transition.

5.1 Introduction

Charge ordering into stripes in direct space has very recently attracted considerable attention due to its role in manganite colossal magnetoresistance (CMR)[1-5] and

cuprate superconductivity[6-8]. Charge ordering (CO) in the maganites is generally characterised by the direct space ordering of Mn^{3+} and Mn^{4+} ions. At room temperature these ions are randomly distributed within the sample MnO_2 planes. Upon cooling the ions become regularly sited. The charge ordered (CO) state is expected to become stable when the repulsive Coulomb interaction between the carriers (e_g electrons) dominates over the kinetic energy of carriers. The stability of the CO state is suggested to be very sensitive to the commensurability of the hole concentration with the lattice periodicity, and hence most enhanced at nominal hole concentrations of 1/2, 1/3 etc[9].

Charge ordering has also been observed in many doped Mott-Hubbard insulators such as $La_{2-x}Sr_xNiO_4$[10-13], $La_{2-x}Sr_xMnO_4$[14, 15] and $La_{1-x}Sr_xFeO_3$[16]. In many cases the charge ordering is accompanied by magnetic ordering, suggesting that the interplay between charge and spin ordering is important in explaining the anomalous physical properties. Recently, a charge-ordered state with charge stripes has been observed in single crystal $La_{1.6-x}Nd_{0.4}Sr_xCuO_4$($x$ = 1/8) by neutron diffraction[6, 7, 17]. This has lead to considerable discussion about the relationship between charge ordering and high-T_C superconductivity. Charge ordering into charge stripes is thus an important area of research applicable to a wide range of phenomenology in transition metal oxides.

To date studies of charge ordering in these systems have generally relied upon electron diffraction and neutron scattering. Electron scattering is very sensitive to weak superlattice reflections caused by charge ordering but only in the layers near the surface. Typically the electron diffraction studies have employed transmission geometry. This requires that the sample be sufficiently thin to allow the electrons to traverse through the sample. Typical sample thickness is therefore of the order of a thousand angstroms and samples are prepared by mechanical polishing followed by ion milling at cryogenic temperatures. Moreover, the technique has a relatively low wavevector resolution and the measured intensities are difficult to model due to multiple scattering effects. Neutron diffraction has been the major technique, suitable

for study of both the spin and charge stripes. An unfortunate condition for neutron scattering techniques is the need for relatively large sample sizes, which are difficult to grow in many manganites. In addition neutron diffraction is not directly sensitive to the charge ordering, but rather the charge order is detected indirectly through displacements of the nuclear positions because of the associated strain deforming the lattice. In this chapter the results of experiments on charge ordering in manganites using x-ray scattering are reported. These results are obtained without the use of small wavelength x-rays which, having a greater energy penetrate almost 1mm into the bulk employed by Vigliante[18] in nickelate, and von Zimmermann[19], in cuprate systems. Our experiments demonstrate that it is possible to directly detect the very weak scattering from charge ordering using long wavelength x-rays, corresponding to a penetration depth of about 10μm similar to that of the electron diffraction studies, and that x-ray scattering has an important role to play in the understanding of charge stripe physics.

The charge stripes in the Mn^{4+} rich regime ($x > 0.5$) were recently observed by electron diffraction in $La_{1-x}Ca_xMnO_3$[3-5, 20]. However, the growth of single crystals of charge-ordered compositions of $La_{1-x}Ca_xMnO_3$ is difficult, due to high Ca vapor pressure at high temperature in high Ca concentration region by floating-zone method[5]. Single crystals of the isostructural system $Bi_{1-x}Ca_xMnO_3$ ($x > 0.5$), however, can be successfully grown by the flux method. Polycrystalline $Bi_{1-x}Ca_xMnO_3$ was examined for both electrical and magnetic properties, displaying ferromagnetism and a large negative magnetoresistance for $x > 0.80$[21] suggestive of charge ordering. This was recently confirmed by a neutron scattering study on single crystals for $0.74 < x < 0.82$[22]. That study found that the charge ordering is accompanied by a structural phase transition and that the spin correlation changes from ferromagnetic to antiferromagnetic at the transition, with long range antiferromagnetic order developing below T_C, as shown in Fig. 5.1[5, 22], in which only measurement on $x = 0.82$ sample is displayed,

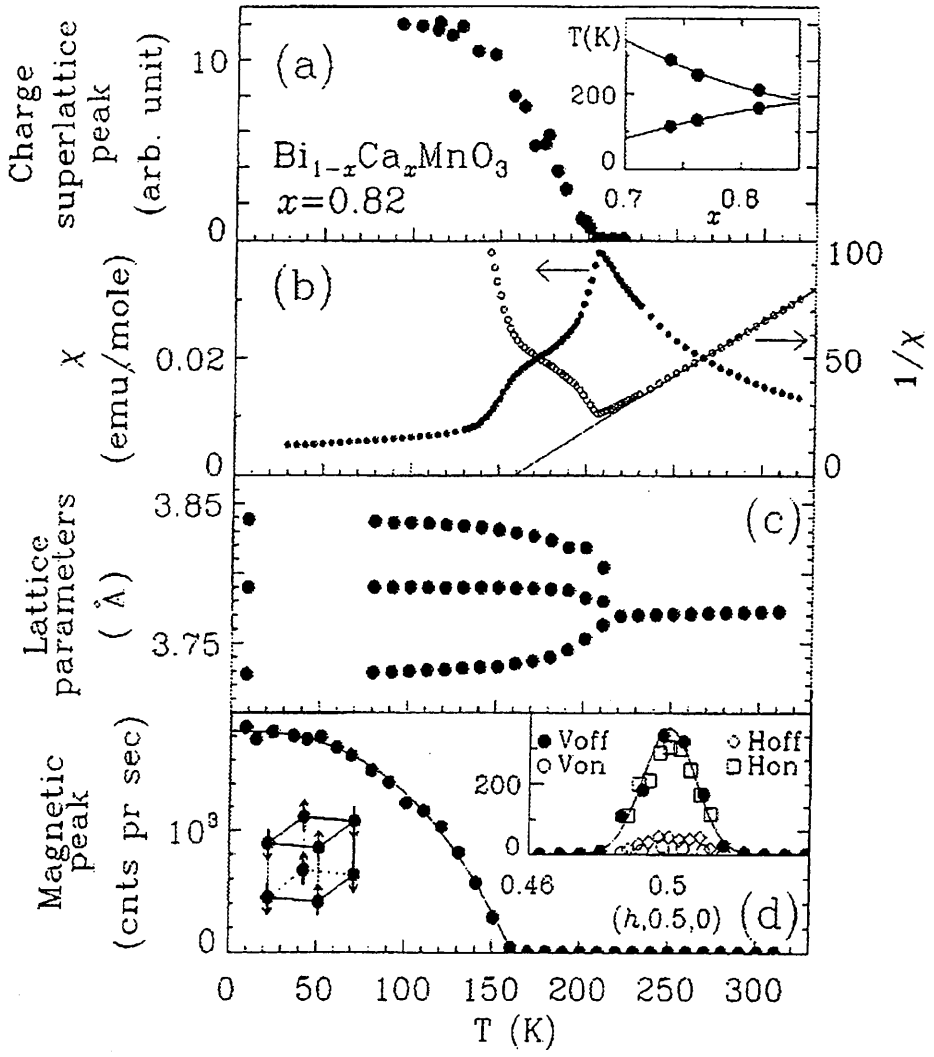

Fig. 5.1 $Bi_{0.18}Ca_{0.82}MnO_3$: temperature dependences of (a) Intensity of the charge superlattice peak, (b) magnetic susceptibility (χ), (c) pseudocubic lattice parameters, and (d) intensity of magnetic Bragg peak (1/2, 1/2, 0). Inset in (a): temperature-composition phase diagram for $Bi_{1-x}Ca_xMnO_3$, showing the charge ordering temperature T_{CO} and the Neel temperature T_N. (taken from Bao, Cheong, *et al.*[5, 22])

The charge ordering was also observed in polycrystalline $Bi_{0.2}Ca_{0.8}MnO_3$ by electron diffraction[23]. In addition to the near 1/4 incommensurate reflections, very long period features were observed corresponding to 1/32 and 1/36. However such studies cannot give quantitative intensities or provide detailed information on the long range correlation of the static direct space charge stripes. More recently, phase separation behavior, in which domains of ferromagnetic and antiferromagnetic order coexist, has been reported by optical studies in $Bi_{1-x}Ca_xMnO_3$ ($x > 0.5$)[24], which is consistent with a recent theoretical prediction[25, 26]. However, the mechanism of strong interplay between charge ordering , magnetism, lattice coupling and mesoscopic phase separation still remains unclear.

In this chapter the first detailed measurements of charge stripe formation in $Bi_{0.24}Ca_{0.76}MnO_3$ by high resolution x-ray scattering are described. Using both our in-house rotating anode x-ray source and a high resolution multi-axis diffractometer at the Synchrotron Radiation Source (SRS) at Daresbury Laboratory we have measured the temperature dependence of the charge stripe satellites which develop below the transition temperature (T_C = 241 K). Such results indicate the strong interplay between charge stripes and the related structural phase transition.

5.2 Experimental procedure

The in-house x-ray experiments were performed at the University of Durham. The crystal was mounted on the cold finger of a Displex closed-cycle cryostat, where the temperature was monitored with a Si diode to an accuracy of ± 0.1 K. The whole cryostat was mounted on a four-circle triple-axis diffractometer, which employed a high-brilliance rotating anode generator operated at 2.8 kW with a Cu anode. The Cu Kα (1.514 Å) x-ray beam was selected and collimated by two flat (0001) pyrolytic graphite crystals used as the monochromator and analyzer. Such an arrangement

gives a relatively poor resolution but very high intensity.

The experiment utilizing synchrotron radiation was performed at station 16.3 at the SRS, Daresbury Laboratory. The station is situated on a beamline employing a six Tesla superconducting wavelength-shifter (Wiggler 16) which provides photon beams with a wide range of energies, extending to over 50 keV. The instrument[27] is a large vertically-diffracting six circle diffractometer with a displex closed-cycle cryostat. A double-bounce Si (111) monochromator was used for the experiment, so that higher resolutions up to 10^{-4} Å^{-1} could be achieved. A wavelength of 1.000 Å was chosen to maximize the x-ray flux and a beamsize of 0.5 mm horizontally and vertically was used in all measurements. Double-axis geometry using fine slits, without the use of a crystal analyzer, was employed in our measurements. Vertical beam-defining and detector slits were both set at 0.5 mm, optimized to provide good wavevector resolution and low background levels without sacrificing significant diffraction intensity. A cooled solid state germanium detector was used with a narrow energy window to further decrease background scattering including fluorescence.

The single crystal of $Bi_{0.24}Ca_{0.76}MnO_3$ was grown by the flux method at Bell Laboratories. This sample had been previously characterised by a number of techniques[5, 22]. In particular the sample displays charge ordering at approximately 240K, but does not develop AFM spin ordering until ~120K. Most of the measurements were performed with the crystal oriented to have its [001] axis perpendicular to the scattering plane. The pseudocubic unit cell with a = 7.510 Å, b = 7.545 Å, c = 7.512 Å, $\alpha = \beta = \gamma = 90°$, was used for all the measurements.

5.3 Results and discussions

This sample displayed very clean singlet Bragg peaks with little background scatter. The instrumental resolution measured at the (400) Bragg peak was 0.025 Å^{-1} in both

longitudinal and transverse scans. Two dimensional contour scans in the (*hk*0) zone of reciprocal space were undertaken, after careful refinement of the orientation matrix. Cooling below 241 K resulted in additional satellite peaks at (~±0.24, ~±0.24,0) around the (400) Bragg peak, as shown in Fig. 5.2.

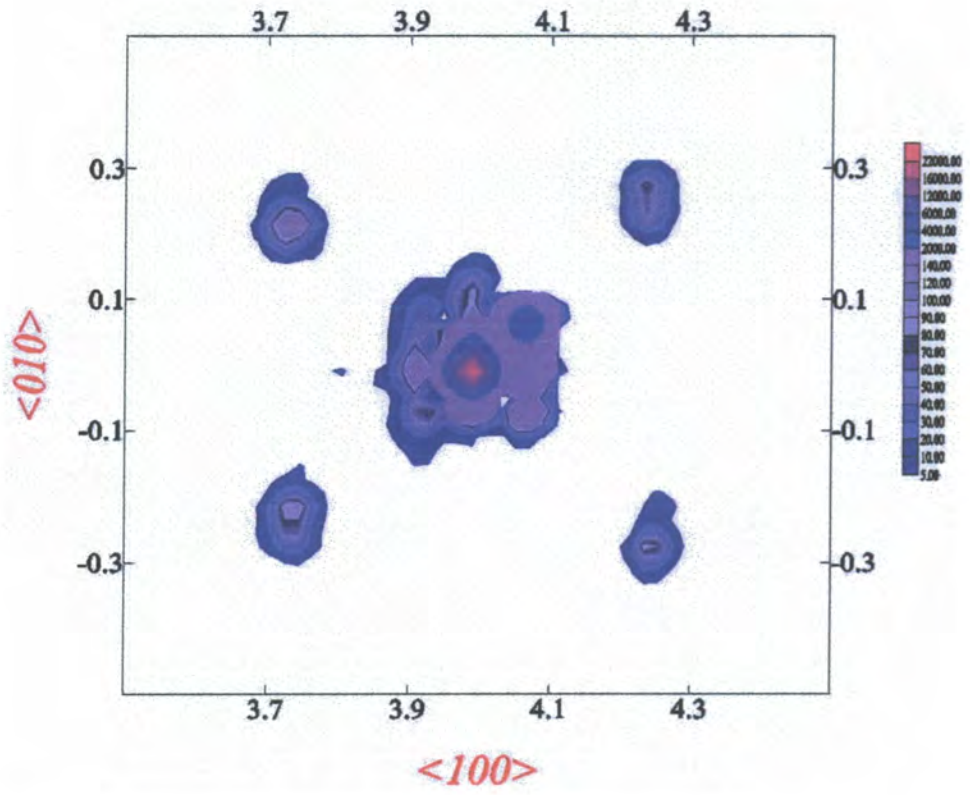

Fig. 5.2 Iso-intensity 2D-contour map around the (400) Bragg peak in reciprocal space of $(Bi_{0.24}Ca_{0.76})MnO_3$, T = 50 K, data obtained by using in-house rotating-anode source, 2 seconds per point counting time.

The pseudocubic notation, with $a \approx b \approx c \approx 2a_p$ (a_p is the basic perovskite unit cell), was used in our studies, and the satellite peaks resulting from charge ordering scattering were located along the diagonal, [110] direction in reciprocal space. However, this modulation wavevector is completely consistent with that observed by electron diffraction (δ, 0, 0)[4, 9] in the case of $La_{1-x}Ca_xMnO_3$ ($x > 0.5$), which used an orthorhombic notation with $a \approx b \approx \sqrt{2}a_p$, $c \approx 2a_p$. In our diffraction pattern four satellites are found, arranged symmetrically around each Bragg peak. This is similar to published electron diffraction pattern[4, 9] showing fourfold symmetry. This suggests charge ordering in a two dimensional sheet resulting in a checkerboard pattern. However direct space high resolution lattice imaging displays charge stripes running only in one direction. This apparent contradiction has been solved by complimentary dark-field images of charge charge-ordered domains in $La_{1-x}Ca_xMnO_3$[4, 9]. These demonstrate the presence of twin-related charge ordered domains of a few thousand angstroms in size. Discommensurations within such charge ordered domains have also been observed and it is likely that in our sample the diffraction pattern results from a sample that is microscopically twinned. More recently it has been suggested that such samples may also involve an inhomogenous spatial mixture of incommensurate charge-ordered and ferromagnetic charge-disordered microdomains which provide a dramatic case of microscopic-scale electron phase separation[28].

These satellite peaks have an intensity of ~60 counts/sec, after subtracting the background of 5 counts/sec, which is almost 10^{-3} less than that of the Bragg peaks. The very weak features very close to the (400) could be sample dynamical, monochromator and analyser streaks because of the triple-axis configuration. Satellite peaks with a similar modulation wavevector (±0.24, ±0.24,0) were also observed around other Bragg peaks such as the (800), (620) and (6-20). Upon warming the sample above 241 K, all the satellite peaks eventually disappeared, confirming the origin of these to be a superstructure of charge stripes induced by charge ordering of Mn^{3+} and Mn^{4+} in the MnO_2 sheet.

Longitudinal and transverse scans through some of the charge ordering peaks were fitted with a Gaussian function, as shown in Fig. 5.3,

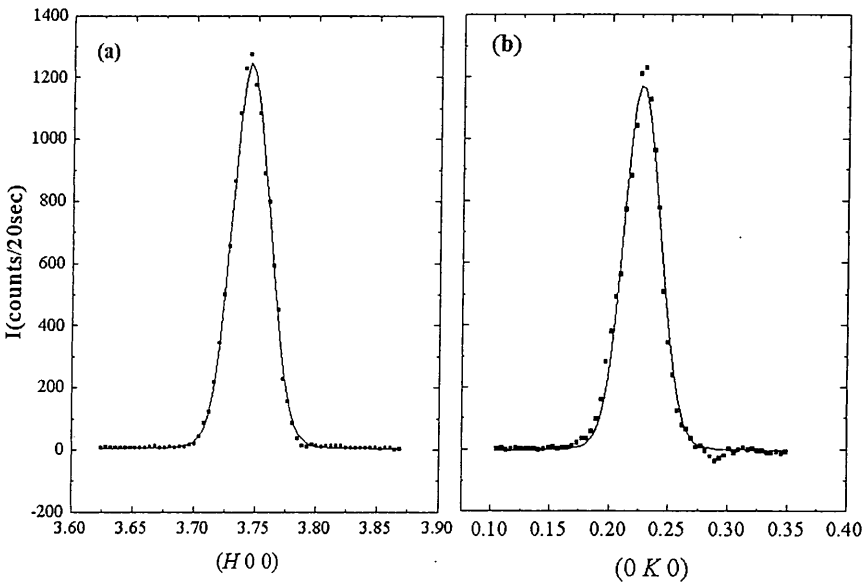

Fig. 5.3 (a) longitudinal and (b) transverse scans through one of charge stripe satellite peaks, (3.75, 0.25, 0) at T = 50 K, the solid squares are the experimental data. The data can be well fitted with a Gaussian function as shown by the solid line, which gives the FWHM as 0.03 $Å^{-1}$.

The full width at half maximum (FWHM) of the charge ordering peaks was found to be 0.03 $Å^{-1}$, which is almost identical to that of the Bragg peaks. However, all this indicates is that the widths of both the Bragg peaks and the charge ordered satellites are dominated by the intrinsic instrumental resolution which is governed by the mosaic width of the graphite crystals. The charge stripe satellites were found to be positioned at (±δ, ±δ ,0) around each Bragg peak where the wavevector,δ, was found to be 0.24. The modulation wavevector of the charge stripe order naturally depends upon the doped charge carrier concentration. For a hole carrier concentration of x, the ratio of Mn^{4+} ions to Mn^{3+} ions is $x/(1-x)$. For $x > 0.5$, the modulation wavevector of the charge-ordering, δ, is found to closely follow the stoichiometry $Bi_{1-x}Ca_xMnO_3$, according to the simple relationship $\delta = 1-x$, which is identical to that reported in $La_{1-x}Ca_xMnO_3$ ($x > 0.5$) by electron diffraction[4].

The temperature dependence of the integrated intensities of the charge stripe scattering was also measured and is shown in Fig. 5.4. The intensity of the CO satellites was observed to rapidly increase, upon cooling, at around 241 K (charge ordering temperature) which occurs simultaneously with the structural phase and magnetic transition as reported in refs[5, 22]. No temperature dependence of the FWHM of the charge ordering peaks was observed. Our measurements using our in-house diffractometer, fully demonstrate that it is possible to detect the relatively weak scattering from the formation of charge stripes in manganites using laboratory x-ray facilities

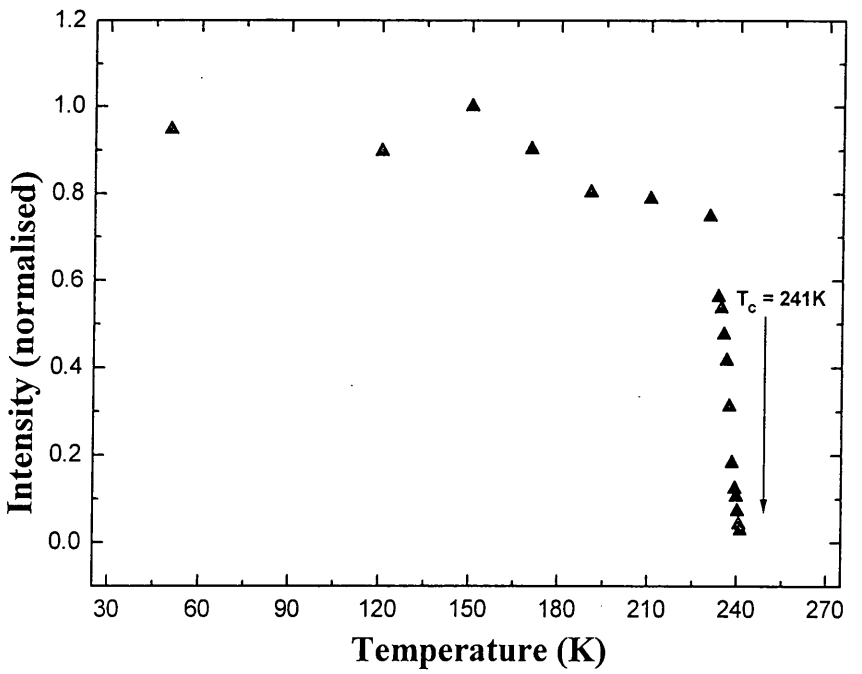

Fig. 5.4 The temperature dependence of the integrated intensity of the charge stripe peak (4.25, 0.25, 0), which implies a transition temperature, T_{CO}, of 241 K.

Previous x-ray powder diffraction studies by Bokov[29] and neutron scattering by Bao[22] both indicate that the lattice parameters display a sharp discontinuity around T_C = 241 K, which is associated with a structural phase transition from the high temperature orthorhombic phase to a low temperature monoclinic phase. The coincidence of charge ordering, structural, magnetic (FM to AFM) and metal-insulator transitions implies that there is strong correlation among electronic, spin and lattice degree of freedom. In fact, the lattice effect, or lattice distortion due to the different ionic radii of Mn^{3+} and Mn^{4+} and the tendency of Mn^{3+} to assume a Jahn-Teller distorted configuration have received a considerable attention[30-37]. A deviation from the basic perovskite structure caused by Jahn-Teller coupling, in which some Mn-O bond lengths decrease and others increase throughout the crystal, may be determined via conventional Bragg diffraction experiments, because the changes in bond length are long-rang ordered and coherent throughout crystal. Both x-ray and neutron powder diffraction can provide the information for the average crystallographic structure and internal structural parameters (bond distance and angle and Debye-Waller factors) and EXAFS and neutron pair distribution functions (PDF) can produce striking evidence for the local lattice distortion. However, these techniques probe the structure rather than the charge stripes. X-ray scattering can simultaneously provide information on both the structure and the charge stripes.

In order to obtain both a higher resolution and a higher count rate from the charge ordered satellites, measurements using synchrotron radiation on the same single crystal were carried out. Using the experimental configuration described above much higher resolution was obtained (0.0054 $Å^{-1}$) along both the longitudinal and transverse directions, and both the Bragg and charge stripe peaks displayed a Gaussian peak shape, as shown in Fig. 5.5.

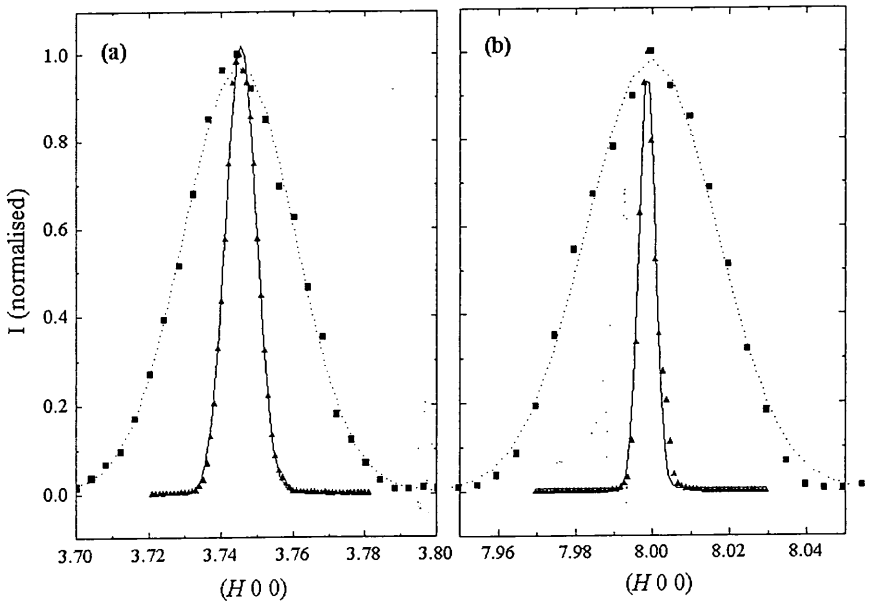

Fig. 5.5 (a) the charge ordering peaks along (H 0 0). (b) the (8 0 0) Bragg peak along (H 0 0). Both peaks are fitted by Gaussian function, the dotted lines are fits to the laboratory low-resolution data, solid lines are fits to the synchrotron data.

Even with the higher resolution obtainable with the use of synchrotron radiation it is clear that the quality of our sample used in this thesis is not high. The rocking curve gives a full width at half maximum mosaic width of approximately 0.2° (θ-scan). This is extremely large compared to semiconductor samples (Si, GaAs etc.) and demonstrates that extinction is not likely to affect the integrated Bragg intensities. This also explains the Gaussian peak shape and suggests that such features can be adequately treated using kinematical theory. The charge stripe peaks were found to have a intensity as high as 10^4 counts/sec. The (800) Bragg peak in the low temperature monoclinic phase was monitored upon warming up and through T_{CO}. At a temperature close to 240 K, the intensity abruptly dropped but did not completely disappear until 243 K. Simultaneously the (800) peak from the orthorhombic phase, separate in reciprocal space because of the different lattice parameters between the two phases, was observed as low as 234 K, but did not become dominant until above 241 K. The sample therefore displays mixed phase behaviour over an extended temperature range of almost 10K, again evidence for the first order character of the transition. The temperature dependence of the (800) Bragg peak in the high temperature orthorhombic phase upon cooling down is also shown in Fig. 5.6 (a) as well.

The hysteresis of the integrated intensity of the Bragg peaks is clearly demonstrated, and consistent with the first order nature of the structural phase transition. These results place the structural phase transition boundary at 240.5 ± 0.5 K, consistent with our earlier results. The temperature dependence of charge ordering in the vicinity of T_C, was also obtained via measurements of the satellite peaks along (100) and (010) in reciprocal space. Hysteresis of the integrated intensity of the charge stripe peaks was clearly observed as shown in Fig. 5.6 (b). This is typical for a first order structural phase transition.

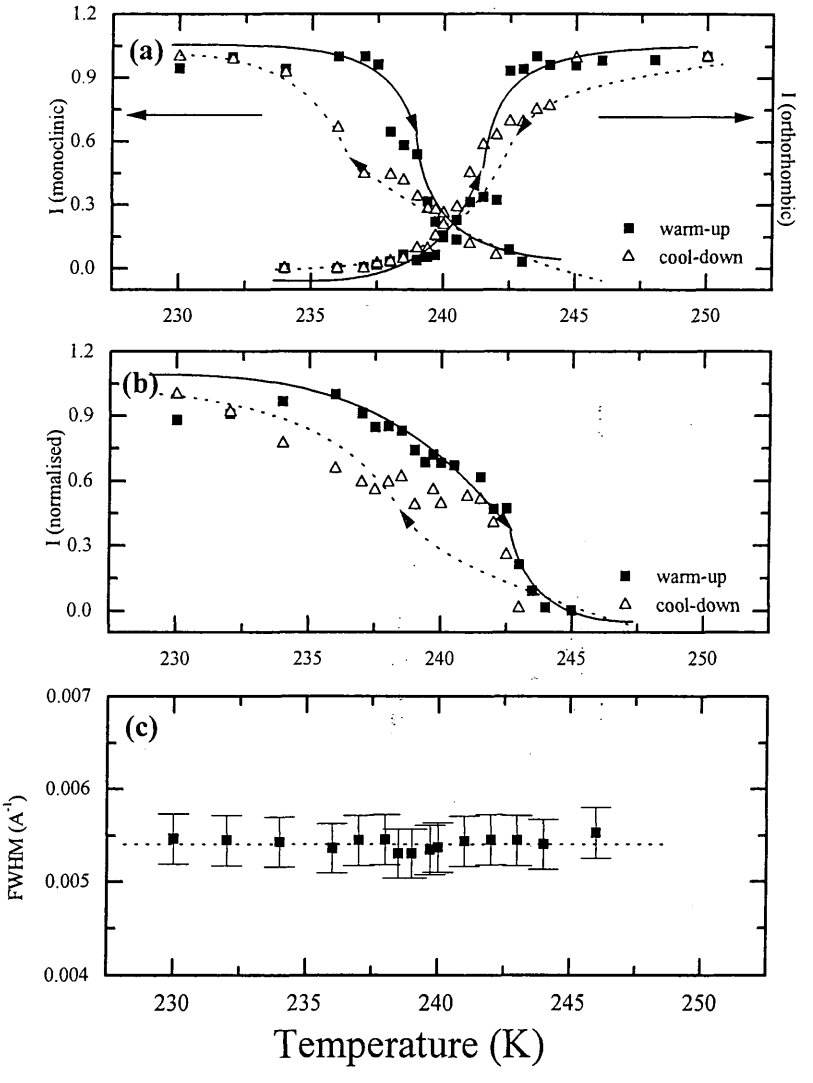

Fig. 5.6 (a) The integrated intensity of the (800) Bragg peak in both the high temperature orthorhombic, and low temperature monoclinic, phases. Figure 5 (b) The temperature dependence of the integrated intensity of the charge stripe peak (4.25, 0.25,0), all lines are guides for the eye. Figure 5 (c) The width of charge stripe peak, (4.25, 0.25, 0) as a function of temperature close to the structural phase transition. The dotted line is the instrumental resolution as measured on the (400) Bragg reflection

Our results are slightly at variance with the electron diffraction results reported on $Bi_{1-x}Ca_xMnO_3$ (x = 0.82)[5, 22] where the charge satellite intensity was observed to gradually increase upon cooling down from T_C (210 K), not becoming saturated until approximately 100 K. This may be a multiple scattering effect rendering the intensities difficult to interpret directly. No change of the width was observed upon either warming up and cooling down as shown in Fig 5.6 (c). This demonstrates that the charge stripes remain long range ordered through the transition. After careful comparison of Figs. 5.6 (a) and (b), some very interesting features were noticed. Upon warming up the sample from within the low temperature monoclinic phase, the intensity of the monoclinic Bragg peaks start to rapidly decrease at 238 K (see Fig.5.7 (a)). However the charge stripe peaks do not display such a rapid decrease in intensity such that at 241 K (above which the high temperature orthorhombic Bragg peaks are dominant) the intensity of the monoclinic Bragg peaks is very low but there remains still considerable relative intensity of the charge stripe peaks. Similarly, upon cooling down from the FM orthorhombic phase (Fig.5.7 (b)) the charge stripe intensity grows at a far more rapid pace than the development of the monoclinic Bragg reflections. These results suggest that at temperatures in the range 240 - 243 K there exist charge stripes, whilst the sample is still predominately orthorhombic in structure.

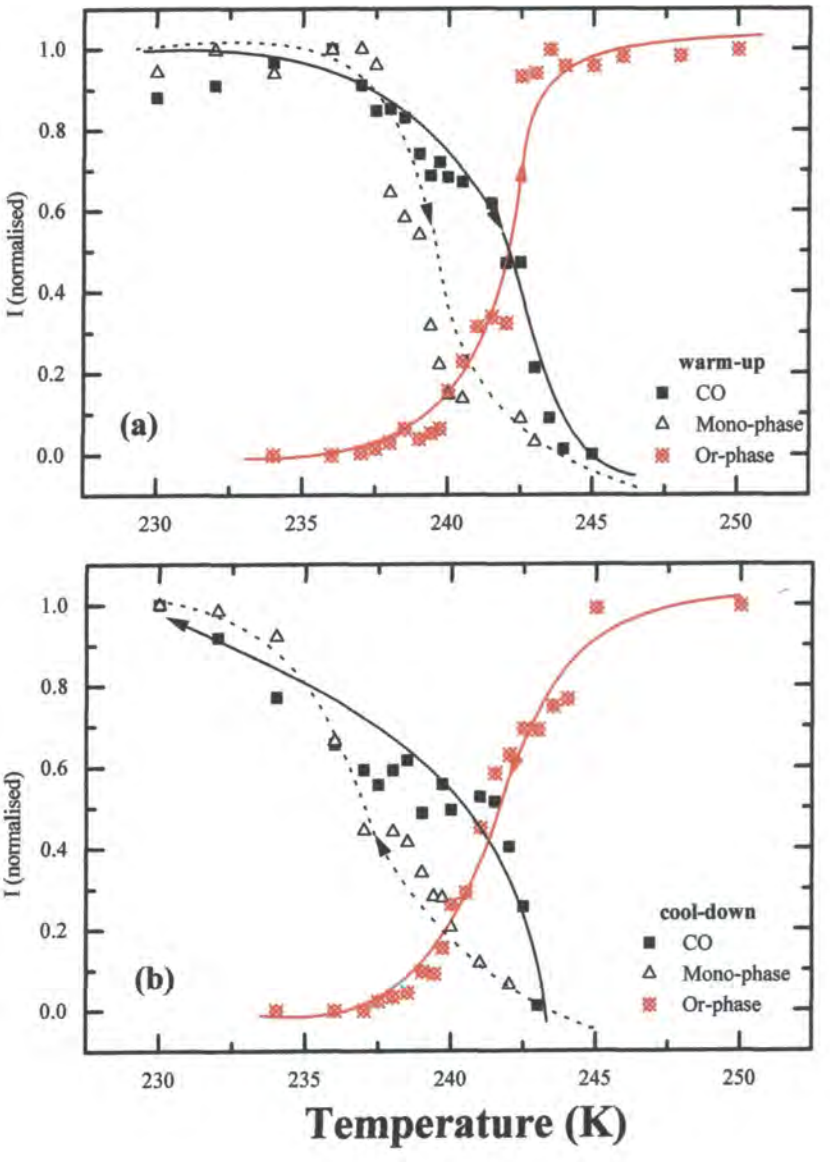

Fig. 5.7 (a) The integrated intensities of the charge ordering, monoclinic and orthorhombic phase peaks upon warming up around the T_C. (b) The integrated intensities of the charge ordering, monoclinic and orthorhombic phase peaks upon cooling down.

In some related materials such as $La_{1.4-x}Nd_{0.6}Sr_xCuO_4$[6] and $La_{2-x}Sr_xNiO_4$[11] the charge ordering and spin ordering occur at different temperatures. It is always found, however, that upon cooling the samples display charge ordering at a higher temperature, prior to spin ordering at yet lower temperatures. This suggests that charge ordering is the dominant driving force in the strong electron-phonon pairing found in such materials. In $Bi_{1-x}Ca_xMnO_3$, only charge ordering accompanies the first order structural phase transition. The formation of charge stripes within the orthorhombic structure will have dramatic effects on the energetics and hence phase stability. At 240.5 ± 0.5 K the energy of the high temperature orthorhombic and low temperature monoclinic phases are approximately equal. Further slow cooling results in a gradual transition from the orthorhombic to the monoclinic phase.

This also suggests that the formation of charge stripes upon cooling likely drives the structural phase transition into the low temperature form. It is also likely that the formation of charge stripes is more continuous a transition than the clearly discontinuous structural transition. The e_g electrons hopping between the Mn^{3+} and Mn^{4+} sites, results in a strong correlation between the charge, spin and lattice, which leads to charge ordering. The charge ordering, actually a strong coupling between the charge and lattice, eventually changes the bond length of the Mn-O, until the Jahn-Teller distortions throughout the crystal reach a new equilibrium, symbolized by the formation of the long range order and coherence of the charge and lattice. This result can be seen as a clear evidence for the strong interaction between the charge and lattice degrees of freedom.

To summarise, the observation of charge ordering into stripes by x-ray scattering techniques has been detailed described. Such experiments can be undertaken using either synchrotron or laboratory based x-ray sources, providing new information on both structural phase transitions and the formation of charge stripes in manganites. The strong relationship between the charge stripe ordering and the structural transition has also been discussed in detail.

5.4 References

1 A. P. Ramirez, Journal of Physics-Condensed Matter **9**, 8171 (1997).

2 A. P. Ramirez, S. W. Cheong, and P. Schiffer, Journal of Applied Physics **81**, 5337 (1997).

3 C. H. Chen and S. W. Cheong, Physical Review Letters **76**, 4042 (1996).

4 C. H. Chen, S. W. Cheong, and H. Y. Hwang, Journal of Applied Physics **81**, 4326 (1997).

5 S.-W. Cheong and C. H. Chen, in *Colossal Magnetoresistance, Charge Ordering and Related Properties of Manganese Oxides*, edited by C. N. R. Rao and B. Raveau (World Scientific, Singapore, 1998), p. 241.

6 J. M. Tranquada, B. J. Sternlieb, J. D. Axe, *et al.*, Nature **375**, 561 (1995).

7 J. M. Tranquada, J. D. Axe, N. Ichikawa, *et al.*, Physical Review Letters **78**, 338 (1997).

8 V. J. Emery and S. A. Kivelson, Physica C **263**, 44 (1996).

9 S. Mori, C. H. Chen, and S. W. Cheong, Nature **392**, 473 (1998).

10 A. P. Ramirez, P. L. Gammel, S. W. Cheong, *et al.*, Physical Review Letters **76**, 447 (1996).

11 S. H. Lee and S. W. Cheong, Physical Review Letters **79**, 2514 (1997).

12 J. M. Tranquada, D. J. Buttrey, and V. Sachan, Physical Review B-Condensed Matter **54**, 12318 (1996).

13 J. M. Tranquada, Journal of Physics and Chemistry of Solids **59**, 2150 (1998).

14 B. J. Sternlieb, J. P. Hill, U. C. Wildgruber, *et al.*, Physical Review Letters **76**, 2169 (1996).

15 W. Bao, C. H. Chen, S. A. Carter, *et al.*, Solid State Communications **98**, 55 (1996).

16 J. Q. Li, Y. Matsui, S. K. Park, *et al.*, Physical Review Letters **79**, 297 (1997).

17 J. M. Tranquada, N. Ichikawa, and S. Uchida, cond-mat/9810212 (1998).

18 A. Vigliante, M. vonZimmermann, J. R. Schneider, *et al.*, Physical Review B-Condensed Matter **56**, 8248 (1997).

19 M. VonZimmermann, A. Vigliante, T. Niemoller, *et al.*, Europhysics Letters **41**, 629 (1998).

20 A. P. Ramirez, P. Schiffer, S. W. Cheong, *et al.*, Physical Review Letters **76**, 3188 (1996).

21 H. Chiba, M. Kikuchi, K. Kusaba, *et al.*, Solid State Communications **99**, 499 (1997).

22 W. Bao, J. D. Axe, C. H. Chen, *et al.*, Physical Review Letters **78**, 543 (1997).

23 Y. Murakami, D. Shindo, H. Chiba, *et al.*, Physical Review B **55**, 15043 (1997).

24 H. L. Liu, S. L. Cooper, and S. W. Cheong, Physical Review Letters **81**, 4684 (1998).

25 S. Yunoki, J. Hu, A. L. Malvezzi, *et al.*, Physical Review Letters **80**, 845 (1998).

26 S. Yunoki, A. Moreo, and E. Dagotto, Physical Review Letters **81**, 5612 (1998).

27 S. P. Collins, R. J. Cernik, B. Fell, *et al.*, Journal of Synchrotron Radiation **5**, 1263 (1998).

28 S. Mori, C. H. Chen, and S. W. Cheong, Physical Review Letters **81**, 3972 (1998).

29 V. A. Bokov, N. A. Grigoryan, and M. F. Bryzhina, Phys. Stat. Sol. **20**, 745 (1967).

30 A. J. Millis, P. B. Littlewood, and B. I. Shraiman, Physical Review Letters **74**, 5144 (1995).

31 A. J. Millis, B. I. Shraiman, and R. Mueller, Physical Review Letters **77**, 175 (1996).

32 A. J. Millis, Physical Review B-Condensed Matter **53**, 8434 (1996).

33 A. J. Millis, Nature **392**, 147 (1998).

34 A. J. Millis, Philosophical Transactions of the Royal Society of London Series a- Mathematical Physical and Engineering Sciences **356**, 1473 (1998).

35 H. Roder, J. Zang, and A. R. Bishop, Physical Review Letters **76**, 1356 (1996).

36 P. G. Radaelli, D. E. Cox, M. Marezio, *et al.*, Physical Review B-Condensed Matter **55**, 3015 (1997).

37 P. G. Radaelli, G. Iannone, M. Marezio, *et al.*, Physical Review B-Condensed Matter **56**, 8265 (1997).

Chapter 6

Charge stripes in a single crystal of $Nd_{0.5}Sr_{0.5}MnO_3$

The striped charge ordering (CO) modulation in single crystal $Nd_{0.5}Sr_{0.5}MnO_3$ has, for the first time, been comprehensively studied using high resolution x-ray scattering. The charge ordering satellite reflections were observed to appear below T_{CO}, 160K, where a transition from a ferromagnetic (FM) to an antiferromagnetic (AFM) state occurs. The modulation wavevector was found to be $\boldsymbol{q}_{CO}$ = (1/2, 0, 0) or (0, 0, 1/2) in the (h0l) zone, which is consistent with the CE-type CO pattern suggested for $Nd_{0.5}Sr_{0.5}MnO_3$. The fact that the direction of the charge-ordered stripe is not fixed along either the a or c axes, results from perpendicular charge-ordered domains (CODs) and 90° twinning. From high-resolution data taken by triple-axis diffraction, we are able to clarify that (1/2, 0, 0) and (0, 0, 1/2)-type satellites have different correlation lengths, and thus are generated from different charge-ordered domains. This is first direct evidence for the existence of CODs obtained by x-ray or neutron diffraction, and is consistent with the results of electron microscopy. In additional, satellite peaks with modulation wavevectors $\boldsymbol{q}_1$ = (1/2, 0, 1/2) and $\boldsymbol{q}_2$ = (1/2, 1, 1/2) were observed upon cooling down below T_{CO}. The possible origins of these two types of satellites will be discussed.

6.1 Introduction

6.1.1 Intriguing properties

Doped perovskite manganites show a wide variety of magnetic-field induced phenomena, including colossal magnetoresistance (CMR)[1, 2]. Recent extensive studies have revealed that the observed features can be attributed not only to the double-exchange (DE) interaction[3-5], but also to other instabilities competitive with the DE interaction, such as antiferromagnetic (AF) superexchange, Jahn-Teller (JT) distortion[6-10], charge-orbital ordering interactions[11, 12], etc. Some of these competing interactions strongly couple with the lattice through the orbital degrees of freedom (or JT effect) of the e_g electrons on Mn^{3+} sites. The orbital degeneracy, and its lifting in a distorted lattice, lead to a variety of electronic/lattice instabilities and modifications[13].

Following the demonstration of charge stripes in $Bi_{0.24}Ca_{0.76}MnO_3$ by single crystal x-ray scattering, we turn to study charge stripes in CMR $Nd_{1/2}Sr_{1/2}MnO_3$ compound. $Nd_{1/2}Sr_{1/2}MnO_3$ is a typical charge-orbital-spin strongly coupled system, which shows some intriguing behaviour. The compound of $Nd_{1/2}Sr_{1/2}MnO_3$ undergoes a ferromagnetic (FM) transition from a paramagnetic (PM) state at T_C = 255 K due to the DE mechanism, namely a FM coupling between the local $3d$ electrons (t_{2g} state) spins via kinetic exchange of the itinerant $3d$ electrons (e_g state). The resistivity shows an appreciable decrease below T_C due to reduced magnetic scattering of the charge carriers in the spin-ordered FM phase and remains metallic down to ~ 160 K, as shown in Fig. 3.6[14]. However, a drastic change due to charge ordering (CO) occurs at T_{CO} ~ 160 K, as seen in Fig. 3.6. At the CO transition, the resistivity jumps by more than two orders of magnitude from a typically metallic value (5×10^{-4} Ωcm) and the FM magnetization disappears, indicating a simultaneous FM-to-AFM transition. In accord with these changes in electric and magnetic properties, the lattice parameters of the orthorhombically distorted perovskite shows distinct changes as shown in Fig. 3.6.

Another dramatic effect, an electronic (metal-to-insulator) first order phase transition, which can be caused by an external magnetic field, has also been reported, and has been the subject of intensive investigations[14-16]. As shown in Fig. 3.8, application of an external magnetic field to $Nd_{1/2}Sr_{1/2}MnO_3$ reduces the resistivity around the Curie temperature (T_C = 255 K) due to the reduced spin scattering by the magnetic filed induced alignment of the local spins t_{2g}. This is the conventional MR effect generally observed around T_C in the case of $La_{1-x}Sr_xMnO_3$[1]. A more remarkable field effect is that the CO phase transition is suppressed while the FM metallic region is extended to lower temperature. Under a magnetic field above 7T, the charge-ordered AFM insulating state is totally extinguished down to zero temperature, leading to a six orders of magnitude change in resistivity. Such magnetic-field-induced metal-insulator transitions (MIT) can be viewed as one of major origins of the CMR effect[16-18].

6.1.2 Structural aspects related to properties: charge-orbital-spin ordering

The structure of $Nd_{1/2}Sr_{1/2}MnO_3$ differs from that of most other perovskites, having *Imma* rather than the usual *Pnma* symmetry[19]. It is orthorhombic at room temperature with lattice parameters a=5.432 Å, b=7.633 Å, c=5.476 Å[20], as shown in Fig. 6.1.

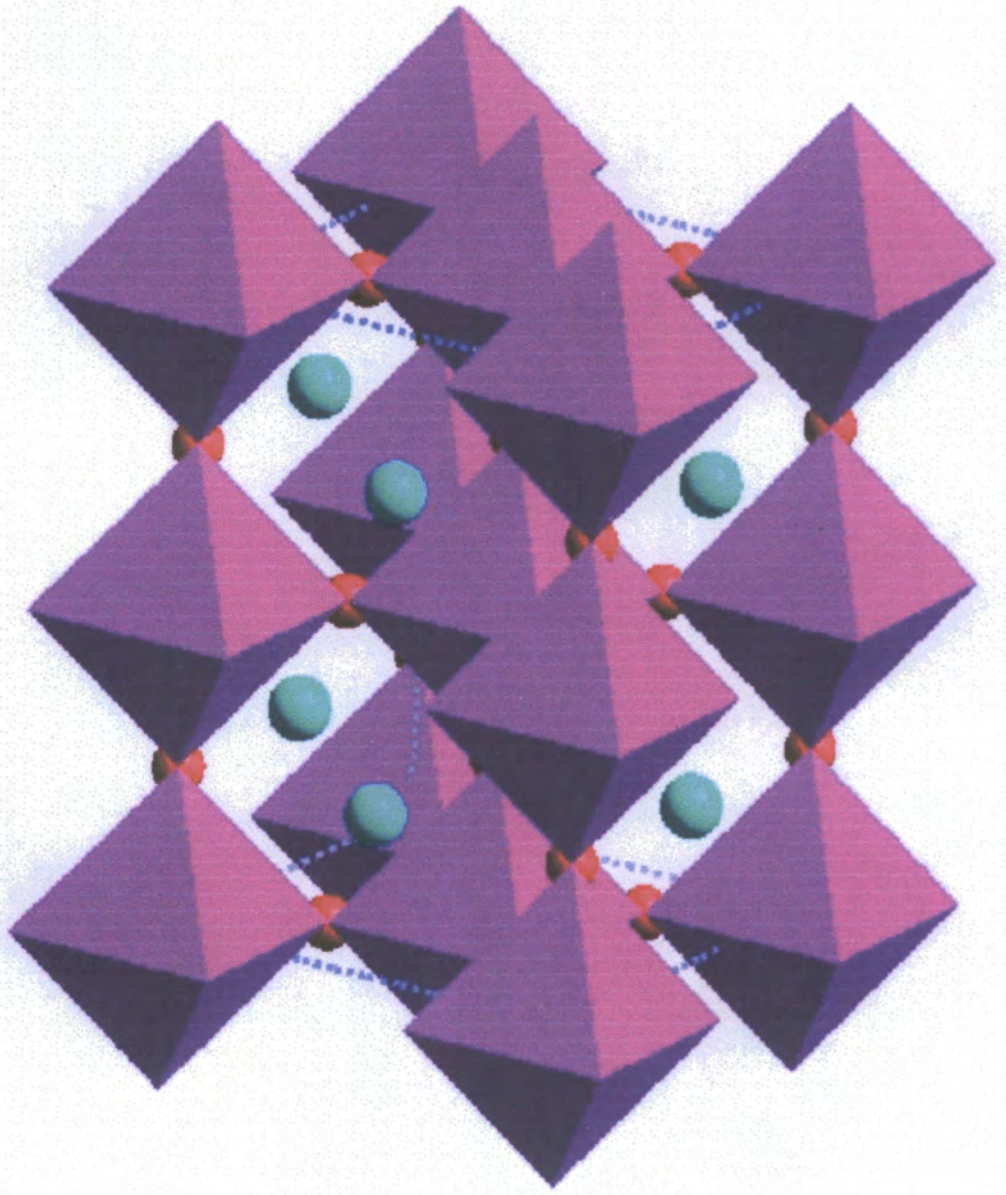

Fig. 6.1 The ideal crystal structure of $Nd_{1/2}Sr_{1/2}MnO_3$ at room temperature

The structure of $Nd_{1/2}Sr_{1/2}MnO_3$ can be obtained from the ideal cubic perovskite ($CaTiO_3$) structure by tilting of the octahedra about [101], rather than about both [101] and [010] as found in *Pnma*[21]. Consequently, the Mn-O-Mn angles in the *ac* plane are closer to 180° than that in the *b* direction. The bond angle anisotropy increases the spatial overlap of Mn e_g and O σ_{2p} orbitals, and hence the one electron bandwidth (W) in the *ac* plane.

These intriguing electrical and magnetic behaviour discussed above has been suggested as strongly linked to the formation and destruction of a possible CE-type AFM structure with charge ordering of $Nd_{1/2}Sr_{1/2}MnO_3$ at low temperatures (below T_{CO}), in which the nominally Mn^{3+} and Mn^{4+} species are assumed to form a checkerboard-like ordering on the *ac* plane, as illustrated in Fig. 2.11. In the original CE-type model proposed by Wollan and Goodenough[22-24], e_g electrons were assumed to occupy either $(3x^2-r^2)$- or $(3z^2-r^2)$-type orbitals in the *ac* plane so that $(3x^2-r^2)$- and $(3z^2-r^2)$-type orbital ordering can occur, as shown in Fig. 2.10(b) and Fig. 2.11. The CE-type AFM structure in manganites with n_h = 1/2 also implies a $2a\times b\times 2c$ (or $2\sqrt{2}a_p\times 2a_p\times 2\sqrt{2}a_p$, where a_p is the unit cell of the basic perovskite) magnetic supercell.

A number of recent experiments[20, 25] have provided evidence for the existence of charge-orbital-spin ordering in $Nd_{1/2}Sr_{1/2}MnO_3$. Using powder neutron diffractions, Kawano[25] and Woodward[20] observed two sets of magnetic modulations due to slightly different magnetic moments for Mn^{3+} and Mn^{4+}, respectively, below T_{CO} = 160 K. The magnetic modulation wavevectors of Mn^{3+} and Mn^{4+} superlattices can be indexed as followed,

$$q_{Mn^{4+}} = (1/2, l, 1/2) \qquad (6.1)$$

which represents a magnetic supercell doubling unit cell along both *a*- and *c*-axes, and

$$q_{Mn^{3+}} = (0, l, 1/2) \qquad (6.2)$$

which indicates another magnetic supercell doubling unit cell along *c*-axis. This result is consistent with the proposed CE-type AFM ordering structure, as shown in Fig. 6.2.

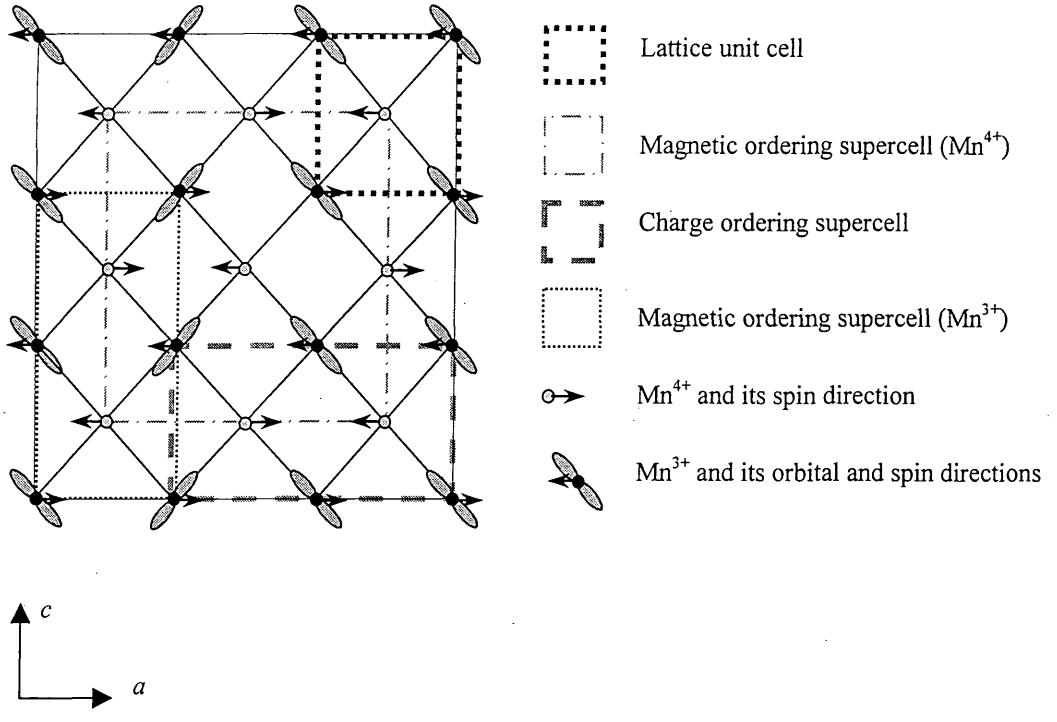

Fig. 6.2 A schematic view of charge, orbital and spin ordering in the *ac* plane in $Nd_{1/2}Sr_{1/2}MnO_3$

Unlike magnetic ordering, the behaviour of which has been well established, the charge ordering and resulting charge stripes in the CE-type structure are much more difficult to detect by neutron diffraction. Superlattice reflections, corresponding to a doubling of the unit cell along the *c*-axis, were observed and given as evidence for charge ordering[26]. However, magnetic ordering with the same modulation wavevector was reported as well. These observations are obviously in conflict. X-ray diffraction is far more sensitive in detecting small changes in charge density. In recent experiments uisng powder x-ray diffraction[20, 27], superlattice reflections indexed as (1/2, 2, 3) and (3/2, 2, 3) were observed, which indicated a doubling of the unit cell along the *a*-axis. However, neither measurements provided detailed information for the temperature dependence and correlation length of charge ordering reflections. Since high quality single crystals of $Nd_{1/2}Sr_{1/2}MnO_3$ grown using the floating zone method have recently become available, it is possible to undertake detailed measurements to clarify these aspects related to the charge ordering through single crystal x-ray diffraction.

Our measurements on $Nd_{1/2}Sr_{1/2}MnO_3$ have also been motivated by some recent reports. It was recently discovered that $Nd_{1/2}Sr_{1/2}MnO_3$ exhibits a *parasitic* A-type AFM state in the CE-type charge-ordered state[28]. An A-type magnetic Bragg peak, characterized by the modulation wavevector of (0, 1, 0), was observed to appear below $T_N^A \sim 200$ K. This transition was found to be second-order in character. The $(x^2 - z^2)$-type orbital ordering was suggested as being responsible for the formation of the A-type AFM structure[25, 28, 29]. The change of the magnetic structure from a CE-type to an A-type can be interpreted as an effect of widening of the one-electron bandwidth (W). The behaviour of the resistivity of the A-type manganites is also distinctly different from those with the CE-type structure. Metallic conductivity has been reported in A-type $Pr_{1/2}Sr_{1/2}MnO_3$ and $Nd_{0.45}Sr_{0.55}MnO_3$ compounds[25, 28, 29]. Coexistence of these two types of ordering has also been reported in the half-doped bilayer manganite $La_1Sr_2Mn_2O_7$[30]. The coexistence and competition between the A-type structure with $(x^2 - z^2)$-type orbital ordering and the CE-type structure with $(3x^2-r^2)$- and $(3z^2-r^2)$-type orbital ordering has been suggested to be essential to understand the related transport

properties. For examples, in Fig. 6.3[30], the resistivities of $Pr_{1/2}Ca_{1/2}MnO_3$ and $La_{1/2}Sr_{3/2}MnO_4$ are insulating over the whole temperature range, and they exhibit a sharp increase below T_{CO} due to charge ordering. By contrast, the resistivity of $Pr_{1/2}Sr_{1/2}MnO_3$ is considerably smaller, this is because a relatively wide W in $Pr_{1/2}Sr_{1/2}MnO_3$ suppresses the CE-type charge ordering, and leads to the A-type AFM structure with a very small resistivity below $T_N \sim 140$ K. Unlike the pure CE-type charge-ordered systems, $Nd_{1/2}Sr_{1/2}MnO_3$ and $La_1Sr_2Mn_2O_7$ both show rather small resistivities, indicating the competition between the two types of ordering.

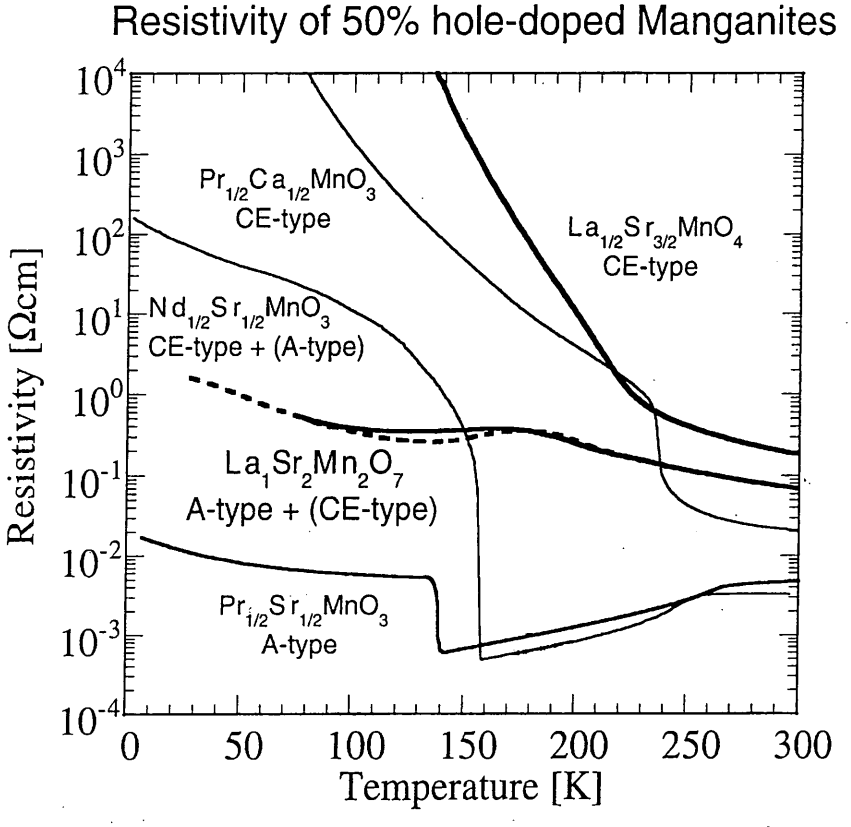

Fig. 6.3 Resistivities of 50% hole-doped manganite compounds: $Pr_{1/2}Ca_{1/2}MnO_3$, $Nd_{1/2}Sr_{1/2}MnO_3$, $Pr_{1/2}Sr_{1/2}MnO_3$, $La_{1/2}Sr_{3/2}MnO_4$ and $La_1Sr_2Mn_2O_7$(the *ab*-plane resitivity) (taken from Kubota *et al.*[30])

6.2 Experimental details

The experiment utilising synchrotron radiation was performed on station 16.3 at the SRS, Daresbury Laboratory. This station is situated on a beamline employing a six Tesla superconducting wavelength-shifter (Wiggler 16) which provides photon beams with a wide range of energies, extending to over 50 keV. The instrument[31] is a large, vertically-diffracting six circle diffractometer with a displex closed-cycle cryostat. A double bounce Si (111) monochromator was used for the experiment, so that higher resolutions up to 10^{-4} Å^{-1} could be achieved. A wavelength of 1.000±0.001 Å was chosen to maximize the x-ray flux and a beamsize of 0.5 mm horizontally and vertically was used in all measurements. Both double-axis geometry, using fine slits, and triple-axis geometry employing a Si(111) crystal analyzer, were used in our measurements. In double-axis configuration, the vertical beam-defining and detector slits were both set at 0.5 mm, optimised to provide good wavevector resolution and low background levels without sacrificing significant diffraction intensity. A cooled solid state germanium detector was used with a narrow energy window to further decrease background scattering including fluorescence.

The single crystal of $Nd_{1/2}Sr_{1/2}MnO_3$ was grown by the flux method at Bell Laboratories. This sample had been previously characterized by a number of techniques[32], which indicated a T_{CO} = 160K.

The lattice parameters a=5.432 Å, b=7.633 Å, c=5.476 Å and $\alpha = \beta = \gamma = 90°$ were used throughout the measurements. The crystal was used with a natural growth face, not cut along some usual direction, such as [100], [010] and [001], but its normal direction to the sample surface with an area of ~2×2 mm^2 is [101]. The sample surface was polished to get a shiny and even surface using 1 μm diamond paste. A number of Bragg peaks were located, e.g., (2 0 2), (3 0 3), (4 0 4), (5 –2 3), (4 0 2), (4 –2 2) etc., and were used to calculate a ***UB*** matrix. All data were collected through reciprocal space scans along the longitudinal direction ***Q*** ([h 0 h]), and the transverse direction ***R***([-h 2h h]).

6.3 Results and discussion

6.3.1 CE-type charge ordering and charge-ordered domain walls (CODs)

Bragg peaks were carefully examined through the whole temperature range, they were observed to be very clean singlets with little background. A structural transition around T_{CO} ~ 160 K was also noticed via monitoring the change of intensities of Bragg peaks. The peak profile of the (5, -2, 3) reflection along the ***Q*** and the ***R*** directions is shown in Fig. 6.4, which was undertaken using both double-axis and triple-axis geometries at 100 K. This temperature, being below T_{CO}, is in the charge-ordered state.

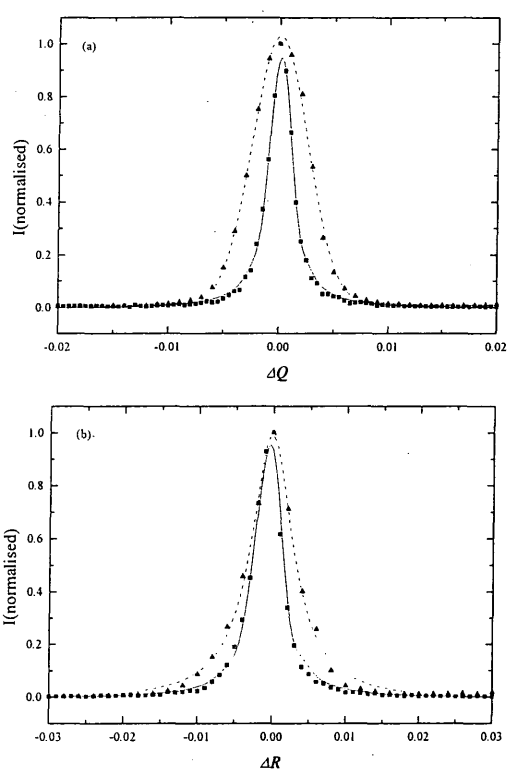

Fig. 6.4 The Bragg peak profile of the (5, -2, 3) at 100 K. Triangles represent data taken in double-axis mode, squares were obtained in tripe-axis model. Both dashed and solid lines are fittings by Gaussian or Lorentz functions, respectively. The peak intensities have been normalized to unity.

The narrower peaks obtained using triple-axis geometry indicate a higher intrinsic experimental resolution. Another notable feature is that the peak along the longitudinal direction ($\boldsymbol{Q}$) is still a very clear single peak even under the higher resolution. This indicates that this crystal (or *diffracting crystal domain*) is untwinned in terms of orthorhombicity. If there is an *a-c* twinned structure, which is most usual for this type of perovskite, then under such high resolution, it should be quite easy to observe the peak splitting along $\boldsymbol{Q}$ due to the difference in the values of *a* and *c* for $Nd_{1/2}Sr_{1/2}MnO_3$. Other Bragg peaks were also examined in triple-axis geometry, however none of the peaks display the splitting.

A careful search for charge ordering peaks was undertaken by scans within reciprocal space, and satellite peaks with a modulation wavevector $\boldsymbol{q}$ = (1/2, 0, 0), such as (2.5, 0, 2), (1.5, 0, 2), (4.5, 0, 4) and (3.5, 0, 4) were observed below 160 K. The most intense satellite was the (2.5, 0, 2), with almost 1000 counts/sec in double-axis model, and 100 counts/sec using Si(111) analyzer, this intensity corresponds to $10^{-3} \sim 10^{-4}$ less than that of related Bragg peaks. The peak profile of the (2.5, 0, 2) is shown in Fig. 6.5, in which the square symbols are the higher resolution data taken in triple-axis geometry.

The modulation of $\boldsymbol{q}$ = (1/2, 0, 0) indicates a superlattice doubling of the unit cell along the *a*-axis. As discussed above, such a charge modulation is implied in the proposed CE-type model, in agreement with observations in $La_{1/2}Ca_{1/2}MnO_3$[33] and $Nd_{1/2}Sr_{1/2}MnO_3$[20, 27], both taken from synchrotron radiation powder x-ray diffraction.

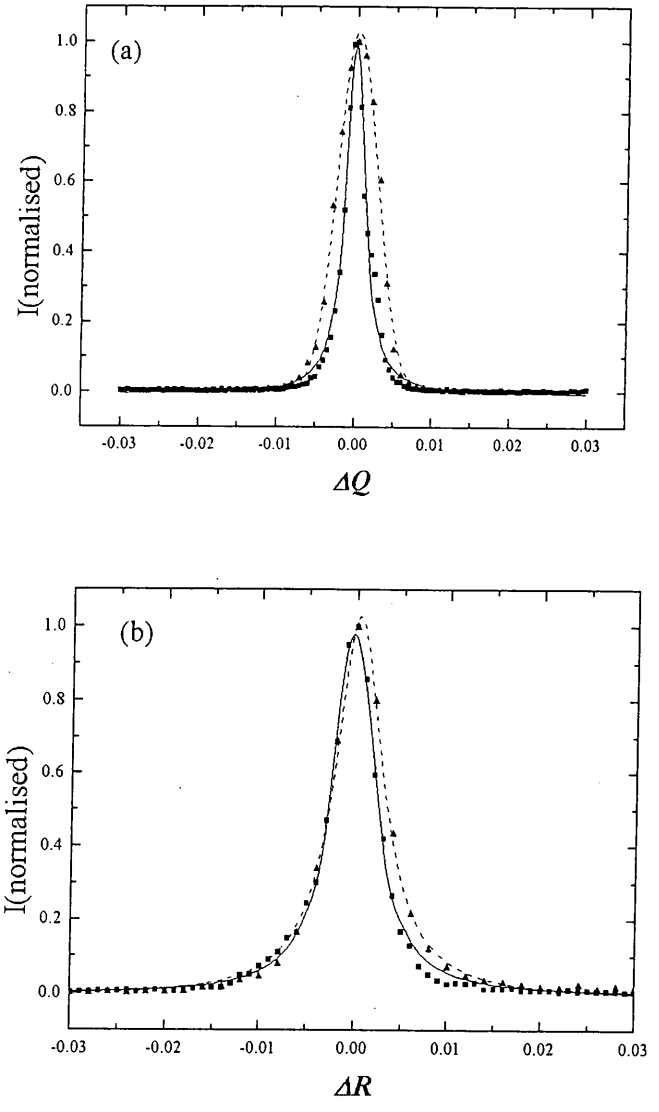

Fig. 6.5 The profile of the (2.5, 0, 2) satellite reflection at 100 K. Triangle symbols show the data taken in double-axis mode, square symbols show the data obtained in triple-axis geometry. Both dashed and solid lines are fittings by a Gaussian or Lorentz functions, respectively. The intensities have been normalized.

In addition, however, satellite peaks with $\boldsymbol{q}$ = (0, 0, 1/2), such as (2, 0, 2.5), (2, 0, 1.5) and (4, 0, 3.5), were observed below 160 K. these show a quite similar temperature behaviour to the (1/2, 0, 0)-type satellites. They also have comparable peak intensities and widths to those of the (1/2, 0, 0)-type satellite reflections. The temperature dependence of the peak intensities, as shown in Fig. 6.6, provides further evidence for a similar origin of these perpendicular modulations. Peak intensities along $\boldsymbol{Q}$ and $\boldsymbol{R}$ were obtained from integrating areas of Gaussian or Lorentzian fitted profiles, then normalized. All the data shown in Fig. 6.6 were collected using double-axis geometry. From Fig. 6.6, it is quite clear that both the (2.5, 0, 2) and (4, 0, 3.5) reflections appear at the same transition temperature upon cooling down the sample, 160 K, which can be termed as T_{CO}. A typical feature of a first-order phase transition also can be seen from Fig. 6.6, in which the intensities of the charge ordering reflections display a huge discontinous increase (almost 80%) in the vicinity of T_{CO} upon warming.

The observation of unspilt Bragg reflections along the longitudinal direction under high resolution excludes the possibility that these perpendicular modulations are due to *a-c* twinned domains. On the other hand, since two such types of modulations would give two sets of charge stripes perpendicular to each other in the *ac* plane, then in this scenario, the stripes would form a square grid. Reflections from a modulation with $\boldsymbol{q}$ = (1, 0, 1), rather than these two perpendicular modulations would then be expected to appear in diffraction. Furthermore, there have been considerable reports[11, 32, 34-36] of the existence of charge-ordered domains (CODs) in $La_{1/2}Ca_{1/2}MnO_3$ by electron microscopy. CODs have also been suggested to be a common feature in a number of perovskite manganites. In high resolution dark-field image technology, several CODs perpendicular to each other in one orthorhombic domain can been seen, which generate two perpendicular satellite reflections through electron diffraction. CODs have been found to have dimensions of around a few thousands angstroms.

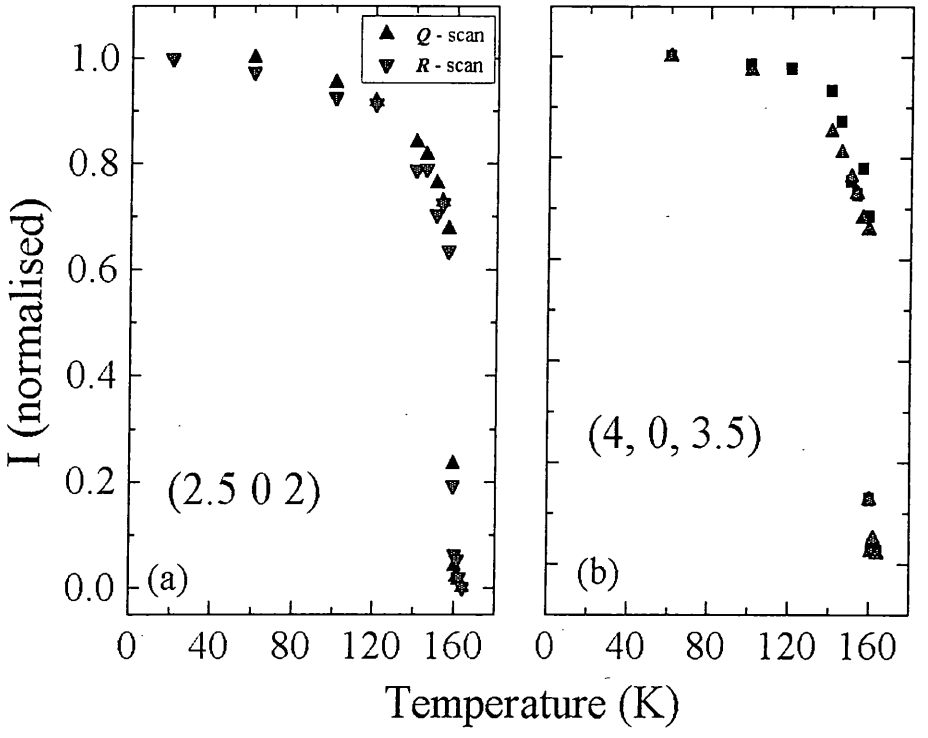

Fig. 6.6 Temperature dependence of the charge ordering reflections, (2.5, 0, 2) and (4, 0, 3.5). All data were taken using double-axis geometry.

As a consequence of the formation of CODs, satellite reflections originated from different CODs should still have some detectable difference, such as peak width which represents a different correlation length in a separate COD. Both the (2.5, 0, 2) and the (2, 0, 1.5) charge ordering peaks were carefully examined using a Si(111) analyzer, and the resulting data is shown in Fig. 6.5 and Fig. 6.7, respectively.

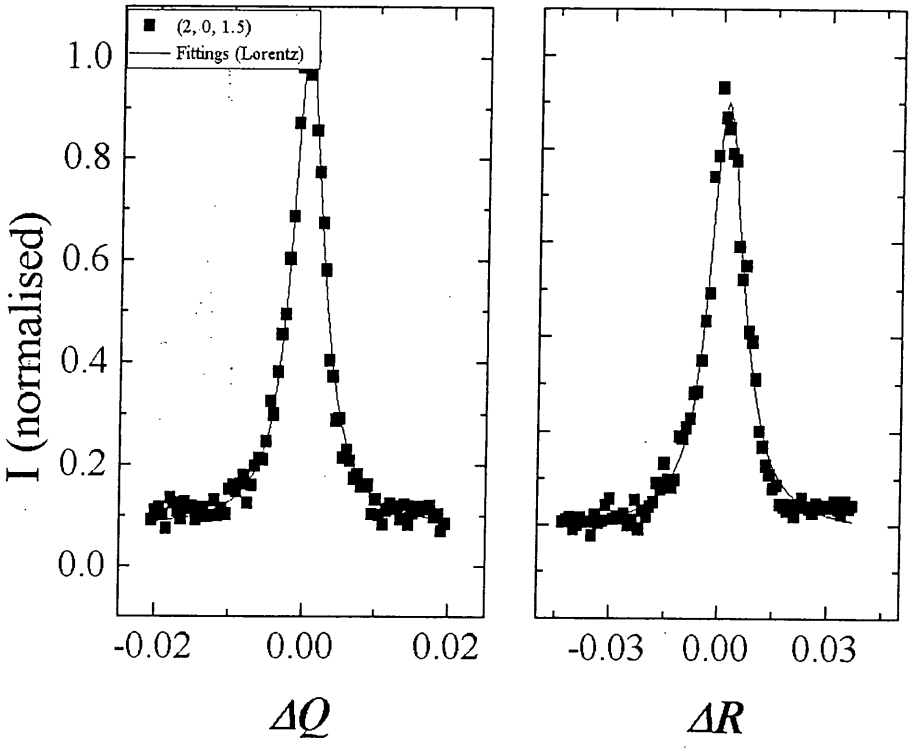

Fig. 6.7 Peak profile of the (2, 0, 1.5) satellite reflection taken in triple-axis geometry, at 100 K. Peaks are fitted by a Lorentz function, as shown by the solid lines.

The width (FWHM) and inverse correlation length of these two charge ordering peaks and a Bragg peak, are summarized in Table 6.1.

	Double-axis				Triple-axis			
	Q		***R***		***Q***		***R***	
	FWHM (r.l.u.)	ξ^{-1} (Å^{-1})	FWHM (r.l.u)	ξ^{-1} (Å^{-1})	FWHM (r.l.u.)	ξ^{-1} (Å^{-1})	FWHM (r.l.u.)	ξ^{-1} (Å^{-1})
Bragg (5, –2, 3)	0.0059	0.0048	0.0068	0.0078	0.0023	0.0019	0.0039	0.0045
CO-1 (2.5, 0, 2)	0.0060	0.0049	0.0061	0.0071	0.0028	0.0023	0.0051	0.0059
CO-2 (2, 0, 1.5)	0.0060	0.0049	0.0050	0.0063	0.0050	0.0041	0.0113	0.0131

Table 6.1 Comparison of FWHM and inverse correlation length (ξ^{-1}) for the Bragg peak (5, -2, 3) and two perpendicular charge ordering reflections

From Table 6.1, It can be noticed that both the (2.5, 0, 2) and the (2, 0, 1.5) have almost identical widths (FWHM) and inverse correlation lengths (ξ^{-1}), and the width of two CO reflections is almost equal to that of the Bragg peak using double-axis geometry, implying that the peak broadening of the CO reflections is dominated by the instrumental resolution. However, the situation is changed in the triple-axis data obtained employing a Si(111) analyzer. In the ***Q*** direction, we have a variation of the inverse correlation length

$$\xi^{-1}_{Bragg} < \xi^{-1}_{CO\text{-}1} < \xi^{-1}_{CO\text{-}2} \qquad (6.3)$$

leading to the following values of the correlation lengths (ξ),

$$\xi_{Bragg} \sim 520 \text{ Å} > \xi_{CO\text{-}1} \sim 434 \text{ Å} > \xi_{CO\text{-}2} \sim 244 \text{ Å} \qquad (6.4)$$

This result clearly demonstrates that the COD of the (2.5, 0, 2) has a different size compared to that of the (2, 0, 1.5). Thus these two perpendicular modulations are

generated from different CODs, but in the same orthorhombic domain. The comparison in the ***R*** direction gives a similar result, as follows,

$$\xi_{Bragg} \sim 222 \text{ Å} > \xi_{CO\text{-}1} \sim 168 \text{ Å} > \xi_{CO\text{-}2} \sim 76 \text{ Å} \qquad (6.5)$$

however, because of the relatively large mosaic width of this sample (~ 0.3°), the peaks along the transverse direction (***R***) would be dominated by the broadening effect of this mosaic width.

A very interesting result, which can also be noticed from above analysis, is that, these two charge ordering satellite reflections generated from different CODs both have shorter correlation length than that of Bragg reflections, as shown in Equations 6.4 and 6.5, indicating that the charge stripes are likely to be disordered and quenched even below T_{CO}. However, whether the correlation length of such quenched disordered charge stripes remains constant at the temperatures far below T_{CO} will need further measurements in the whole temperature range to clarify. The quenched disordered charge stripes will be further discussed based on experiments of $La_{5/3}Sr_{1/3}NiO_4$ in Chapter 7.

6.3.2 (1/2, 0, ½) and (1/2, 1, ½)-type modulations

So far, we have observed weak reflections from charge stripes, and also demonstrated the existence of charge-ordered domains. In this section, some additional satellite reflections, which have modulation wavevectors $\boldsymbol{q}_1$ = (1/2, 0, 1/2) and $\boldsymbol{q}_2$ = (1/2, 1, 1/2), will be discussed. These two sets of satellite reflections are not expected from the CE-type charge ordering formation. The peak profiles of two of these satellite reflections are shown in Fig. 6.8,. The intensities of both $\boldsymbol{q}_1$ and $\boldsymbol{q}_2$ modulated satellite reflections are much weaker than those of the CE-type charge ordering reflections, further reduced by a factor of 10. Furthermore, their peak widths (FWHM) are just slightly broader than those of CO reflections, as also shown in Fig. 6.8.

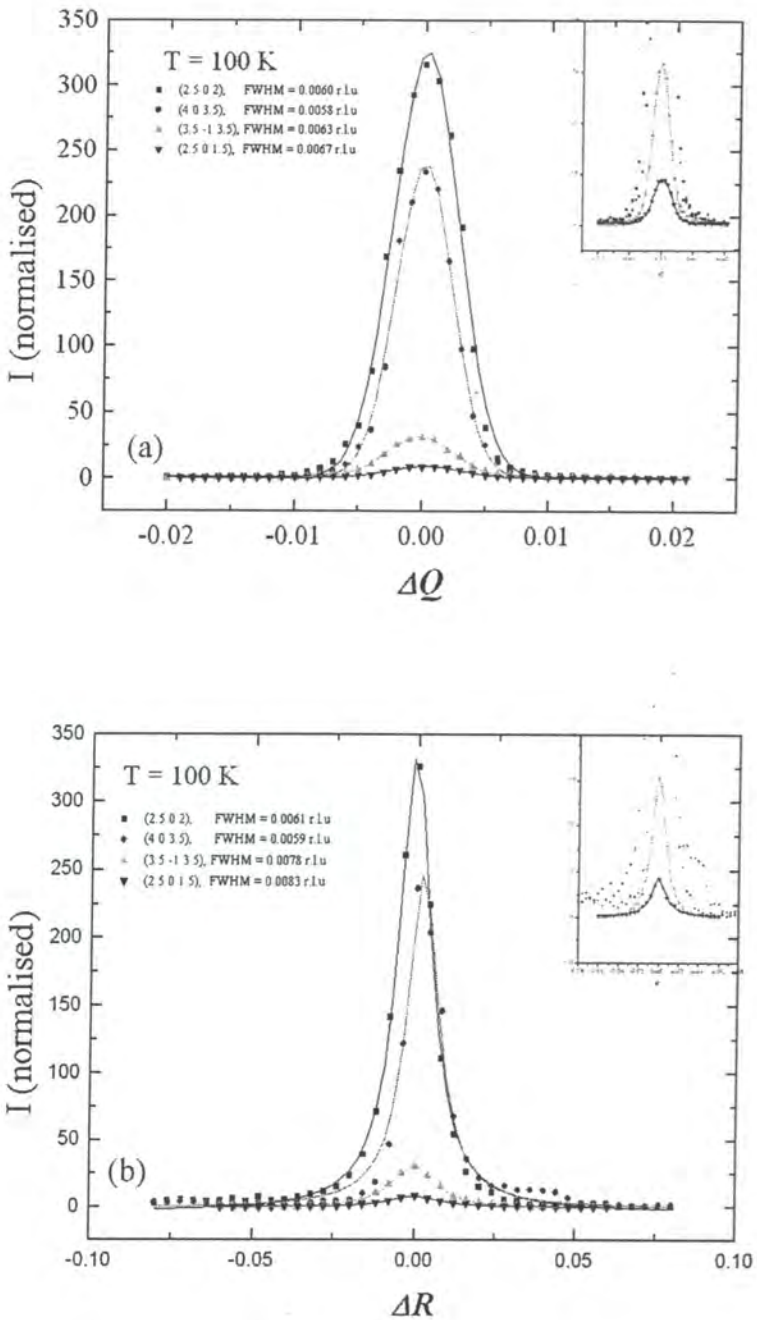

Fig. 6.8 The peak profiles of the (2.5, 0, 1.5) and the (3.5, -1, 3.5) reflections, compared to these of the (2.5, 0, 20 and (4, 0, 3.5) charge ordering reflections, at 100 K.

Since their intensities are extremely weak, less than 30 counts/sec, we have so far failed to collect convincing data using triple-axis geometry employing a Si(111) analyzer. The use of a more intense synchrotron source, e.g., the ESRF, will be essential to clarify the nature of these satellite reflections. In spite of the weak intensity, we still obtained the temperature dependence of the (2.5, 0, 1.5) and the (3.5, -1, 3.5) reflections in double-axis geometry, as shown in Fig. 6.9.

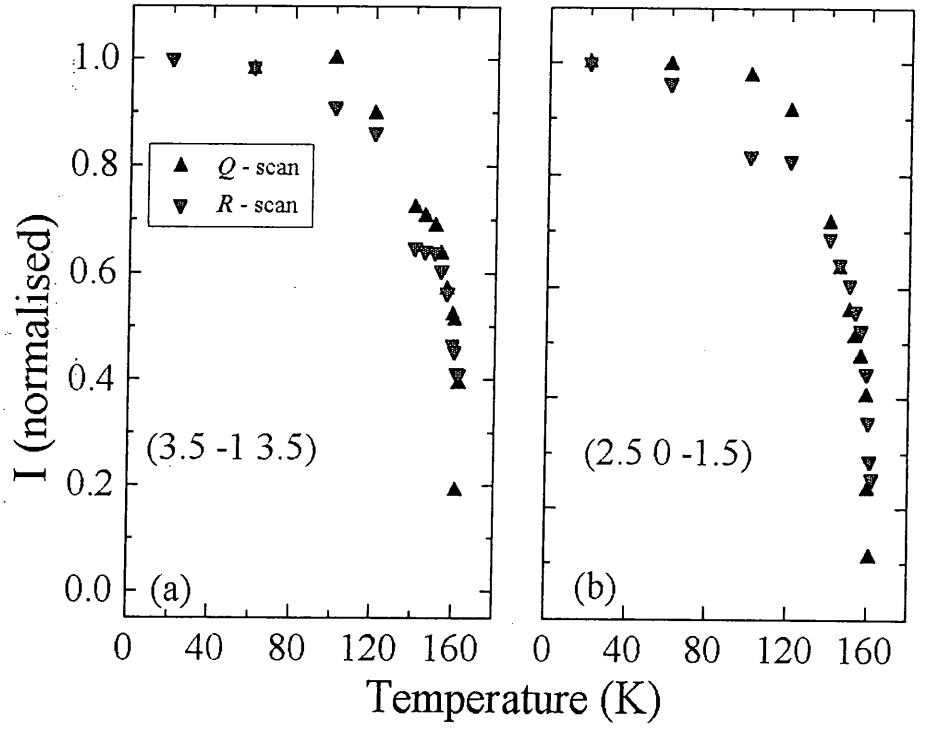

Fig. 6.9 The temperature dependence of the (2.5, 0, 1.5) and the (3.5, -1, 3.5) reflections

Fig. 6.9 (a) and (b) both display a quite similar behaviour to that of the previously discussed charge ordering satellite reflections, and indicate a phase transition temperature at around 160 K. It also can be noticed that the intensities of the CO reflections remains 80% of that at 156 K close to the T_{CO} (as shown in Fig. 6.6), but those weak reflections only have 30% for the (2.5, 0, 1.5) and 50% for the (3.5, -1, 3.5) at the same temperature. This suggests that the transition has a more continous nature for these additional reflections

According to previous neutron diffraction measurements[26], the (1/2, 1, 1/2)-type reflection has been observed, but was attributed to magnetic scattering from a modulated Mn^{4+} supercell. But, it is obvious that the (1/2, 1, 1/2)-type reflections observed in our measurements can not be generated from magnetic scattering, Because of the extremely weak magnetic scattering cross section, even with the use of synchrotron radiation, it is still too weak to detect any non-resonant magnetic scattering. However, if such magnetic ordering causes lattice strains, very weak reflections might be detected by x-ray diffraction. Additional experiments will be required to resolve this puzzle. It is worth noting that a very weak charge scattering was observed at positions consistent with non-resonant magnetic scattering from spin correlations in $La_{1.775}Sr_{0.225}NiO_4$ by high energy x-ray diffraction. The origin of this scattering also remains uncertain[37].

This (1/2, 0, 1/2)-type weak reflection is difficult to explain, because neither CO nor magnetic ordering can be attributed to its occurrence. However, if we look at the model of CODs, the effect of boundaries between two perpendicular CODs has so far been neglected. It was reported[35, 36] that the boundaries of the CODs are more or less parallel to the Mn-O-Mn direction of the simple perovskite structures, which is 45° from the CO wavevectors. The reconstruction of charge densities at the CODs boundaries could lead to a charge modulation with a propagation wavevector along the [1/2, 0, 1/2] direction, which is exactly 45° from the CO modulation wavevector. Because such a modulated charge density would be very low, the intensity of (1/2, 0, 1/2)-type reflections should be even much weaker than that of CO reflections. The intensity of the (2.5, 0, 1.5)

reflection is less than 10 counts/sec, the weakest one among all the observed satellite reflections.

Finally, it is also possible that these weak reflections are generated from mesoscopic separated phases in one orthorhombic domain. The coexistence of A-type and CE-type structures in $Nd_{1/2}Sr_{1/2}MnO_3$[28] and possible phase separation[20, 27] would also provide clue for further studies. Undoubtedly, further evidence will be needed to clarify these results.

6.4 References,

1 A. P. Ramirez, Journal of Physics-Condensed Matter **9**, 8171 (1997).

2 J. Fontcuberta, Physics World , 33 (1999).

3 C. Zener, Physical Review **82**, 403 (1951).

4 P. W. Anderson and H. Hasegawa, Physical Review **100**, 675 (1955).

5 P.-G. De Gennes, Physical Review **118**, 141 (1960).

6 A. J. Millis, P. B. Littlewood, and B. I. Shraiman, Physical Review Letters **74**, 5144 (1995).

7 A. J. Millis, B. I. Shraiman, and R. Mueller, Physical Review Letters **77**, 175 (1996).

8 A. J. Millis, Physical Review B-Condensed Matter **53**, 8434 (1996).

9 A. J. Millis, Nature **392**, 147 (1998).

10 H. Roder, J. Zang, and A. R. Bishop, Physical Review Letters **76**, 1356 (1996).

11 S.-W. Cheong and C. H. Chen, in *Colossal Magnetoresistance, Charge Ordering and Related properties of Manganese oxides*, edited by C. N. R. Rao and B. Raveau (World Scientific, Singapore, 1998), p. 241.

12 J. Inoue, Philosophical Transactions of the Royal Society of London Series a- Mathematical Physical and Engineering Sciences **356**, 1481 (1998).

13 T. Kimura, Y. Tomioka, A. Asamitsu, *et al.*, Physical Review Letters **81**, 5920 (1998).

14 H. Kuwahara, Y. Tomioka, A. Asamitsu, *et al.*, Science **270**, 961 (1995).

15 Y. Tokura, H. Kuwahara, Y. Moritomo, *et al.*, Physical Review Letters **76**, 3184 (1996).

16 H. Kuwahara and Y. Tokura, in *Colossal Magnetoresistance, Charge Ordering and Related properties of Manganese oxides*, edited by C. N. R. Rao and B. Raveau (World Scientific, Singapore, 1998), p. 217.

17 Y. Tokura, Current Opinion in Solid State & Materials Science **3**, 175 (1998).

18 M. Imada, A. Fujimori, and Y. Tokura, Reviews of Modern Physics **70**, 1039 (1998).

19 V. Caignaert, F. Millange, M. Hervieu, *et al.*, Solid State Communications **99**, 173 (1996).

20 P. M. Woodward, D. E. Cox, and T. Vogt, Preprint (1998).

21 G. Burns and A. M. Glazer, *Space Group for Solid State Scientists* (Academic Press, Boston, 1990).

22 E. O. Wollan and W. C. Koehler, Physical Review **100**, 545 (1955).

23 J. B. Goodenough, Physical Review **100**, 564 (1955).

24 J. B. Goodenough, A. Wold, R. J. Arnott, *et al.*, Physical Review **124**, 373 (1961).

25 H. Kawano, R. Kajimoto, H. Yoshizawa, *et al.*, Physica B **241**, 289 (1997).

26 H. Kawano, R. Kajimoto, H. Yoshizawa, *et al.*, Physical Review Letters **78**, 4253 (1997).

27 P. M. Woodward, T. Vogt, D. E. Cox, *et al.*, Physical Review Letter (submitted) (1998).

28 H. Kawano, R. Kajimoto, H. Yoshizawa, *et al.*, cond-mat/9808286 (1998).

29 H. Yoshizawa, H. Kawano, J. A. FernandezBaca, *et al.*, Physical Review B-Condensed Matter **58**, R571 (1998).

30 M. Kubota, H. Yoshizawa, Y. Moritomo, *et al.*, cond-mat/9811192 (1998).

31 S. P. Collins, R. J. Cernik, B. Fell, *et al.*, Journal of Synchrotron Radiation **5**, 1263 (1998).

32 S.-W. Cheong, T. Katsufuji, and C. H. Chen, (private communication, 1998).

33 P. G. Radaelli, D. E. Cox, M. Marezio, *et al.*, Physical Review B-Condensed Matter **55**, 3015 (1997).

34 K. Yamada and e. al., Physica C **221**, 355 (1994).

35 C. H. Chen and S. W. Cheong, Physical Review Letters **76**, 4042 (1996).

36 C. H. Chen, S. W. Cheong, and H. Y. Hwang, Journal of Applied Physics **81**, 4326 (1997).

37 A. Vigliante, M. vonZimmermann, J. R. Schneider, *et al.*, Physical Review B-Condensed Matter **56**, 8248 (1997).

Chapter 7

Quasi-two-dimensional charge stripes in single crystals $La_{5/3}Sr_{1/3}NiO_4$

Unlike those observed in $Bi_{0.24}Ca_{0.76}MnO_3$, $Nd_{0.5}Sr_{0.5}MnO_3$ and other perovskite manganites, the charge stripes in $La_{2-x}Sr_xNiO_4$ are quasi two-dimensional (2D). In this chapter, this feature was comprehensively demonstrated by studying single crystals of $La_{5/3}Sr_{1/3}NiO_4$ using synchrotron radiation x-ray scattering. $La_{5/3}Sr_{1/3}NiO_4$, shows some intriguing properties, undergoing a second-order phase transition to a charge-ordered state upon cooling down below T_{CO} (~ 240 K), which was symbolised by the appearance of weak charge stripe satellites. In a series of initial measurements, satellite peaks due to charge stripe scattering were observed to have a modulation wavevector $\boldsymbol{Q}_1$ = (2/3, 2/3, 1) in the (hhl) zone. The temperature dependence of the integrated intensities and the full-width-at-half-maximum (FWHM) of these satellite reflections along the longitudinal and transverse directions was measured, which demonstrates the second-order nature of the charge ordering transition. The critical exponents, $2\beta \sim 0.25$ and $\nu \sim 1$, were obtained by fitting the data to power laws. These values are in agreement with those of a 2D-Ising model. In later measurements, the satellite reflections were observed to appear at different positions, characterised by a modulation wavevector $\boldsymbol{Q}_2$ = (2/3, 0, 1) in the (h0l) zone. This observation is consistent with other results via neutron and electron diffraction. It has been further confirmed that the charge stripes are shown to be 2D in nature both by the measurements of their correlation lengths and by critical exponents of the charge stripe phase transition. One of most interesting observations is that, even at very low temperatures, the charge stripes do not develop long-range

order, indicating that the charge stripes are disordered and quenched below T_{CO}. Following recent theoretical predications for a possible similarity between the stripes and the electronic liquid-crystal phases (ELC), this result likely can be interpreted as the first direct evidence for the existence of a low temperature smectic stripe phase, which is followed by a nematic phase due to increasing transverse stripe fluctuations, then by a disordered stripe liquid state as the temperature is increased.

7.1 Introduction

In previous chapters, charge stripes in $Bi_{0.24}Ca_{0.76}MnO_3$, $Nd_{0.5}Sr_{0.5}MnO_3$ were extensively studied by single crystal x-ray scattering. A common feature for those charge stripes is that they are long-range correlated in all three dimension (3D), despite being described as the ordering of doped holes within the Mn-O layers. However, the "layer" referred to in the 3D perovskite manganites is not due to a real layered structure. There exist some truly structural layered perovskite transition-metal oxides, such as $La_{2-x}Sr_xMnO_4$[1-3] (n = 1), $La_1Sr_2Mn_2O_7$ (n = 2)[4], both of which show quite anisotropic properties between in-plane and out-of-plane direction. The spatial dimensionality of the charge stripes in these materials is, therefore strongly associated with the dimensionality of their structures. The charge stripes appearing in the 3D perovskite manganites can be described more suitably by the concept of a "charge sheet", or "charge wall", as schematically shown in Fig. 7.1 (a). In contrast, the charge stripes formed in the 2D-layer compounds are 2-dimensional in nature, as shown in Fig, 7.1 (b), in which the charge stripes are long-range ordered only in the 2D planes. However, in real material systems, the charge stripes would still retain some finite correlation between the layers, thus they would appear as a quasi-2D feature.

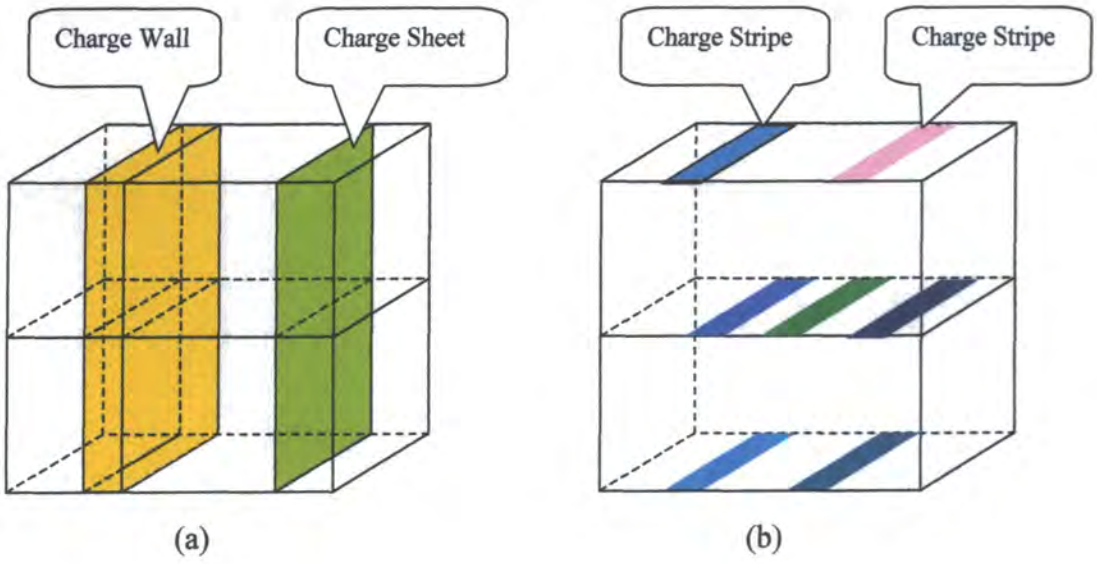

Fig. 7.1 A schematic view of the charge stripes in the 3D and 2D structures

In this chapter, the quasi-2D feature of the charge stripes in the hole-doped nickelate compound $La_{5/3}Sr_{1/3}NiO_4$ was extensively studied by synchrotron radiation x-ray scattering.

Both La_2NiO_4 and La_2CuO_4 are 2D antiferromagnetic (AF) insulators with layered MO_2 (M = copper or nickel) planes, which means the coupling of spins within each metal-oxygen plane is much stronger than that between spins in neighbouring planes. When holes are doped into the MO_2 planes via substitution with strontium, $La_{2-x}Sr_xCuO_4$ eventually shows a metallic behaviour and the maximum T_C for the superconductivity is reached for $x \approx 0.15$, and the long-range AF is replaced by incommensurate (IC) spin fluctuations, which show a 2D feature[5, 6].

$La_{2-x}Sr_xNiO_4$ is isostructural with the high T_C material $La_{2-x}Sr_xCuO_4$, shows very similar metallic behaviour when the doping level of $x \approx 1$ is reached, and similar 2D IC spin fluctuations, as discovered by Hayden *et al.*[7], but no superconductivity exists.

At sufficient high levels of doping, the holes tend to order in a stripe-like structure acting as domain walls within NiO_2 planes. The existence of charge stripes in $La_{2-x}Sr_xNiO_{4+\delta}$ has been well established by a number of measurements via neutron[8-16], electron[17] and x-ray[18] scattering.

The quasi-2D feature of charge stripes was initially revealed by an electron diffraction experiment on $La_{2-x}Sr_xNiO_4$ ($0 \leq x \leq 1$) powder[17]. By comparing the peak width of the same superlattice spot in the two perpendicular cross sections of the reciprocal space, it was found that the correlation length of the charge ordering reflections in the NiO_2 planes is around 500 Å, however, it is shorter than 60 Å perpendicular to the NiO_2 layers.

There were also a few reports on the measurements of neutron scattering on single crystals of layered $La_{0.5}Sr_{1.5}MnO_4$[1] and $La_{5/3}Sr_{1/3}NiO_4$[19] compounds. The quasi-2D feature of the charge stripes was also realised by measuring the anisotropic correlation lengths in the Mn-O or Ni-O planes and the directions perpendicular to these planes. A recent observation in a single crystal $La_{5/3}Sr_{1/3}NiO_4$, which displays a very large anisotropic resistivity[20] between the *ab* plane and the direction along the *c*-axis appears below T_{CO}, is a further evidence for the quasi-2D behaviour of charge stripes.

Among all the hole-doped La_2NiO_4 compounds, $La_{5/3}Sr_{1/3}NiO_4$ is the one studied most extensively, because of its abnormal behaviour observed in many properties, such as resistivity and magnetic susceptibility[21], sound velocity and specific heat[22], optical conductivity spectra[20], Raman spectra[23-25] and nuclear magnetic resonance[26]. The formation of charge stripes and spin ordering was attributed to the occurrence of these intriguing behaviours. Recent electron diffraction[17] and neutron scattering[19] measurements have demonstrated the existence of charge stripes and spin ordering when cooling below $T_C = 240$K and $T_S = 190$K, respectively.

The neutron scattering measurements[19] have also revealed that $La_{5/3}Sr_{1/3}NiO_4$ undergoes three successive transitions associated with the melting of the quasi-2D charge stripes and spin ordering in the NiO_2 planes, as shown in Fig. 7.2. It was indicated that the two lower temperature phases have quasi-long-range in-plane charge correlation. When the lattice of 2D charge stripes melts, it goes through an intermediate glass state before becoming a disordered liquid state. This intermediate glass state was termed a "stripe glass".

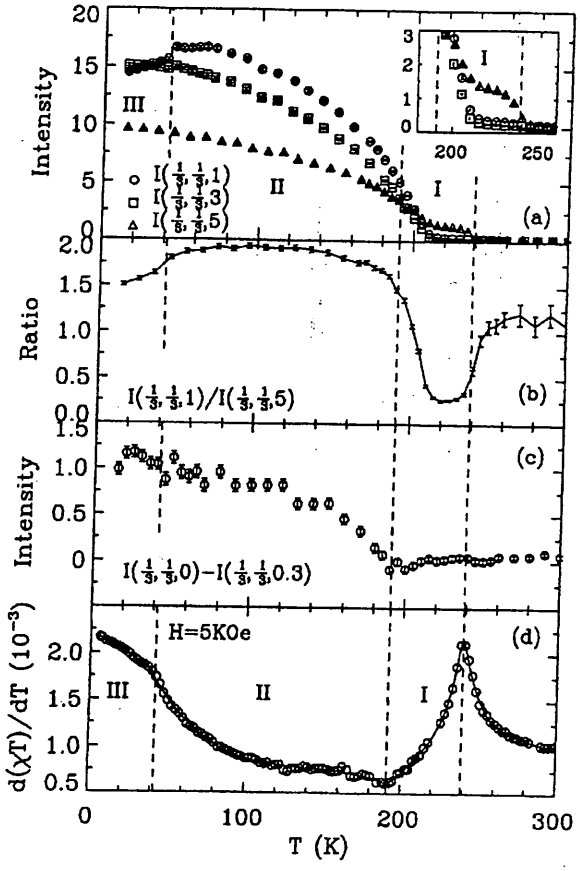

Fig. 7.2 (a) Temperature dependence of the superlattice peak intensities at the (1/3, 1/3, 1), (1/3, 1/3, 3) and (1/3, 1/3, 5). (b) Ratio of the (1/3, 1/3, 1) peak intensity to the (1/3, 1/3, 5) peak. (c) Temperature dependence of the magnetic superlattice peak intensity. (d) $d(\chi T)/dT$ in emu/mole. (taken from Lee and Cheong[19])

However, the structural correlation in $La_{5/3}Sr_{1/3}NiO_4$ has yet to be investigated by high resolution x-ray scattering techniques. In particular, the quasi-2D feature of the charge stripes in this compound need to be further confirmed by x-ray scattering which has a higher wavevector resolution. Neutron scattering is not directly sensitive to the charge ordering, but rather the charge order is detected indirectly through displacements of the nuclear positions because of the associated strain deforming the lattice. The requirement for the large size single crystals in neutron scattering, will often make the resolution worse because of the larger sample mosaic spread, bigger density inhomogeneity and strain disorder. In addition, the counting rate at charge stripes peaks achievable with synchrotron x-rays is much greater than that obtained using reactor neutron sources. In previous chapters, it has been demonstrated that synchrotron radiation x-ray scattering is fully capable of making high resolution measurements on charge stripes.

7.2 Experimental details

The synchrotron experiments were performed both at the station 16.3 at the SRS, Daresbury Laboratory, and on the beamline XMaS CRG (BM28) at the ESRF. A double-bounce Si (111) monochromator was used at the SRS. Initial measurements mainly were undertaken at the station 16.3. A wavelength of 0.8 Å was chosen to maximise the x-ray flux and penetration depth.

The beamline XMaS CRG has a versatile 11-axis Huber diffractometer with a similar displex closed-circle cryostat. The incident x-ray was selected to be 1 Å using a Si(111) monochromator and most of high-order contamination were rejected by the use of a focusing mirror, which also hugely increases the flux at the sample.

Double-axis geometry using very fine slits, without the use of a crystal analyzer, was employed in both beamlines for all measurements. Both anti-scatter and detector slits

were carefully adjusted to reduce the background and increase the wavevector resolution. Both Bicron NaI(Tl) scintillation detector (XMaS) and Ge solid state detectors (16.3 and XMaS) were employed to make measurements.

The single crystals of $La_{1.67}Sr_{0.33}NiO_4$ were grown using the floating zone method at Bell Laboratories. Two different crystals (crystals A and B) were measured. Both were previously characterised by the bulk susceptibility measurement $d(\chi T)/dT$ as shown in Fig. 7.2, indicating a charge ordering transition at $T_C \sim 240$ K. The surface of crystal B was mechanically polished using 1μ diamond paste. An orthorhombic cell (or pseudo-tetragonal $F4/mmm$) with a unit-cell size $\sqrt{2}\, a_t \times \sqrt{2}\, a_t \times c_t$ relative to the basic body-centered-tetragonal cell ($I4/mmm$) was adopted through all the measurements, however, the structural refinement from the latest powder x-ray diffraction data shown a lower symmetry $F112/m$ due to the structural effect of Sr substitution[27]. The crystal structure of $La_{1.67}Sr_{0.33}NiO_4$ is shown in Fig. 7.3. Initial measurements on the intensities and positions of the Bragg peaks versus temperature showed no structural transitions over the whole temperature range, $10 \sim 300$ K.

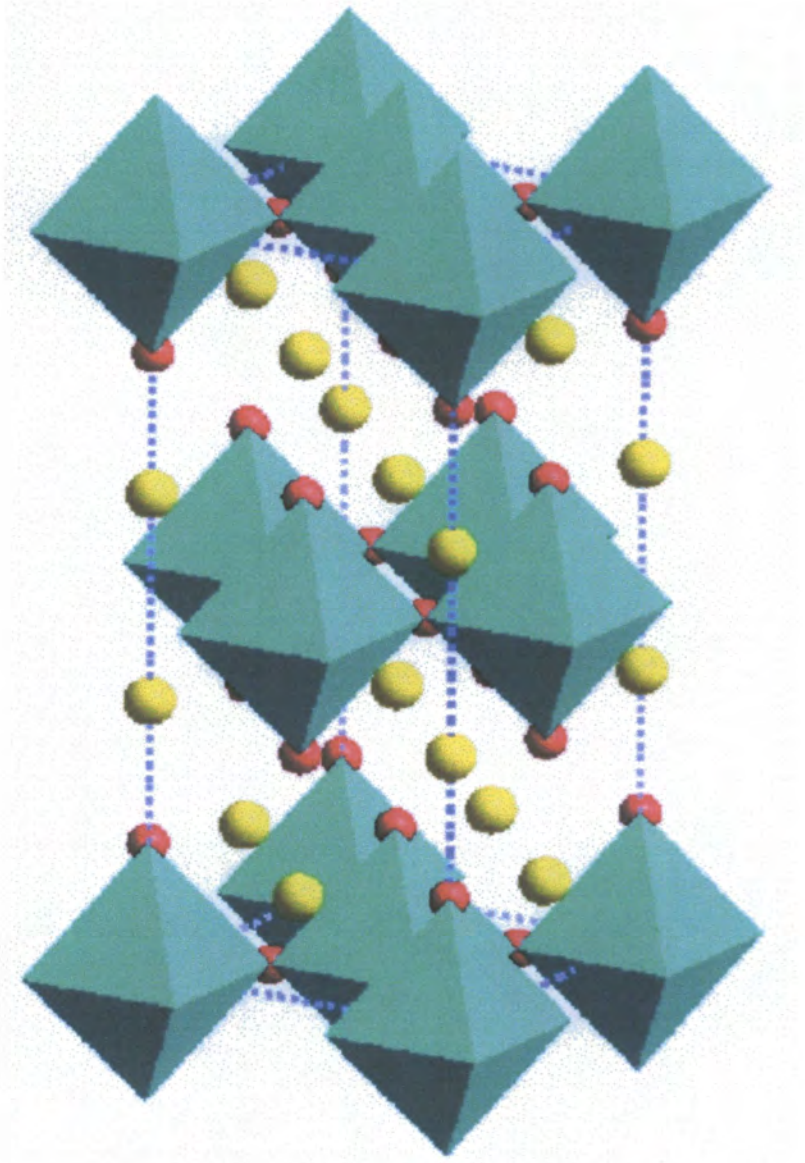

Fig. 7.3 The crystalline structure of $La_{1.67}Sr_{0.33}NiO_4$

7.3 Results and discussion

The measurements on sample A were undertaken at the station 16.3, at the SRS. A schematic search for the charge-stripe reflections below T_{CO}, was done at 20 K by scanning along four different directions in the (*h, h, l*) zone, as shown in Fig. 7.4.

In Fig. 7.4 (1), one peak with almost 800 counts/20sec can be clearly seen at the (3.33, 3.33, 1) position, another two relative weak peaks (~ 120 counts/20sec) at the (3.33, 3.33, –1) and the (3.33, 3.33, 5) can also been noticed. The very strong and clear two peaks, which were assigned as the (3.67, 3.67, 2) and the (3.67, 3.67, 4), can also be observed in the long scan along the (3.67, 3.67, *l*) direction in Fig. 7.4. (2). All the peaks have the intensities approximately 10^{-4} that of the Bragg reflections and a consistent modulation wavevector $\boldsymbol{Q}_1$ = (2/3, 2/3, 1). Such a modulation wavevector is further confirmed via the scans along the (*h*, *h*, 2) and (*h*, *h*, 1) directions, as shown in Fig. 7.4. (3) and (4), respectively, in which the satellite reflections are found to be related to the neighboring Bragg peaks with a modulation wavevector $\boldsymbol{Q}_1$ = (2/3, 2/3, 1). All observed satellite reflections disappear above ~ 240 K via measuring the temperature dependence of their intensities, indicating that all these satellite reflections are related to the formation of charge stripes.

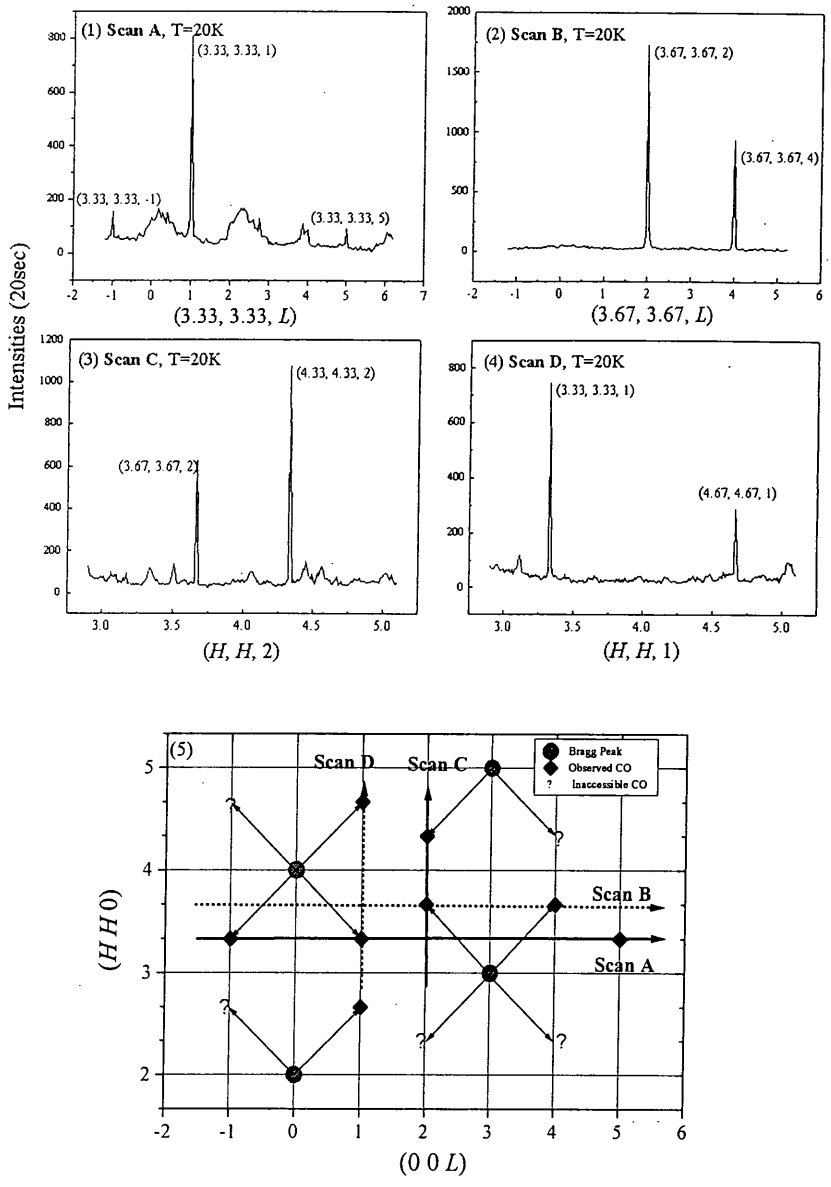

Fig. 7.4 (1)-(4) Scans taken in various directions in reciprocal space displaying charge stripe order, (5) A reciprocal space map showing the location, and relationship of charge order satellites. Data were taken at 20 K at the SRS.

Some very broad features along the (3.33, 3.33, *l*) direction, such as those around the positions of (3.33, 3.33, 0.33) and (3.33, 3.33, 2.33), can be noticed, as shown in Fig. 7.4. (1). These only have intensities around 130 counts/20sec, sitting on the background of 50 counts/20sec, almost one order of magnitude weaker than that of the charge ordering satellites. These peaks are likely to be associated with diffuse scattering due to the doping effects of the Sr atoms.

Further measurements on the same sample were done on the beamline XMaS, at the ESRF, which demonstrated a charge ordering reflection at the (3.67, 3.67, 2) with an intensity as high as 20,000 counts/sec, almost a factor of 150 increase compared to that measured at the SRS, as shown in Fig. 7.5.

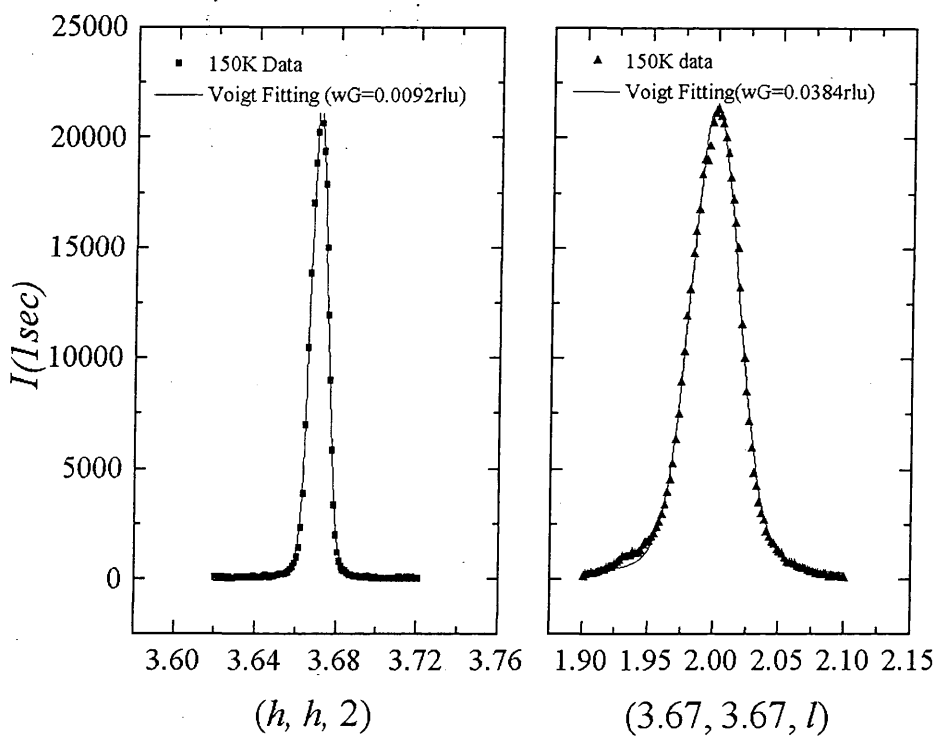

Fig. 7.5 The peak profile of the charge ordering reflection (3.67, 3.67, 2) of sample A , at 150 K. The lines are fittings of a Voigt function.

Due to the effects of mosaic spread of specimen and other uncertainties in the collimator resolution and monochromator mosaic spread, a Voigt function was used for the analysis of the x-ray peak shapes, which is a convolution of a Lorentz function and the Gaussian instrumental resolution function[28, 29].

The evidence for the 2D behaviour was obtained from the critical scattering measurements. Measurements of the integrated intensity and the FWHM of the charge stripe satellite reflection (3.67, 3.67, 2) were undertaken in the temperature range 150 K < T < 250 K, as shown in Fig. 7.6. The peak intensity starts to has a very large decrease upon warming up approaching 220 K. Both the longitudinal and transverse scans show a very similar behaviour, indicating $T_{CO} \approx 220$ K. The FWHM of the charge ordering satellite reflection starts to dramatically broaden above 220 K, which indicates a second-order phase transition in nature.

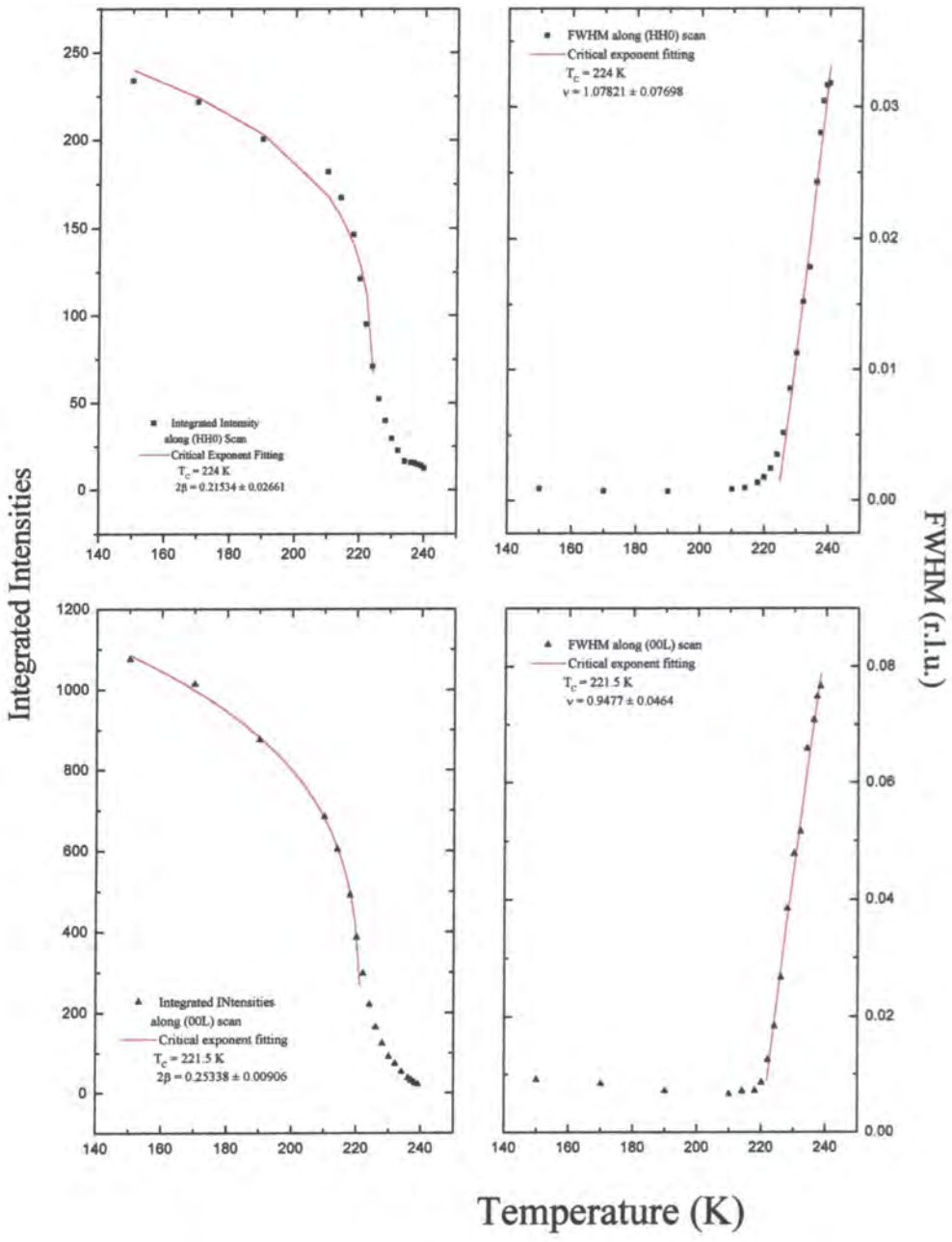

Fig.7.6 The temperature dependence of the integrated intensity and FWHM of the charge stripe satellite reflection (3.67, 3.67, 2) along the longitudinal and transverse directions, as shown as solid dots and triangles, respectively. The solid lines are the best fittings to the power laws discussed in text.

The following power laws were chosen to fit the order parameter (integrated intensity $I(T)$) and the width (κ) in both the longitudinal and transverse directions,

$$I(T) = I_0 \left| \frac{T - Tco}{Tco} \right|^{2\beta} \tag{7.1}$$

and

$$\kappa(T) = \kappa_0 \left| \frac{T - Tco}{Tco} \right|^{\nu} \tag{7.2}$$

The critical exponents, 2β and ν, were found to have the following values,

$$0.22 \pm 0.03 \leq 2\beta \leq 0.25 \pm 0.009 \tag{7.3}$$

and

$$0.95 \pm 0.046 \leq \nu \leq 1.07 \pm 0.077 \tag{7.4}$$

which are very close to the predicated exponents of a 2D-Ising model, $2\beta = 0.25$ and $\nu = 1.0$, as shown in Table 7.1[30], in which the approximate values of critical exponents for various 2D and 3D models are listed. This result clearly demonstrates that the charge stripes in $La_{1.67}Sr_{0.33}NiO_4$ belong to the 2D universality class.

	2β	ν
2D Ising	0.25	1.0
3D Ising	0.624	0.64
3D Heisenberg	0.76	0.702
3D *X-Y*	0.692	0.669

Table 7.1 Approximate values of critical exponents for various models (taken from Collins[30])

This result is also in accord with some theories discussed in Chapter 3, for example, one solution for a classical 2D-Ising model indicated that the stripe phase and charge inhomogeneity are the expected consequences from the frustrated phase separation[31], another numerical density matrix renormalisation group (DRMG) calculations based on a 2D *t-J* model also result a charge-stripe scenario[31-34].

However, this modulation wavevector for charge stripes reflections obtained from above measurements is not quite consistent with that in previous neutron[19] and electron diffraction[35] measurements, which are characterized both by $\boldsymbol{Q}_2$ = (2/3, 0, 1) in the (*h*0*l*) zone. To clarify this difference, further measurements[36] for the charge stripe ordering in another surface-polished crystal, the sample B, were undertaken on the beamline XMaS CRG. The instrumental resolution function was determined to be ξ_H^{-1} ~ 0.0034 Å^{-1}, ξ_K^{-1} ~ 0.002 Å^{-1}, and ξ_L^{-1} ~ 0.006 Å^{-1} as measured on the Bragg Peak (5, 1, 5), which displays very clean singlet, at 100 K. The satellite reflections were observed with a modulation wavevector $\boldsymbol{Q}_2$ = (2/3, 0, 1). Attempts to locate both types of charge ordering in a single crystal has so far failed. Mis-refinement of the ***UB*** matrix could cause this difference, since only a 2D refinement was adopted in these initial measurements, comparing to a 3D refinement used in later measurements. However, the satellite reflections with a modulation wavevector $\boldsymbol{Q}_1$ =

(2/3, 2/3, 1) are also likely related to some uncertain sample-dependent effects, due to a different T_{CO} at 220 K. Further clarification is needed in future studies. The linear scans through the charge ordering peak (5.33, 0, 7) along the *h*, *k* and *l* directions are shown in Fig. 7.7.

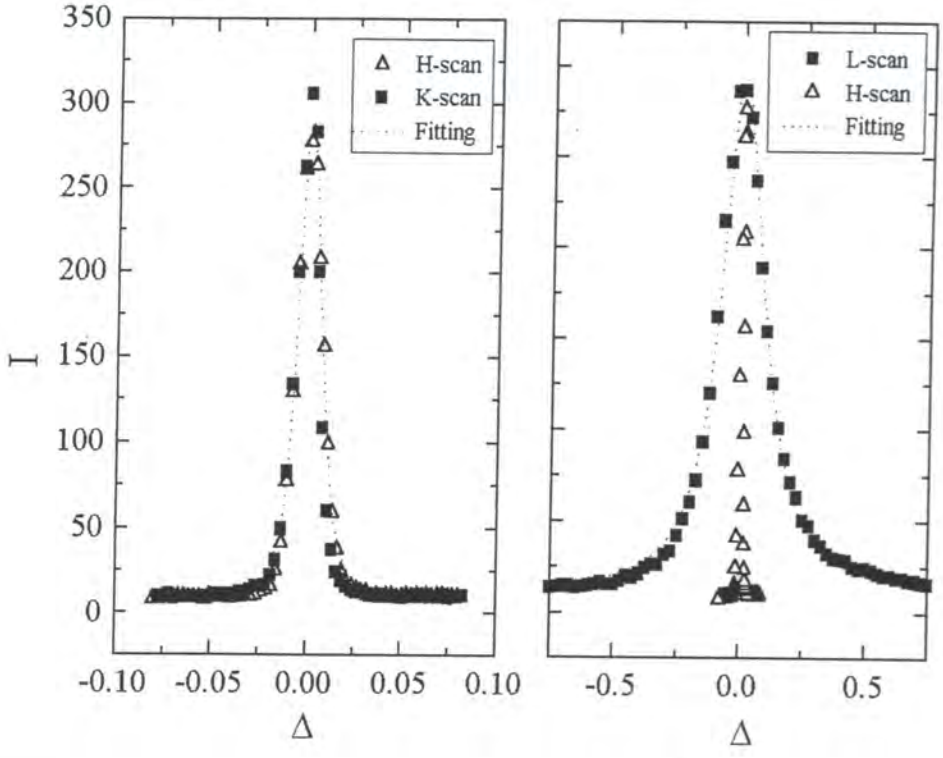

Fig. 7.7 Linear scans through the (5.33, 0, 7) at T = 226 K. The dotted lines are fittings of a Gaussian function convoluted with the instrumental resolution function.

The dotted lines show the best fittings convoluted with the instrumental resolution function. It is clear that the profile of the charge stripe satellite along the *h*, *k* directions are nearly identical, but it is much wider in the *l* direction. Further measurements in the temperature range 100 K ≤ T ≤ 250 were undertaken. The best fittings to the charge ordering peaks giving the correlation lengths along 3 directions are listed in Table 7.2.

	ξ_H (Å)	ξ_K (Å)	ξ_L (Å)
227 K	133	220	17
250 K	56	55	12
255 K	32	33	< 12

Table 7.2 Correlation length of the charge ordering peak (4.66, 0, 5) at temperature below and above the transition temperature $T_{CO} \approx 240$ K.

ξ_H and ξ_K represent in-plane (the *ab* plane) correlation length of the charge stripes, while ξ_L represents out-of-plane (along the *c*-axis) correlation length. Below T_{CO}, at 227 K, the anisotropy of correlation lengths between the in-plane and our-of-plane is shown as follows,

$$\frac{\xi_H}{\xi_L} \approx \frac{\xi_K}{\xi_L} \geq 10 \qquad (7.5)$$

This indicates that the charge stripes are short-range correlated along the *c*-axis with the correlation length only equal to 2 ~ 3 Ni-O layers, but they are quasi-long-range correlated in the Ni-O plane. This is the first direct demonstration for the quasi-2D feature of the charge stripes in $La_{5/3}Sr_{1/3}NiO_4$ via x-ray scattering.

The quasi-2D nature can be further determined by the measurements of the critical scattering of the charge stripe satellites. Fig.7.8 and Fig.7.9 show the temperature dependence of the integrated intensities and the evolution of the inverse correlation lengths (ξ^{-1}) of the charge stripe reflection (4.66, 0, 5), respectively.

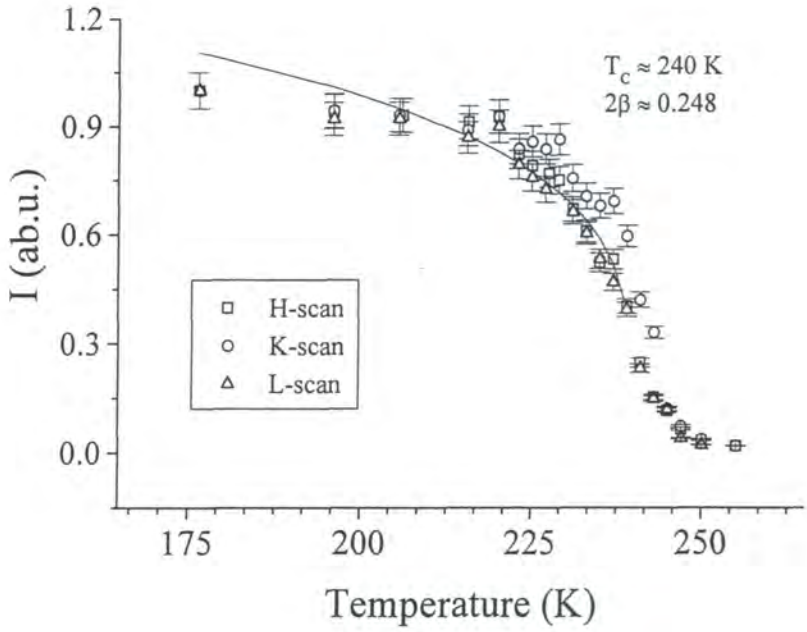

Fig. 7.8 Temperature dependence of integrated intensities of (4.66, 0, 5) along *h*, *k* and *l* directions, the solid line is the best fit to a power law, as represented by Equation 7.1.

The critical exponent 2β can be given via fitting data by a power law shown in Equation 7.1 as follows

$$2\beta \approx 0.248 \qquad (7.6)$$

From Table 7.1, It is clear that the exponent 2β of the charge stripes are in best agreement with that of a 2D-Ising model. This is another evidence for the quasi-2D feature of charge stripes in $La_{5/3}Sr_{1/3}NiO_4$.

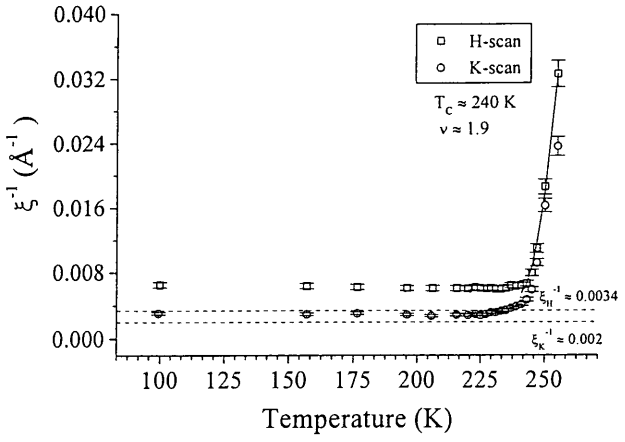

(a)

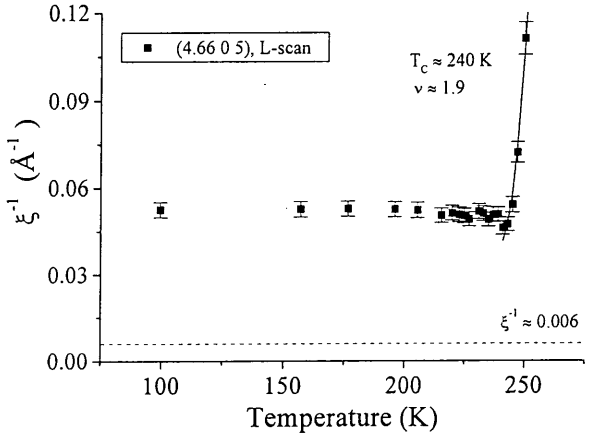

(b)

Fig. 7.9 (a)The evolution of the inverse correlation lengths of the (4.66, 0, 5) along *h* and *k* directions. (b) The evolution of the inverse correlation lengths of the (4.66, 0, 5) along *l* direction. The solid lines are best fits by a power law, as shown in Equation 7.2. Dotted horizontal lines are indications of the instrumental resolution function.

However, as shown in Fig. 7.9, the fits along three directions give an unusually high value for exponent ν around 1.9, which does not correspond to the values of any known universality class. The randomly distributed impurities are likely responsible for the loss of long-range order, thus increasing the exponent of the correlation length[36] of the charge stripes. All fits give a similar transition temperature T_{CO} at around 240 K which is in agreement with transport measurements.

One of the most surprising observations is that correlation lengths of the charge stripes in 3 directions remain above the instrumental resolution even at temperatures far below T_{CO}, indicating that charge stripe ordering is disordered and quenched below T_{CO}, as shown in Fig. 7.9. The pinning potential provided by the Ni ions, the defects induced by the Sr dopants, or the combination of both are likely responsible to the quenched disorder in the charge-ordered state[19, 36, 37]. There also exists some theoretical studies on the striped phase in the presence of disorder and lattice potentials[38]. However, further measurements on various compounds with different hole-doping levels would be needed to clarify the origin of this quenched disorder.

We interpret this result as the evidence of the existence of the low temperature electronic liquid-crystal phases (ELC), previously predicated by a theory[39, 40]. In an early elastic neutron scattering study, a glassy feature of the stripe phase in $La_{1.6-x}Nd_{0.4}Sr_xCuO_4$ (x = 0.12) was revealed, in which the FWHM of the elastic magnetic peak remained at a finite value below 30 K, corresponding to a spin-spin correlation length of 200 Å. Kivelson and Emery[39] proposed this as a *Nematic Stripe Phase*, or a disrupted *Smectic Stripe phase* because of the presence of quenched disorder. A similar intermediate *Glass State* laying in between the long-range ordered stripe crystal state and disordered stripe liquid state, or *Stripe Glass* was also proposed for the charge stripes in $La_{5/3}Sr_{1/3}NiO_4$[19].

Fig. 7.10 displays the ratio of the widths of the (4.66, 0, 5) along the *k* and *h* directions over the whole measured temperature range. Three different temperature regimes can be clearly identified, as phase I (above 240 K), II (between 220 and 240 K) and III (below 240 K). The ratio, κ_K/κ_H, is almost constant in the Phase III, indicating a static and well-ordered phase in this region, however, it can be well fitted by a linear function in the phase II, indicating the existence of an unique phase between 220 and 240 K. A similar linear behaviour was also found in the same temperature regime of the (5.33, 0, 7). In the phase I, the ratio varies largely because of the appearance of very large charge fluctuations in this critical scattering region.

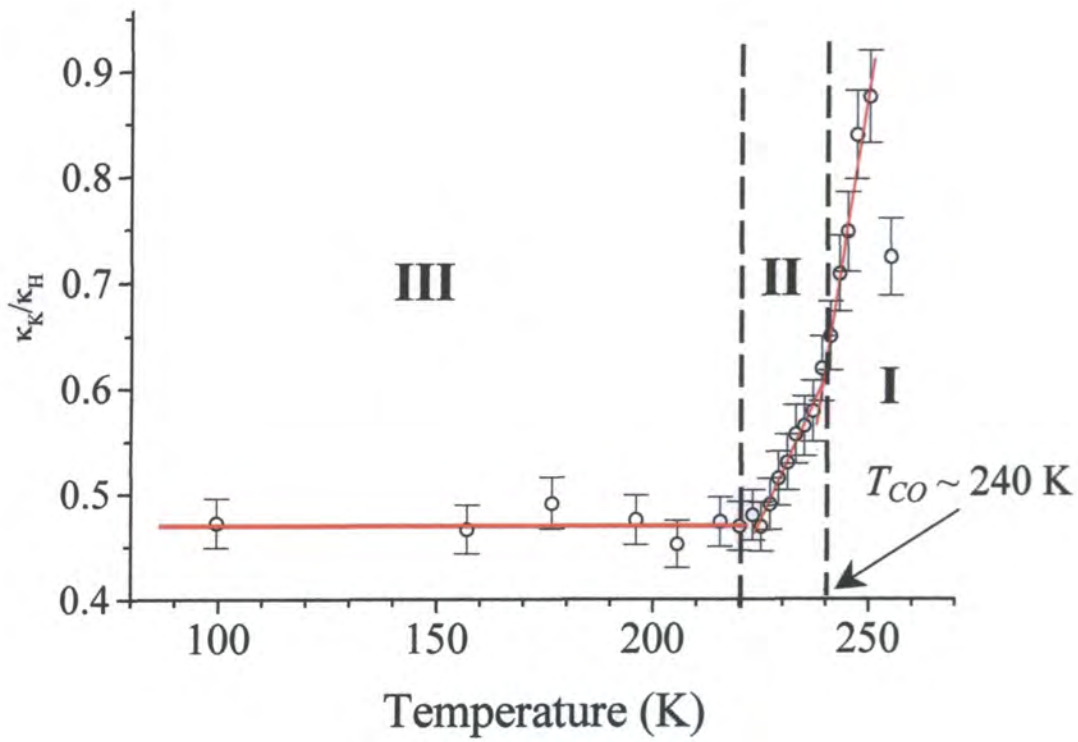

Fig. 7.10 The ratio of the widths along *k* and *h* directions of the (4.66, 0, 5) as a function of temperature, three temperature regimes are indicated.

By analogy with the classical liquid crystal[41], the corresponding ELC phases can be classified as follows,

- *Isotropic stripe liquid (above 240 K):* In this temperature regime, only very weak and broad scattering was observed at the expected positions in reciprocal space, as shown in Fig. 7.8 and Fig. 7.9. Such scattering is caused by critical scattering due to dynamic fluctuations into the charge stripe phase. The size of these charge-ordered clusters increases upon cooling, and the correlation length of these scattering shows a marked divergence close to T_{CO} before the long-range ordered charge stripe phase forms. Fig. 7.11 (1) and (2) show a schematic view of the evolution of the stripe liquid.
- *Electronic nematic phase (220 ~ 240 K):* In this region, the charge stripes are acting just like nematic liquid crystal molecules. The nematic-like charge stripes break the four-fold rotation symmetry, but leave both translation and reflection symmetries unbroken. As shown in Fig. 7.11 (3), the nematic-like charge stripes have a well-defined axis of orientation, indicated by the orientation vector N, however, the transverse fluctuations remain sufficiently large, which can be quantitatively indicated by the measurements of the inverse correlation length along the $\boldsymbol{R}$ direction. An decrease of the inverse correlation length along the transverse direction $\boldsymbol{R}$ upon cooling down can be noticed from Fig. 7.9, but no measured changes along the $\boldsymbol{Q}$ direction can be seen.
- *Electronic smectic phase (below 220 K):* In this temperature regime, following further decrease of the transverse fluctuations, the inverse correlation lengths along both $\boldsymbol{Q}$ and $\boldsymbol{R}$ directions eventually tend to saturate above the experimental resolution below 220 K, as shown in Fig. 7.9 and Fig. 7. 10. The charge stripes in this region can be termed as "smectic stripe". The smectic stripes still remain quasi-long-range order even at very low temperatures, as shown in Fig. 7.11 (4). This behaviour is different from that of crystal-like stripes.

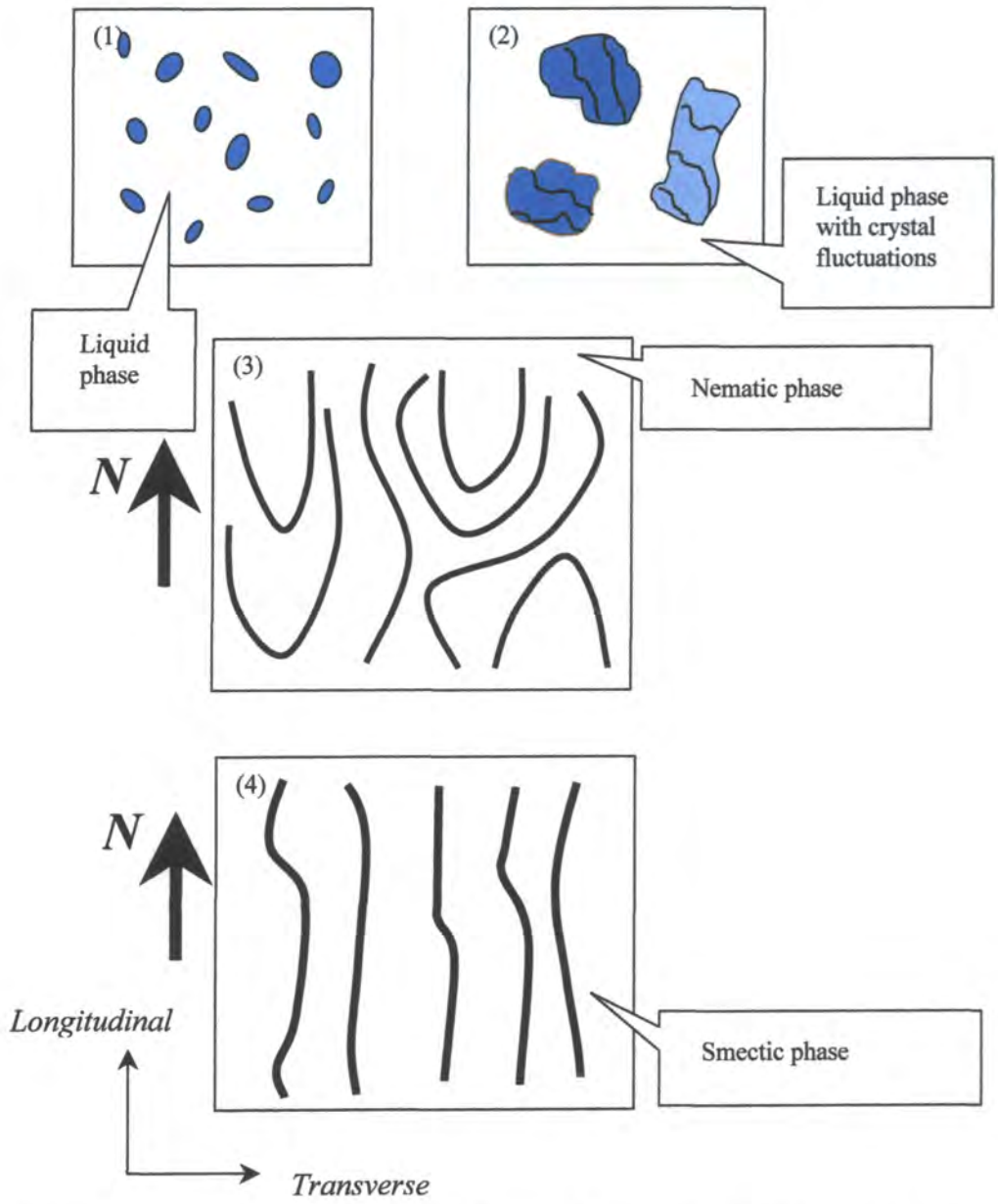

Fig. 7.11 A schematic view of the evolution of electronic liquid-crystal phases. (1) Stripe liquid; (2) Stripe liquid with charge ordering fluctuations; (3) Nematic stripe phase; (4) Smectic stripe phase.

To summarise, the quasi-2D feature of the charge stripes in $La_{5/3}Sr_{1/3}NiO_4$ has been demonstrated by synchrotron radiation x-ray scattering, and the experimental evidence for the existence of the electronic liquid-crystal phases has also been obtained. However, further measurements with higher resolution using synchrotron radiation will be needed to clarify these results in future studies.

7.4 References

1 B. J. Sternlieb, J. P. Hill, U. C. Wildgruber, *et al.*, Physical Review Letters **76**, 2169 (1996).

2 W. Bao, C. H. Chen, S. A. Carter, *et al.*, Solid State Communications **98**, 55 (1996).

3 Y. Moritomo, T. H. Arima, and Y. Tokura, Journal of the Physical Society of Japan **64**, 4117 (1995).

4 M. Kubota, H. Yoshizawa, Y. Moritomo, *et al.*, cond-mat/9811192 (1998).

5 S. W. Cheong, G. Aeppli, T. E. Mason, *et al.*, Physical Review Letters **67**, 1791 (1991).

6 T. E. Mason, cond-mat/9812287 (1998).

7 S. M. Hayden, G. H. Lander, J. Zarestky, *et al.*, Physical Review Letters **68**, 1061 (1992).

8 J. M. Tranquada, D. J. Buttrey, V. Sachan, *et al.*, Physical Review Letters **73**, 1003 (1994).

9 J. M. Tranquada, D. J. Buttrey, J. E. Lorenzo, *et al.*, Physica B **213**, 69 (1995).

10 J. M. Tranquada, J. E. Lorenzo, D. J. Buttrey, *et al.*, Physical Review B-Condensed Matter **52**, 3581 (1995).

11 J. M. Tranquada, D. J. Buttrey, and V. Sachan, Physical Review B-Condensed Matter **54**, 12318 (1996).

12 J. M. Tranquada, Journal of Physics and Chemistry of Solids **59**, 2150 (1998).

13 V. Sachan, D. J. Buttrey, J. M. Tranquada, *et al.*, Physical Review B-Condensed Matter **51**, 12742 (1995).

14 J. E. Lorenzo, J. M. Tranquada, D. J. Buttrey, *et al.*, Physical Review B-Condensed Matter **51**, 3176 (1995).

15 P. Wochner, J. M. Tranquada, D. J. Buttrey, *et al.*, Physica B **241**, 877 (1997).

16 P. Wochner, J. M. Tranquada, D. J. Buttrey, *et al.*, Physical Review B-Condensed Matter **57**, 1066 (1998).

17 C. H. Chen, S. W. Cheong, and A. S. Cooper, Physical Review Letters **71**, 2461 (1993).

18 A. Vigliante, M. vonZimmermann, J. R. Schneider, *et al.*, Physical Review B-Condensed Matter **56**, 8248 (1997).

19 S. H. Lee and S. W. Cheong, Physical Review Letters **79**, 2514 (1997).

20 T. Katsufuji, T. Tanabe, T. Ishikawa, *et al.*, Physical Review B-Condensed Matter **54**, 14230 (1996).

21 S. W. Cheong, H. Y. Hwang, C. H. Chen, *et al.*, Physical Review B-Condensed Matter **49**, 7088 (1994).

22 A. P. Ramirez, P. L. Gammel, S. W. Cheong, *et al.*, Physical Review Letters **76**, 447 (1996).

23 G. Blumberg, M. V. Klein, and S. W. Cheong, Physical Review Letters **80**, 564 (1998).

24 G. Blumberg, M. V. Klein, and S. W. Cheong, Journal of Physics and Chemistry of Solids **59**, 2196 (1998).

25 K. Yamamoto, T. Katsufuji, T. Tanabe, *et al.*, Physical Review Letters **80**, 1493 (1998).

26 Y. Yoshinari, P. C. Hammel, and S.-W. Cheong, cond-mat/9804219 (1998).

27 P. J. Heaney, A. Mehta, G. Sarosi, *et al.*, Physical Review B-Condensed Matter **57**, 10370 (1998).

28 R. A. Cowley, in *Neutron Scattering*, edited by K. Sköld and D. L. Price (Academic Press, Orlando, 1987).

29 D. E. Cox, in *Synchrotron Radiation Crystallography*, edited by P. Coppens (Academic Press, London, 1992).

30 M. F. Collins, *Magnetic Critical Scattering* (Oxford University Press, Oxford, New York, 1989).

31 U. Low, V. J. Emery, K. Fabricius, *et al.*, Physical Review Letters **72**, 1918 (1994).

32 S. R. White and D. J. Scalapino, Physical Review Letters **80**, 1272 (1998).

33 S. R. White and D. J. Scalapino, Physical Review Letters **81**, 3227 (1998).

34 S. R. White and D. J. Scalapino, cond-mat/9812187 v2 (1998).

35 S.-W. Cheong, T. Katsufuji, and C. H. Chen, (private communication, 1998).

36 C. H. Du, Y. Su, J. P. Allen, *et al.*, Physical Review Letters (submitted) (1999).

37 V. J. Emery and S. A. Kivelson, Physica C **209**, 597 (1993).

38 N. Hasselmann, A. H. Castro Netro, C. M. Smith, *et al.*, Physical Review Letters **82**, 2135 (1999).

39 S. A. Kivelson, E. Fradkin, and V. J. Emery, Nature **393**, 550 (1998).

40 S. A. Kivelson and V. J. Emery, cond-mat/9809082 (1998).

41 P. M. Chaikin and T. C. Lubensky, *Principles of Condensed Matter Physics* (Cambridge University Press, Cambridge, 1995).

Chapter 8

Summary

This thesis describes the first comprehensive effort to study charge stripes which exist in some transition-metal oxides by single crystal x-ray scattering. In the previous parts of this thesis, the existence of the charge stripes below the charge ordering transition temperature, T_{CO} in single crystals of $Bi_{0.24}Ca_{0.76}MnO_3$, $Nd_{0.5}Sr_{0.5}MnO_3$ and $La_{5/3}Sr_{1/3}NiO_4$ was confirmed, which can be demonstrated by measuring the additional charge ordering satellite peaks surrounding Bragg peaks. The major results obtained are summarised in this chapter, and the remaining questions and the future work will also be addressed.

$Bi_{0.24}Ca_{0.76}MnO_3$ is the first example which was chosen to demonstrate the existence of the charge stripes in manganese oxides. Weak satellite peaks with a modulation wavevector $\boldsymbol{q_{CO}} \approx (0.24, 0.24, 0)$ were observed below T_{CO}. The first-order nature of the charge ordering transition was demonstrated by observation of hysteresis of in the integrated intensity of the charge stripe satellite peaks as a function of temperature. The correlation length of the charge stripes was almost identical to that of the related Bragg peaks, indicating that the charge stripes in $Bi_{0.24}Ca_{0.76}MnO_3$ are long-range ordered at all temperatures. The strong relationship between the charge stripe ordering and the structural phase transition, which is one of important features for the charge-ordered manganites, was clearly revealed. Those measurements also indicate

that it is possible to directly detect the very weak scattering from charge stripes using long wavelength x-rays.

Following the demonstration of the charge stripes in $Bi_{0.24}Ca_{0.76}MnO_3$, satellite peaks due to the striped charge ordering in the CMR oxide $Nd_{0.5}Sr_{0.5}MnO_3$ were successfully observed through the use of synchrotron radiation x-ray scattering. The charge stripe scattering was found with the modulation wavevector q_{CO} = (1/2, 0, 0) or (0, 0, 1/2). This is the first reported observation of the charge stripe in this compound through single crystal x-ray scattering, and the results are consistent with the CE-type charge ordering pattern suggested for $Nd_{0.5}Sr_{0.5}MnO_3$. From high resolution data taken by triple-axis diffraction, it was confirmed that the (1/2, 0, 0) and (0, 0, 1/2)-type satellites have different correlation lengths, and thus are generated from two perpendicular charge-ordered domains (CODs). The 90° twinned charge-ordered domains are also very important features in the charge-ordered manganites. This is the first direct evidence for the existence of such CODs obtained by x-ray diffraction. In addition, very weak satellite peaks with modulation wavevector q_1 = (1/2, 0, 1/2) and q_2 = (1/2, 1, 1/2) were observed below T_{CO}, which are possibly related to the formation of spin stripes.

Evidence for the quasi two-dimensional (2D) nature of charge stripes in $La_{5/3}Sr_{1/3}NiO_4$ was comprehensively obtained via x-ray scattering. The results obtained indicate that the correlation lengths of the charge stripes are quite anisotropic between the in-plane and out-of-plane directions, or the charge stripes are quasi long-range ordered in the Ni-O layers, but only have very weak correlation between layers. Such a quasi-2D scenario was further confirmed by critical scattering measurements of the charge stripes, which gave the critical exponents predicated of the 2D universality class. One of the most important discoveries is that the charge stripes do not develop long-range order even at very low temperatures, indicating that the charge stripes are disordered and quenched below T_{CO}. We interpret this result as the evidence of existence for a low temperature electronic liquid-crystal phase (ELC),

which was only predicated by a recent theory. Above T_{CO}, 240 K, only very weak and broad critical scattering due to dynamic fluctuations of the charge stripes was observed, giving the evidence for the existence of an isotropic stripe liquid phase. The electronic nematic and smectic phases appear upon cooling down below 240 K and 220 K, respectively. These two phases are distinguished by the marked increasing of transverse fluctuations between 220 and 240 K.

However, there are still some questions remaining. For example, whether the charge ordering satellites observed with four-fold symmetry in $Bi_{0.24}Ca_{0.76}MnO_3$ are due to the *a*- and *b*-axes twinned structures, or just another example for the CODs as observed in $Nd_{0.5}Sr_{0.5}MnO_3$, is still unclear. A better quality single crystal and measurements under higher resolution will be needed to clarify this observation. Furthermore, the origins of these two additional satellites observed in $Nd_{0.5}Sr_{0.5}MnO_3$ require further experimental investigation. Whether the charge stripes in $Nd_{0.5}Sr_{0.5}MnO_3$ are disordered and quenched at very low temperatures requires further measurements in the full temperature range to confirm. In particular, the proposed orbital ordering of CE-type pattern in $Nd_{0.5}Sr_{0.5}MnO_3$ needs direct evidence from the studies of orbital ordering by synchrotron radiation x-ray resonant scattering. Finally, the possible origins of the (2/3, 2/3, 1)-type charge modulations in $La_{5/3}Sr_{1/3}NiO_4$ need to be further examined. The feature of the disordered and quenched charge stripes in $La_{5/3}Sr_{1/3}NiO_4$ certainly needs further measurements on samples with varied hole concentration, which would also be important to clarify the origins of the quenched disordering.